Copyright Warning & Restrictions

The copyright law of the United States (Title 17, United States Code) governs the making of photocopies or other reproductions of copyrighted material.

Under certain conditions specified in the law, libraries and archives are authorized to furnish a photocopy or other reproduction. One of these specified conditions is that the photocopy or reproduction is not to be "used for any purpose other than private study, scholarship, or research." If a, user makes a request for, or later uses, a photocopy or reproduction for purposes in excess of "fair use" that user may be liable for copyright infringement,

This institution reserves the right to refuse to accept a copying order if, in its judgment, fulfillment of the order would involve violation of copyright law.

Please Note: The author retains the copyright while the New Jersey Institute of Technology reserves the right to distribute this thesis or dissertation

Printing note: If you do not wish to print this page, then select "Pages from: first page # to: last page #" on the print dialog screen

NJIT New Jersey's Science & Technology University

The Van Houten library has removed some of the personal information and all signatures from the approval page and biographical sketches of theses and dissertations in order to protect the identity of NJIT graduates and faculty.

ABSTRACT

END-OF-LIFE ANALYSIS OF NANOTECHNOLOGY PRODUCTS

by
Sun Olapiriyakul

Previous research has shown that thermodynamic properties including melting point and specific heat capacity of nanomaterials may be higher than that of their corresponding bulk materials. The melting point elevation and specific heat capacity enhancement of nanomaterials may result in increased energy consumption and waste gases emission at the end-of-life (EOL) stage where the products containing nanomaterials are recycled by high temperature metal recovery (HTMR) process.

In this dissertation, the effect of physical characteristics of nanomaterials, referred to as physicochemical parameters, on their melting temperature and specific heat capacity was investigated. In addition, physical, chemical, and thermodynamic properties of nanomaterials embedded inside commercially available lithium-ion (Li-ion) battery were examined by various characterization techniques including scanning electron microscopy (SEM), energy dispersive X-ray spectroscopy (EDS), X-ray diffraction (XRD), and differential scanning calorimetry (DSC). Thermodynamic analysis techniques with life cycle assessment (LCA) were used to investigate the environmental impacts of nanomaterials during the EOL material recovery stage due to their unusual thermodynamic properties.

As opposed to the energy analysis result, the exergy analysis showed that the chemical reactions that occur during the reduction and smelting processes are the primary sources of exergy loss. If the smelting temperature is increased to fully melt down nanomaterials with unusually high melting point, under assumptions of constant heat

flux, the smelter may operate for a longer period of time resulting in substantial amount of exergy loss and carbon dioxide emission. It was also shown that the reduction process consumes larger amount of energy to raise the temperature of nanomaterials with specific heat capacity enhancement, as opposed to bulk materials. Design for environment (DFE) guideline was developed to improve process performance and risk management. Potential vulnerabilities to recycling of nanomaterials as well as recommended product design and process modifications are summarized.

Finally, a novel exergy footprint was formulated as a sustainable and environmental impact metric that provides a meaningful understanding of the environmental impact of a product or a process. The consumption and flow of exergy in the US economy is defined in terms of five functional categories: materials, transportation, food, water, and direct energy carriers. To illustrate the exergy footprint calculation, the environmental impact associated with the HTMR process measured in terms of exergy loss and exergy consumption were compared to the exergy consumption at a national level.

END-OF-LIFE ANALYSIS OF NANOTECHNOLOGY PRODUCTS

by
Sun Olapiriyakul

A Dissertation
Submitted to the Faculty of
New Jersey Institute of Technology
in Partial Fulfillment of the Requirements for the Degree of
Doctor of Philosophy in Industrial Engineering

Department of Mechanical and Industrial Engineering

January 2010

Copyright © 2010 by Sun Olapiriyakul

ALL RIGHTS RESERVED

APPROVAL PAGE

END-OF-LIFE ANALYSIS OF NANOTECHNOLOGY PRODUCTS

Sun Olapiriyakul

Dr. Reggie J. Caudill, Dissertation Advisor — Date
Professor of Mechanical and Industrial Engineering, NJIT

Dr. Athanassios Bladikas, Committee Member — Date
Associate Professor of Mechanical and Industrial Engineering, NJIT

Dr. Mengchu Zhou, Committee Member — Date
Professor of Electrical and Computer Engineering, NJIT

Dr. Paul G. Ranky, Committee Member — Date
Professor of Mechanical and Industrial Engineering, NJIT

Dr. Sanchoy K. Das, Committee Member — Date
Professor of Mechanical and Industrial Engineering, NJIT

Dr. Zhiming Ji, Committee Member — Date
Associate Professor of Mechanical and Industrial Engineering, NJIT

BIOGRAPHICAL SKETCH

Author: Sun Olapiriyakul

Degree: Doctor of Philosophy

Date: January 2010

Undergraduate and Graduate Education:

- Doctor of Philosophy in Industrial Engineering,
  New Jersey Institute of Technology, Newark, NJ, 2010.

- Master of Science in Industrial Engineering,
  San Jose State University, San Jose, CA, 2003.

- Bachelor of Science in Mechanical Engineering,
  Sirindhorn International Institute of Technology, Thammasat University, Pathum Thani, Thailand, 1999.

Major: Industrial Engineering

Presentations and Publications:

Olapiriyakul, S., Caudill R.J., Thermodynamic Analysis to Assess the Environmental Impact of End-of-life Recovery Processing for Nanotechnology Products. *Environmental Science and Technology* **2009,** *43*, (21), 8140-8146.

Olapiriyakul, S., Elele, E., Caudill, R.J., End-Of-Life Analysis of Nanotechnology Products: A Case Study Focusing on the High Temperature Battery Recycling Process. In *13th Battery Materials Recycling Seminar and Exibit*, Florida, 2009.

Olapiriyakul, S., Caudill, R.J. In *A Framework for Risk Management and End-Of-Life (EOL) Analysis for Nanotechnology Products: A Case Study in Lithium-Ion Batteries*, Proceedings of the 2008 IEEE International Symposium on Electronics & the Environment, 2008.

Olapiriyakul, S., Das, S.K., Design and analysis of a two-stage security screening and inspection system. *Journal of Air Transport Management* **2007,** *13*, (2), 67-74.

Olapiriyakul, S., Abdel-Malek, L., Hsieh, H.N., Meegoda, J.N., El Haggar, S., Post Optimality Analysis of a Solid Waste Management System; a Case Study. In *1st Global Cleaner Production Conference and Exhibition "Clean Globe 1"*, Nasr City, Cairo, Egypt, 2006.

Olapiriyakul, S., Borgaonkar, A., Abdel-Malek, L., Hsieh, H.N., Meegoda, J.N., The Potential Advantages of Applying Operations Research Techniques to Optimize Waste Management in New Jersey. In *1st Global Cleaner Production Conference and Exhibition "Clean Globe 1"*, Nasr City, Cairo, Egypt, 2006.

Dedicated to my family

ACKNOWLEDGMENT

I would like to express my sincere appreciation to my dissertation advisor, Dr. Reggie J. Caudill, for his guidance, compassionate support, and wisdom. I also would like to thank other committee members: Dr. Anthanassios Bladikas, Dr. Paul Ranky, Dr. Sanchoy Das, and Dr. Zhiming Ji for their valuable time and insightful comments.

The financial support by the Government of Thailand, Commission on Higher Education, Ministry of Education, NJIT Multi-lifecycle Engineering Research Center, and New Jersey Institute of Technology is gratefully acknowledged.

I wish to express my gratitude to Dr. Theodore Davidson for his insightful comments on thermodynamic analysis of the HTMR recycling process, and to Dr. Zafar Iqbal for very helpful discussions regarding the melting behaviors and potential impacts of nanomaterials. Thank to Ezinwa Elele for his help on nanomaterials characterization experiments. I also wish to thank my previous academic advisors: Dr. Jacob Tsao and Dr. Sanchoy Das for their continuous support and guidance throughout my time as a graduate student at San Jose State University and New Jersey Institute of Technology.

Special thank to Dr. Atipol Kanchanapiboon, Mojisola Otegbeye, Randy Raegan and other industrial engineering colleagues for their support and friendship during my years at New Jersey Institute of Technology. Most importantly, I wish to express my deepest thanks and greatest love to my parents, my wife, my sons Pakin and Pete and all other family members for all the sacrifices they have endured for my success.

TABLE OF CONTENTS

TABLE OF CONTENTS
(Continued)

TABLE OF CONTENTS
(Continued)

TABLE OF CONTENTS
(Continued)

LIST OF TABLES

LIST OF TABLES
(Continued)

LIST OF FIGURES

LIST OF FIGURES
(Continued)

NOMENCLATURE

i	material
$C_{p,i}$	heat capacity of material i (KJ/K-Kg)
e_i	standard chemical exergy of material i (KJ/mole)
E_{input}	energy input (KJ)
E_{output}	energy output (KJ)
E_{loss}	energy loss (KJ)
ΔE	change of internal energy (KJ)
Ex_{input}	exergy input (KJ)
Ex_{output}	exergy output (KJ)
Ex_{loss}	exergy loss (KJ)
$Ex_{unusable}$	exergy of unusable materials (KJ)
$Ex_{irr\ loss}$	exergy loss due to process irreversibility (KJ)
$Ex_{ch,i}$	chemical exergy of material i (KJ)
$Ex_{th,i}$	thermal exergy of material i (KJ)
ΔH	change in enthalpy (KJ)
$\dot{m}$	mass flow rate (kg/hr)
T_0	reference (ambient) temperature (298 K)
T_i	temperature of material i (K)
ΔT	change in temperature (K)

CHAPTER 1

INTRODUCTION

1.1 Problem Statement

Nanotechnology is rapidly moving from the research labs into development and commercialization with nanoproducts beginning to appear in almost every market segment. Recent efforts have focused on the use of nanomaterials in electronics due to the potential to significantly improve performance and reduce cost. However, concerns regarding the environmental behaviors and the possible health and environmental risks of manufactured nanomaterials have been raised by the government organizations such as U.S. Environmental Protection Agency [USEPA] and National Science and Technology Council [NNCO].

Energy analysis and life cycle assessment (LCA) studies have been performed to evaluate resource usage, as well as the economic and environmental impacts of nanotechnology. Previous studies indicate that the high energy requirement and high environmental impact of nanomaterials at the production stage is outweighted by the reduction in raw materials at the production stage and savings in energy at the use stage of nanoproducts [Lloyd and Lave, 2003, 2005]. However, the scope of this previous research was limited to the production and use stages without considering the end-of-life (EOL) material recovery stage. The life cycle of nanomaterials is shown in Figure 1.1. The impact of the size-dependent properties of nanomaterials was also excluded from most of the previous studies. Moreover, measuring only the input and output energy, traditional energy analysis frequently leads to an incomplete or misleading conclusion

regarding process performance due the inability to account for chemical potential of materials and the loss of useful energy due to process irreversibility.

In addition to the primary concern in term of toxicity, research shows that chemical and mechanical properties [Edelstein and Cammarata, 1998] as well as thermal properties [Chen, 2005] of nanomaterials can differ significantly from the bulk counterpart. The phase transition temperature (melting point) of nanoparticles has been demonstrated to vary significantly from that of their bulk forms due to their large surface-to-volume ratio, small particle size, unique structure, and host matrices. While a depression in melting point (called "supercooling") usually occurs in free-standing nanoparticles, an elevation of melting point (called "superheating") may occur in cases where nanoparticles or nano-thin film is embedded in the host matrix [Qi and Wang, 2005, Zhang et al., 2006]. Nanoparticles and thin films made of high-melting-point materials, such as iron and titanium, are being used as electrode materials by several Li-ion batteries manufacturers, including Valence Technology [Peter, 2005], A123systems [A123systems], and Altairnano [Altairnano, 2005]. Superheating of these materials could create problems for recyclers ranging from waste handling to feedstock contamination and even nanoparticle emissions. Preliminary findings by Olapiriyakul and Caudill [Olapiriyakul and Caudill, 2008, 2009] indicates that the melting behavior of nanomaterials may result in the increased energy consumption and waste gases emission at the EOL stage of nanomaterials-containing products. In addition to the melting behavior, specific heat capacity of nanomaterials is usually higher than that of the corresponding bulk materials at low temperature range [Chen, 2005]. This phenomenon is commonly called heat capacity enhancement or excess heat capacity of nanomaterials.

The heat capacity enhancement of nanomaterials may result in higher heat energy required by HTMR process to raise the temperature of the recyclates to their melting point. This may also result in longer operating time and increased waste gas emission by HTMR process.

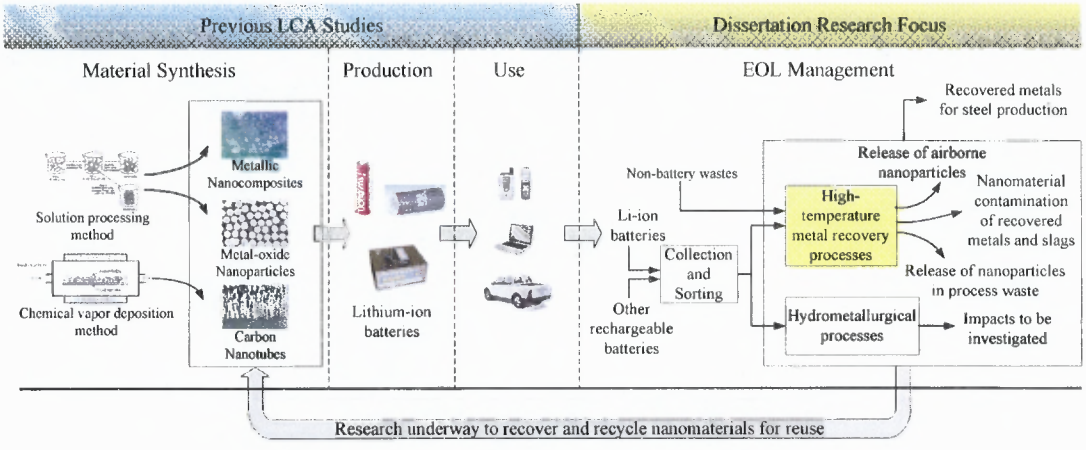

Figure 1.1 Life cycle of nanomaterials for Li-ion batteries.

Source: [Olapiriyakul and Caudill, 2008]

Note: Figure 1.1 is modified from the original figure.

1.2 Research Objective

The primary objective of the dissertation is to investigate the environmental impact of nanomaterials-containing lithium-ion (Li-ion) batteries during the EOL product lifecycle stage. A traditional high temperature metal recovery (HTMR) process typically used for battery recycling is assumed as the recycling method. Secondary research objectives are: (1) to verify the existence of nanomaterial within commercially available Li-ion batteries by using nanomaterial characterization techniques; (2) to investigate the characteristics of nanomaterials being developed for advanced Li-ion batteries and their correlation with the size-dependent properties of nanomaterials; (3) to analyze the environmental impact

of the nanomaterials on the existing HTMR process by using thermodynamic analysis (both energy and exergy concepts) and traditional LCA techniques; (4) to develop design for environment (DFE) guidelines to recommend improvements in product design and recycling processes based on the results of thermodynamic analysis and LCA; and (5) to develop a unique exergy footprint analysis to create a quantitative lifecycle environmental impact metric to complement the use of LCA and exergy analysis.

1.3 Research Significance

The research presented here is the first effort to date that utilizes energy and exergy analyses and LCA techniques to investigate EOL recycling processes and the associated environmental impacts of nanoproducts caused by size-dependent properties of nanomaterials. Consequently, this research represents several significant contributions to the field of environmentally-sound product lifecycle management and the design of products for end-of-life material recovery.

In this dissertation, material characterization experiments are also performed to examine the characteristics and thermodynamic properties of nanomaterials used in commercially available Li-ion batteries made by A123Systems. The dissertation presents the first research in which data obtained from the material characterization experiments are used in assessing the environmental impacts of nanoproducts at the EOL recycling stage.

Additionally, this is also the first time where the design for environment (DFE) guidelines for nanoproducts are constructed based on the results of energy and exergy analyses and the impacts of the properties/behaviors of nanomaterials. The guidelines, consisting of the physical properties of nanomaterials as DFE attributes, will give product designers deeper insights into the environmental impacts of nanoproducts.

Furthermore, to compare the exergy usage of nanoproducts with the amount of exergy available, the concept of exergy is used to develop a unique exergy footprint analysis to create a quantitative lifecycle environmental impact metric to complement the use of LCA and exergy analysis. Based on the exergy footprint concept, the product lifecycle exergy consumption can be analyzed and compared with the exergy associated with national resource consumption, creating a novel exergy footprint normalized at the national level.

1.4 Research Methodology

A case study based on lithium-ion (Li-ion) batteries with a conventional high-temperature material recovery (HTMR) process is presented here to demonstrate the use of exergy analysis, in addition to energy analysis and LCA, to assess environmental impacts of nanoproducts during the EOL stage. Li-ion batteries, utilized broadly in many electronic products, offer a rich application area for nanomaterials within a relatively simple product structure. The concerns of EOL management and recycling of nano-enabled Li-ion batteries are both timely and important as these batteries are already in the marketplace and moving into the recycle stream.

The characteristics of nanomaterials used in A123Systems Li-ion batteries are examined by performing various characterization techniques. The size and structure of nanostructured coating material of the positive electrode of the battery is examined by using scanning electron microscopy (SEM). The chemical composition is determined by the combined use of energy-dispersive X-ray spectroscopy (EDS) and X-ray diffraction (XRD). Then, the specific heat capacity of the coating material and the electrode is measured by differential scanning calorimetry (DSC).

At the first step of the HTMR battery recycling process, shredders equipped with traditional filtration systems may release nanoparticles into the atmosphere due to the motion and velocity of nanoparticles in air media. In this dissertation, discrete event simulation methods are used to investigate the penetration of nanoparticles through commercial filter media. Then, the environmental impacts caused by the superheating and specific heat capacity enhancement phenomenon during the subsequent high-temperature processes are examined by using exergy analysis, in addition to energy analysis and LCA.

Energy analysis, focusing only on the heat content of material flows, identifies the smelting process as the primary source for process loss. However, in the case of HTMR recycling process, the results of exergy analysis provide more insight into the environmental impact as the process is partly driven by chemical reactions. As opposed to the energy analysis result, the exergy analysis and LCA assessment show that the chemical reactions that occur during the reduction and smelting processes are the primary source of exergy loss and carbon dioxide emissions, and not energy consumption. When the smelting temperature is increased as needed to melt the nanomaterials, the smelter

must operate for a longer period of time resulting in larger amount of exergy loss and carbon dioxide emissions caused by the prolonged chemical reaction and higher energy requirement. These exergy losses within the system boundary will eventually dissipate into the ecosystem and create environmental impacts. To avoid these impacts, DFE guideline is developed to provide the designer of nanoproducts with an insight into the environmental impacts at the EOL stage associated with the product design attributes which are the characteristics of nanomaterials such as size, structure, and film thickness.

1.5 Organization of the Paper

In Chapter 2, background information on nanomaterials and their properties as well as the case study of Li-ion battery and HTMR process is presented. Review of the literature surrounding LCA of nanomaterials and nanoproducts is also given. Chapter 3 provides the experimental results of material characterization performed to examine the surface topography, chemical composition, and specific heat capacity of the positive electrode of an A123Systems Li-ion battery. In chapter 4, the impacts of Brownian motion on nanoparticles filtration is presented as well as the results of the discrete event simulation study showing the size distribution of penetrated nanoparticles. Chapter 5 presents the environment and process impacts from thermodynamic properties of nanomaterials. The details on energy and exergy analyses and LCA can be found in this chapter. Chapter 6 presents preliminary DFE guidelines for nanoproducts. The environmental impacts at the EOL stage associated with nanoproduct's design alternatives are examined in this chapter. Chapter 7 illustrates the development of exergy footprint analysis and its use as a

quantitative lifecycle environmental impact metric. The exergy associated with the resource consumption in the United States is calculated in this chapter.

CHAPTER 2

LITERATURE REVIEW

2.1 Nanomaterials in Electronic Applications

Nanomaterials can be described as materials having at least one dimension of between one and one-hundred nanometers. The dimension could be a particle diameter, layer thickness, or fiber length. Conventional materials have grains varying in size anywhere from 100's of microns (μm) to millimeters (mm). Each grain is composed of many atoms. The average size of an atom is on the order of 1 to 2 angstroms (Å) in radius (1 nanometer is equal to 10 Å).

Nanomaterials often display enhanced properties compared to bulk, which offer breakthrough advances in many applications. Advances in microelectronics technologies are leading to circuitry containing smaller transistors, resisters, and capacitors which operate at higher clock speeds. Faster processing and clock speeds tend to yield higher probability of system break down due to poor heat dissipation (overheating) of the bulk material while running at these higher speeds. Nanomaterials such as carbon nanotubes (CNTs) can solve these problems due to its inherently high thermal conductivities and high mechanical strength [Ngo et al., 2004]. The excellent electron emitting properties of CNTs also enable their applications in electron emitting devices such as flat panel display [Wilson, 2006]. CNTs-based electron gun provides flat panel display with a longer lifetime, superior picture quality, and lower operating and manufacturing costs. Magnetic data storage is another important electronics application. Despite the smaller size of data storage devices, the density of information stored on hard disks has increased

dramatically by using nanosized high-performance magnetic thin films for high-density magnetic recording [Osaka et al., 2005].

In the past decade, nanomaterials and nanofabrication techniques have been used to improve energy applications such as fuel cells in terms of electrochemical performances and manufacturing cost. Proton Exchange Membrane (PEM) fuel cells become more commercially viable by using nanostructured catalyst particles. The extremely large surface area of nanomaterials can accelerate chemical reactions and, hence, allow the high-cost catalysts such as platinum to be used more efficiently. Solar cell, capacitor, and rechargeable batteries especially Li-ion are also energy applications which have been improving recently by the use of nanomaterials.

2.2 Li-ion Battery Case Study

The application of nanomaterials in electronic products with a focus on Li-ion batteries has been carefully selected as the case study. The miniaturization of electronics applications has created demand for smaller and lighter energy sources. Li-ion batteries, utilized broadly in many electronic products, offer a rich application area for nanomaterials within a relatively simple product structure. The concerns of EOL management and recycling of nano-enabled Li-ion batteries are both timely and important as these batteries are already in the marketplace and moving into the waste stream.

2.2.1 Main Components of Li-ion Battery

The main components of a Li-ion battery cell are the negative electrode (anode), the positive electrode (cathode), and the electrolyte. Other components include the separator and metal/plastic case. Conventional anodes and cathodes typically use graphite and lithium cobalt oxide as the primary bulk material constituents, respectively. Electrolyte is composed of lithium salts. The chemical composition of a typical Li-ion cell is shown in Table 2.1.

Table 2.1 Chemical Composition of Li-ion Battery

Component	wt.%
$LiCoO_2$	27.5
Steel/Ni	24.5
Cu/Al	14.5
Carbon	16
Electrolyte	3.5
Polymer	14

Source: [Lee and Rhee 2002]

2.2.2 Mechanism of Li-ion Battery

The mechanism by which a Li-ion battery converts chemical energy directly into electrical energy involves the charge and discharge processes. Upon charging, lithium ions are extracted from the cathode and inserted into the anode via the electrolyte which behaves as the conducting medium for the ions. Upon discharging, the lithium ions return to the cathode, releasing energy in the process. Therefore, battery performance characteristics—capacity, energy density, and cycling performance—are related to the intrinsic properties of the materials that form the cathode, anode, and electrolyte.

2.2.3 Chemical Composition of Conventional Li-ion cells

Cathode Materials

Conventional Li-ion cells use microcrystalline transition metal oxides as cathode material which acts as a host compound where lithium ions can be inserted and extracted reversibly during cycling process. A Li-ion battery made of lithium cobalt oxide ($LiCoO_2$) cathode was first commercialized by Sony in 1991. Currently, $LiCoO_2$ is the most widely used transition metal oxide due to the high energy density. However, the cobalt-based cathode is expensive and highly toxic to humans and the ecosystem.

Human toxicity of cobalt includes heart muscle diseases, genotoxic, and various lung diseases [Kim et al., 2006[b]]. Cobalt is also classified by International Agency for Research on Cancer (IARC) as a possible human carcinogen (group 2B) [Altamirano-Lozano et al., 2006]. Moreover, cobalt has both high acute (short-term) toxicity and chronic (long-term) toxicity on plant [Palit et al., 1994] and aquatic life [B.C. Government].

The search for a better cathode material focused on materials that are inexpensive and non-toxic. Multi-metal oxides such as nickel-cobalt-manganese compound were among very first alternatives to lithium cobalt oxide [Amine et al., 2005]. Other non-cobalt cathode materials found on the market today are manganese spinel and iron phosphate.

Anode Materials

Li-ion technologies employ various forms of carbonaceous materials as lithium insertion anodes. Conventional carbon-based anode is made of synthetic graphite and acetylene type carbon black. The high conductivity of graphite and its good chemical stability are attractive features for its use as anode material. Graphite has higher electrical conductivity than acetylene black. On the other hand, acetylene black is capable of retaining over three times as much electrolyte as graphite.

Carbon black is a form of amorphous (no well-defined structure) carbon produced by thermal decomposition of hydrocarbons or incomplete combustion of natural gas and petroleum oil. Amorphous carbons generally have high surface area, high porosity, and small particle size. Acetylene type carbon black (acetylene black), which is produced by the thermal decomposition of acetylene gas, is commonly used as an electrically conductive additive in the anode of Li-ion battery.

2.2.4 Li-ion Battery Performances

For rechargeable batteries, the primary performance measures are the energy density, power density, and cyclability. Examples of other secondary measures are charging time, safety, shelf life, cycling performance, and ability to charge and discharge at an extremely low temperature. In most cases, the battery's performance depends on the intrinsic properties of electrode materials.

Energy Density

The battery energy density is the amount of energy stored per unit mass (Wh/kg) or volume (Wh/L). A battery with higher energy density can hold more energy resulting in a longer runtime which is the primary performances for portable electronics devices such as cell phones, notebook computers, and digital cameras.

Power Density

The battery power density is the amount of electric energy delivered per unit time (W/kg). The power density can also be expressed as the ability of the battery to discharge quickly. High power density batteries are required by high-power applications such as power tools and electric vehicles.

Cyclability

Frequently referred to as rechargeability or battery life, cyclability can be expressed as the number of cycles the battery can deliver an energy level higher than 80% of its nominal energy.

2.2.5 Examples of Nanomaterial Applications in Li-ion Batteries

During the past few years, improvements in Li-ion battery performance are being realized through application of various nanomaterial technologies. The main elements of Li-ion cells are constructed of nanomaterials made of the same or different composition. These new nanobatteries are being developed and commercialized by several battery manufacturers and academic researchers, as shown in Table 2.2. Nanotechnology allows the use of materials which have high lithium storage capacity, such as tin and silicon,

without the large volume expansion problem associated with conventional materials. The use of nanostructured titanate as anode materials produces faster charging times because lithium ions can be inserted into nanostructured titanate at a higher rate compared to graphite. Nanostructured silicon material is being considered as a separator to store electrolyte away from the electrodes, resulting in an extremely long inactive shelf life. As these examples indicate, nanomaterials have broad application to enhance Li-ion battery performance as a result of both their chemical and physical properties. [1]

Table 2.2 Nano-based Li-Ion Battery Technologies

Organizations	Nanomaterial-embedded Components	Performances
Sony[1]	Tin-based amorphous anode	High energy density
Stanford U.[2]	Silicon nanowire anode	High energy density
A123 Systems[3]	Nanostructured iron phosphate cathode	High power and safer
Valence Tech.[4]	Nanostructured iron phosphate cathode	High power and safer
Altairnano[5]	Nanostructured lithium titanate anode	Fast charging time
mPhase[6]	Electrolyte separator made of nanostructured silicon surfaces	Extremely long shelf life

Source: [1] [Sony], [2] [Chan et al., 2008], [3] [A123systems], [4] [Peter, 2005], [5] [Altairnano, 2005], [6] [Lifton and simon, 2005]

Cathode Material

Lithium iron phosphate ($LiFePO_4$) has been widely investigated as a cathode material for high power density Li-ion batteries [Jugovic and Uskokovic, 2009]. The material is inexpensive, non-toxic, and intrinsically safe due to its high thermal stability. However, the main disadvantages of lithium iron phosphate are its low electronic conductivity and low lithium ion diffusion rate resulting in the loss of reversible capacity at high current density.

The commercialization of Li-ion batteries containing $LiFePO_4$ cathode materials has been realized by morphological modification of the material at nano-scale to increase its electronic conductivity [Hsu et al., 2004]. One of the claimed performances is the very high power density. The solid-state synthesis is used for the scaled-up production of $LiFePO_4$ nanoparticles by A123Systems [Chiang et al., 2007], Valence Technology Inc [Saidi et al., 2006], and Sony [Yamada et al., 2003]. The process involves the decomposition and heating of the mixture of lithium, iron, and phosphate compounds at high temperatures. Alternatively, chemical route technique such as Sol gel method can be used to produce high-purity $LiFePO_4$ nanoparticles [Hsu et al., 2004].

Anode Material

The development of anode materials has been achieved by structural modification of carbonaceous materials. CNTs, discovered by Sumio Iijima of NEC in 1991 [Ijima, 1991], have been widely studied as anode materials for Li-ion batteries. CNTs can be structurally classified into single-walled nanotubes (SWNTs) and multi-wall nanotubes (MWNTs). SWNTs have one layer of graphene sheet while MWNTs have many layers.

The potential use of CNTs as anode materials of high-capacity Li-ion batteries has been investigated due to their higher surface area and hence higher lithium storage capacity compared with graphite [Gao et al., 1999, Wu et al., 1999] CNTs-based composite materials have been shown to be a good candidate for anode material due to their high energy density and high capacity retention over charge-discharge cycles [Wang and Kumta, 2007]. CNTs can be metallic or semiconducting depending on the

arrangement of carbon atoms. Semiconducting SWNTs with extended length can be used as electronic circuit components such as switch and transistor.

Another carbonaceous anode material called PUREBLACK, is a partially graphitized nano-sized carbon black [Barsukov et al., 2006]. The material has higher electrical conductivity than acetylene type carbon black and has very low impurities. PUREBLACK-205, developed and commercialized by Superior Graphite (Chicaco, IL, USA) and Columbian Chemicals Co. (Marietta, GA, USA), has average particle size of 40 nm [Portet et al., 2007].

For high-energy-density Li-ion batteries, tin and silicon are promising anode materials due to their high lithium storage capacity which is the amount of lithium ions the material can store. However, tin and silicon exhibit large volume expansion and shrinkage during charge-discharge cycles resulting in disintegration of the electrode and, hence, the loss of electronic contact of active material, giving severe capacity fade.

Nanostructured tin and silicon have been used to circumvent the volume expansion problem due to the fact that smaller particles yield lower degree of volume expansion compared to larger particles. Various nanostructured silicon-based anode materials under studied include silicon-carbon nanocomposite and silicon thin film deposited on a nickel foil [Kasavajjula et al., 2007]. Scientists also employed various nanostructured tin-based materials, particularly tin oxides, to circumvent this volume-change problem [Li et al., 2000, Chandra Bose et al., 2002].

Nanostructured titanate can also be a substitute material for carbon in the negative electrode. Existing carbon-based anodes suffer from safety concerns (electroplating of lithium) and the formation of a solid-electrolyte interface (SEI) layer consuming the

charge. Anode materials containing nanostructured titanate, nanostructured lithium titanate spinel oxide, are being developed and commercialized by Altairnano [Altairnano, 2005]. Among the claimed enhancements are the super-fast recharging and discharging time (one minute recharge) and the capability to operate in extreme temperatures. These improvements result from the absence of SEI layer and large surface area of the active material.

2.3 Nanomaterials Processing Methods

A review of the synthesis methods used for industrial-scale production of these nanomaterials is given in this section of dissertation. The energy and input materials consumption of each synthesis method are discussed as this information is required in assessing the environmental impacts of nanoproducts during the material synthesis stage. The information regarding the ability of each synthesis method in controlling the physical properties including size, length, thickness, structure, and the level of impurities are demonstrated. These properties not only affect the battery performance but also their degree of toxicity and their fate during the recycling process and after releasing into the environment.

Nanomaterials synthesis methods involve the manipulation of materials at the atomic level. In general, the synthesis methods fall into two classes, which are called top-down and bottom-up. Top-down techniques involve the process of miniaturizing macro-scale structures into much smaller structures. The top-down technique such as lithography is widely used to produce micro-electro-mechanical systems (MEMS) and microelectronics.

However, most of the existing lithography techniques are impractical for large-scale manufacturing of nanomaterials due to the limitation of the minimum feature size that can be produced. Moreover, special handling and disposal of toxic chemicals used for etching out the patterns are required, which drive up the cost of the process [Pechenik, 2002].

Bottom-up or self-assembly process is a process that causes molecules to aggregate by non-covalent interactions into stable well-defined structures, without human intervention. The creation of nanomaterials used in electronic applications and Li-ion batteries are mostly built upon bottom-up methods due to their capability for large-scale production [Uskokovic, 2007]. Four examples of widely used bottom-up methods, chemical vapor deposition (CVD), high pressure carbon monoxide disproportionation (HiPCO), and sol-gel, and combustion synthesis are discussed in this section.

2.3.1 Chemical Vapor Deposition

CVD can be used to produce nanomaterials with various kinds of structure, such as free-standing nanoparticles, nanocomposite, and film (or coating). Size (or coating thickness), surface morphology, and types of the interface between the substrate and the growth material can be controlled by adjusting the process parameters such as temperature, pressure, gas flow rate. However, large amount of energy is required to maintain the high operating temperature. Moreover, additional chemical purification may need to be performed for catalysts and residuals removal.

The synthesis involves the deposition of the gaseous atoms of precursor on the substrate, dispersed with small metal catalysts such as iron particles. The substrate is set into the hotspot of the furnace under a constant flow of hydrocarbon such as benzene and hydrogen and argon mixture gas, resulting in the growth of CNTs as shown in Figure 2.1.

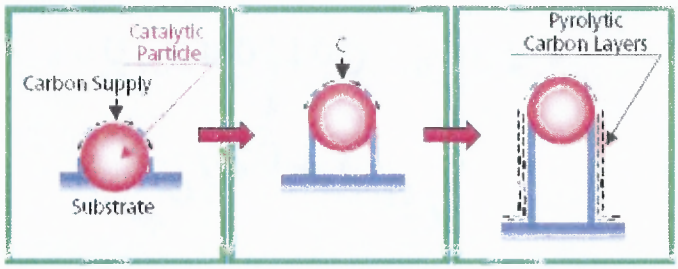

Carbon diffuses around the catalyst to form the tubular structure.

Figure 2.1 Schematic image of tip-growth model.
Source [Endo, 1988]

This conventional method, called seeding method, is a non-continuous method which is impractical for large-scale production. Due to the strong demand for CNTs, a continuous method, called the floating reactant method, was developed by Endo and his research group [Endo et al., 2006]. This method gradually supplies the catalyst and hydrocarbon along with the carrier gas resulting in the carbon deposition process and the growth of CNTs at the floating catalyst particles as depicted in Figure 2.2. This method is now being used for an industrial-scale production by Nikkiso Co., LTD in Japan [Nikkiso R&D Report].

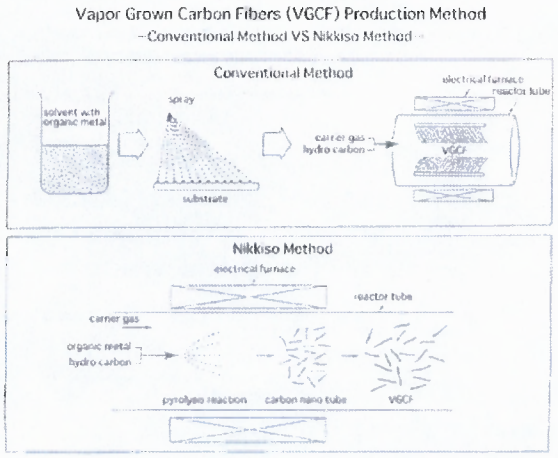

Figure 2.2 Schematic of floating reactant.
Source: [Nikkiso R&D Report]

Two excellent candidate anode materials that can be produced by CVD are CNTs [Wu et al., 2003] and silicon-based nanomaterials [Graetz et al., 2003]. Hydrocarbon and silane (silicon hydrides) are generally used as the precursor for their production, respectively. CNTs and silicon have higher lithium-storage capacity compared with graphite. Nanostructure of silicon also inhibits the large volume expansion of microstructure silicon, preventing the capacity fade over charging-discharging cycles.

2.3.2 High Pressure Carbon Monoxide Disproportionation

High Pressure Carbon Monoxide Disproportionation (HiPCO) process, invented by the Smalley research group in the 1990s, can produce high-purity SWNTs in large quantities. The process uses carbon monoxide (CO) as the carbon feedstock and iron pentacarbonyl ($Fe(CO)_5$) as the catalyst precursor. The use of CO instead of hydrocarbons which are the commonly-used carbon feedstock for CVD method substantially reduces the formation of amorphous carbon and hence eliminates the need for additional purification processes.

In the process, CO and the nano-sized iron-containing catalyst are continuously supplied into the reactor with the reaction temperature of between 800 and 1200 °C and the reaction pressure of between 1 and 10 atm [Nikolaev et al., 1999]. The higher production rates can be achieved by maintaining the reaction temperature and pressure at higher levels. The tube's diameter can be controlled by varying the pressure of CO. The average diameter of the tube produced by HiPCO process is only 1.1 nm approximately [Chiang et al., 2001]. The length of the tube can be controlled by varying the reaction time.

2.3.3 Sol Gel

Sol-gel method is capable of producing various kinds of oxide nanomaterials such as nanoparticles, nanocomposite, nanofibers, and thin film. The distinctive advantages of sol-gel method include the simple processing steps, low operating cost, low equipment cost, accurate control of the chemical composition and high purity of the final products.

The process starts with the formation of homogeneous solution (sol) which is the mixture of the desired oxide precursors and water (or alcohol). Further solidification processes of sol determine the forms of the final product as shown in Figure 2.3. In processing anatase titanium dioxide nanoparticles, an electrode material for nano-enabled Li-ion batteries, the sol is concentrated at low temperature and transformed into gel. The gel undergoes calcination (heating at high temperature but below the melting point) to yield the nanoparticles [Liu et al., 2005]. When alternate nanostructures are preferred, adjustment can be made to the processing parameters which include the types of precursor, water content, methods of transforming the sol into gel, and heating temperature.

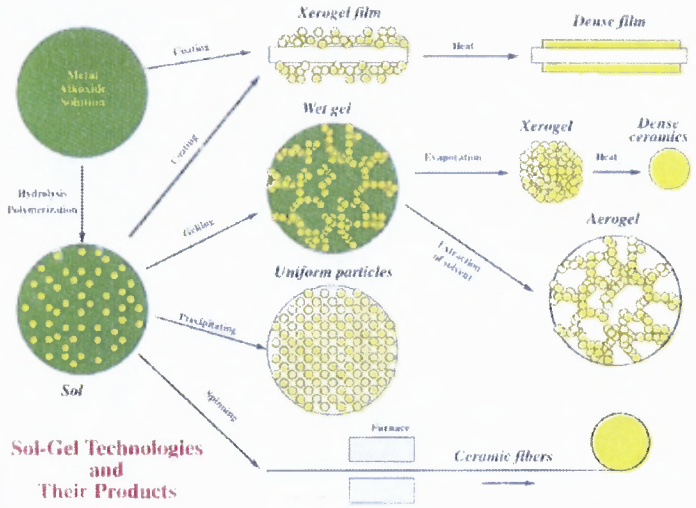

Figure 2.3 Sol-Gel Technologies and their products.
Source: [Chemat Group]

2.3.4 Combustion Synthesis

Combustion synthesis is a cost-effective chemical route technique capable of producing various types of oxides in the form of nanoparticles that are smaller and more uniform in size and shape than those produced by sol-gel methods. Sol-gel nanoparticles often require post-treatment at high temperature resulting in agglomeration of particles and thereby negating any benefits of nanoparticles from their large surface area.

Combustion synthesis is a two-step process: 1. formation of precursor and; and, 2. gas evolution. At the first step, the formation of viscous and homogenous liquid or gel occurs by heating the mixture of fuel and the starting constituents, which is the corresponding metal nitrates, at low temperature. Examples of the fuel are glycine, critic acids, urea, ascorbic acid, acetone, and the combination of them. At the second step, the temperature of the liquid is raised to the combustion temperature resulting in the ignition, rapid evolution of gaseous products, and thereby the formation of nanoparticles.

The characteristics such as size, shape, and structure of nanoparticles produced by combustion synthesis can be controlled by altering the type of fuel and the ratio between the starting constituents and the fuel, often referred to as oxidant-to-fuel ratio. Nanoparticles metal phosphate, cathode materials for Li-ion batteries, with particle size ranging from 12 nm to 33 nm was produced Eltron research, Inc. by using combustion synthesis method [Eltron Research Inc., 2004]. A123systems also produce their patented nanostructured iron phosphate by using combustion synthesis with milling and heat treatment techniques. The starting constituents include lithium carbonate (Li_2CO_3), iron (II) oxalate ($Fe(C_2O_4)$), and ammonium phosphate ($(NH_4)_3PO_4$). High purity acetone is used as the fuel [Chiang et al., 2007].

2.4 Toxicity of Nanomaterials and Physicochemical Parameters

An awareness of nanotoxicity has originated from the similarity in the high-aspect-ratio structure of CNTs and asbestos. Aspect ratio is the ratio of the longer dimension to the shorter dimension for a two-dimensional shape. Asbestos refer to a mineral fiber that has been used as heat insulation materials, roofing materials, and pipe in cement building construction. It is well-known that inhalation or ingestion of asbestos can lead to a long-term risk of lung cancer [OSHA]. The long thin dimensions of asbestos enable them to permanently deposit to the deepest part of lung resulting in lower gas exchange functions and a high chance of lung cancer. CNTs, with similar fibrous shape, could possibly be as toxic as asbestos. In this case, shape is considered as a factor affecting the toxicity of CNTs. Shape and other physical properties including size, structure, and surface area which affect the chemical reactivity between nanomaterials and the host environment are commonly referred to the term *physicochemical parameters*. These parameters and the

chemical composition of the materials are the key factor determining the toxicity of nanomaterials on biological systems.

The physical properties of nanomaterials such as size, shape, and structure can affect the biological activity and the uptake of nanoparticles by human via respiratory tract and skin. According to the previous experimental study, the parameters can affect the deposition pattern of nanomaterials in the respiratory tract resulting in different degree of adverse health effects which include immune-system malfunction, oxidative stress related disorders, lung disease, and cells inflammation [Oberdorster et al., 2005[a]]. A good understanding in the relationship between the nanomaterials physicochemical parameters and toxicity is essential in developing toxic screening strategies at the very beginning of the product life cycle.

The correlation between the physicochemical parameters and toxicological response of nanomaterials presented in this dissertation is based on the results of the previous toxicology studies which have been carried out with the aid of *in vivo* and/or *in vitro* tests. The results of these small-scale tests can be extrapolated to estimate the real effect on human and ecosystem. However, it must be noted that most of the literature on nanotoxicological data, which is derived from *in vivo* and *in vitro* tests, is limited to short-term effects. The duration of *in vitro* test is usually less than a day while the duration of *in vivo* is limited to the life span of the tested animals.

"*In vivo*" means within a living organism. In biological toxicity study, *in vivo* tests are an experiment occurring in a living body which is simply called "animal test". Inexpensive and fast-breeding animals commonly used in *in vivo* test are guinea pig, rat, mice, bird, and invertebrates. *In vivo* tests are primarily design for human drug testing.

The test duration ranges from short-term dosing to lifetime of the tested animal. *In vivo* tests can be used to determine the degree of absorption via inhalation, dermal, or oral exposure and the magnitude of the toxicity. The measured *in vivo* toxic is then subjected to animal-to-human extrapolation.

In vitro refers to manipulation of living cells, organs, tissues, and biomolecules in a test tube or in a controlled environment outside a living organism. The cell is the smallest unit of life in our bodies. Each cell is composed of an array of biomolecules. Any manipulation that breaks down the cell into its non-living components is considered an *in vitro* approach. The advantages of *in vitro* tests are that they are quick, relatively inexpensive, and specific mechanisms of action can be tested. The disadvantage of these tests is that the homeostatic mechanisms and pathways found in animals are not present. Therefore, the ability to determine injury repair in the same system in which toxicity is tested is very limited.

2.4.1 Particle Size and Surface Area

Previous nanotoxicology studies have consistently reported that the toxic effects attributed to the exposure of nanoparticles are size-dependent [Nel et al., 2006, Oberdorster et al., 2005[b]]. As particle size decreases and becomes less than 100 nm, the surface molecules increase exponentially as depicted in Figure 2.4.

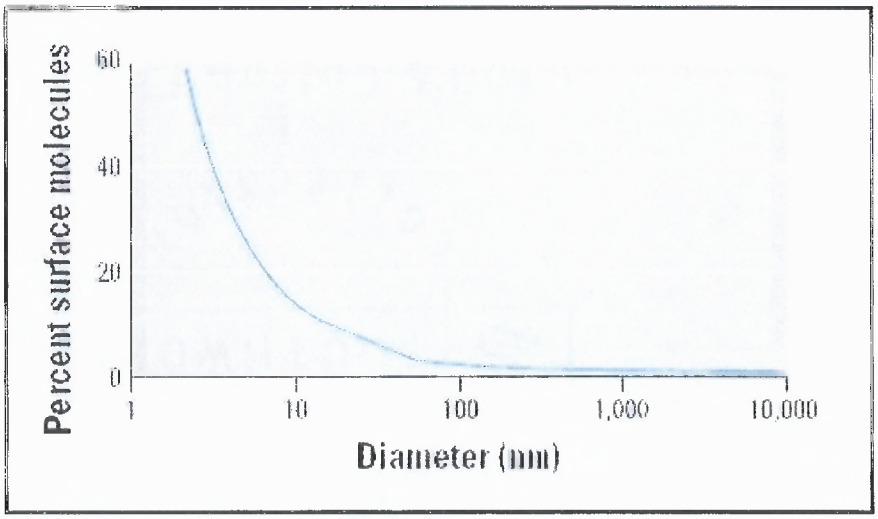

Figure 2.4 Surface molecules as a function of particle size.
Source: [Oberdorster et al., 2005 [b]]

Given the same mass, the higher surface area enhances the material with a much higher chemical reactivity and potential toxicity. The ability to cause adverse effects to human such as lung injuries of nanoparticles (or ultrafine particles) comparing with fine particles (>100nm but still respirable) has now been shown for a number of Li-ion electrode materials as summarized in Table 2.3. According to these experimental studies, ultrafine particles are more toxic to human than fine particles.

Table 2.3 Comparative Toxicity of Ultrafine Particles to Fine Particles

Material	Ultrafine particle (<100 nm) over fine particle (>100 nm)	Testing Methodology
TiO_2	Higher inflammatory response in the lung cells[1]	in vivo (rats), 12 weeks
	Prolonged retention of the particles, Cell proliferation[1]	in vivo (rats), 1 year
TiO_2, Carbon Black	Airway inflammation and immune adjuvant activity found in the ultrafine only[2]	in vivo (mice), 8 days to 28 days
Carbon Black	greater proinflammatory activity and oxidative stress at low mass dose[3]	in vivo (rats), 6 hours to 7 days
	Greater inflammatory response[4]	in vivo (rats), 6 hours
Cobalt (Co)	More toxic to lower respiratory tract[5]	in vivo (rats), 1-30 days
Vanadium Oxide (V_2O_3)	Greater reduction in cell viability (10 time stonger), much stronger extent of lipid peroxidation in macrophages[6]	in vitro (epithelial lung cells)
Nickel (Ni)	more severe pulmonary imflammation[7]	in vivo (rats), 1-30 days
Amorphous Silica (Colloidal)	more severe acute pulmonary imflammation and tissue injury[8]	in vivo (mice), 30 min to 24 hours

Source: [1] [Oberdorster et al., 1994]; [2] [De Haar et al., 2006]; [3] [Li et al., 1999]; [4] [Li et al., 1996]; [5] [Zhang et al., 2000 [b]]; [6] [Worle-Knirsch et al., 2007]; [7] [Zhang et al., 2003]; [8] [Kaewamatawong et al., 2005]

Low-toxicity material may present greater toxic hazard at nanoscale. Nanoparticles of polystyrene, solid plastic which is a raw material for electronic and consumer products such as computer housing, foam packaging , and clear drinking cup, cause significant cell death in *in vivo* and *in vitro* tests [Brown et al., 2001]. Copper is another low-toxicity material which displays moderately toxic effect at nanoscale in *in vivo* test. The pathological examinations revealed that kidney, liver, and spleen are target organs for nano-copper particles and the main parameter inducing the toxicological effects is the high surface area of nano-copper particles [Chen et al., 2006].

Scientists have studied the potential use of carbonaceous nanomaterials, especially MWNTs, in Li-ion batteries as anode materials. Surface area, which is a key factor influencing electrochemical property of CNTs as lithium/lithium ion absorber, is also the parameter that best predicts the pulmonary toxicity of CNTs and other carbonaceous nanomaterials. Reported by the previous toxicological study, SWNTs yield

the strongest adverse effect to human cells, when compared with other carbonaceous nanomaterials, due to their largest surface area per volume ratio [Tian et al., 2006].

Particle size is also a critical parameter affecting the distribution of nanomaterials in the body. According to the model created by ICRP (International Commission on Radiological Protection) which is used to predict the deposition of particles in human respiratory tract, the deposition of orally inhaled particles in four regions of the respiratory tract is mainly affected by the particle size. The distance nanoparticles travel increases with decreasing particle size and increasing respiratory cycle period (decreasing respiratory rate) [Heyder, 2004].

2.4.2 Oxidative Stress

The term *oxidative stress* and *free radical* have been considered as a factor affecting nanomaterials toxicity. In general, an atom is surrounded by even number of electrons at the outer ring. When one of the electrons is lost, a free radical which is chemically reactive and highly unstable occurs. When encounter with cells, the chemical activity can cause biological damage, frequently referred to as oxidative damage, to cells which is the cause of cell death, cell mutation, cancer, and bodily disorders. Oxidative stress occurs when the availability of body's antioxidant is insufficient to neutralize free radicals.

The ability to generate free radicals has been suggested by previous toxicological study as a metric for assessing toxicity of nanomaterials and ultrafine particles [Donaldson et al, 2003; Nel et al., 2006]. Cobalt is known to be more toxic than nickel in term of lung disease. However, in vitro study revealed that ultrafine particles of nickel are more toxic to human lung than ultrafine particles of cobalt and TiO_2 due to their superior ability to generate free radicals and oxidative damage [Zhang et al., 1998].

2.4.3 Particle Structure

High aspect ratio nanomaterials such as CNTs could be as toxic as asbestos due to the similarity in their fibrous shape [Hazards Magazine, Donaldson and Tran, 2004]. Previous in vitro study indicates that aspect ratio (frequently referred to length) is one of the parameters affecting the toxicity of fibrous-formed carbonaceous nanomaterials such as CNTs and carbon nanofibers [Magrez et al., 2006]. However, at presence, the correlation between nanomaterials length and their toxicity is still inconclusive due to the uptake and clearance mechanisms.

The clearance mechanism in human lung is the process in which the deposited particle is removed by defensive agents such as alveolar macrophage. Short fiber can be easily cleared by the defensive agents comparing to the long fiber [Donaldson et al., 2006]. Shorter length also allows a better distribution of the particles in the lungs avoiding the aggregation of particles which is the cause of acute lung inflammation [Muller et al., 2005]. On the other hand, shorter fiber may be more toxic to human lung cell according to the toxicity study of DNA-wrapped SWNTs by Becker et al [Becker et al., 2007]. Their *in vitro* test suggests that short tube (less than about 200 nm in length) yields higher cellular uptake rate and could be more toxic than long tube.

2.4.4 Solubility

CNTs are an example of toxic nanomaterials which are insoluble in their native state. It is well-known that highly water-soluble chemicals are less likely to interact with organic material. Researchers at Rice University and elsewhere have developed processing methods for dissolving CNTs in organic solution [Nanotech News, 2005]. The surface structure of CNTs is modified by chemical processes. Research on the solubility of CNTs

and their cytotoxicity has been conducted for their medical applications. In vitro study by Dumortier et al illustrates that this water-soluble CNTs post no toxic effect to human's primary immune cells [Dumortier et al., 2006].

Solubility is an important parameter that affects the toxicity of nanomaterials in human body and water-based environment. The distinction of nanomaterials based on their solubility is a future research task.

2.4.5 Impurity

Toxic effect may be caused by impurities. Commercially available CNTs are an example of nanomaterials which always come with traces of impurities. Previous toxicity study shows that impurities in SWNTs are the cause of higher mortality rates in aquatic animals such as copepod [Templeton et al., 2006].

CNTs are thermally generated and their production always yields some amount of residual material such as ash or amorphous carbon. Additionally, growing mechanism of SWNTs involves the hydrocarbon decomposition on supported metal catalysts (Co, Fe, Ni, and Mo). These metal catalysts are prepared on the substrate which usually made of alumina, magnesium oxide or silica. Although MWNTs can be produced without metal catalysts, the presence of a small amount of metal catalysts helps to align the nanotubes [Lam et al., 2006]. In general, unpurified CNTs contain large amount of residual metal, support material, and ash. These residual materials can partially be removed by purification process. The remaining amount serves as additional toxic to CNTs and contaminates the result in many toxicity experiments. Gold nanorods are another example of nanomaterials that are toxic due to the process-related impurities. The presence of toxic chemical agents used by surfactant-assisted growth method, which is a common

processing technique for gold nanorods, in the produced nanorod can cause severe toxic effects on human skin cell [Wang et al., 2008].

2.5 Random Motion of Nanoparticles

The motion of nanoparticles and very fine particles suspended in a gas or fluid has been found to be random. This random motion, frequently referred to as Brownian motion, occurs when a particle is continually collided with air molecule. According to kinetic theory, as the particle size, mass, and density decrease, particles move at a higher velocity resulting in a longer travel distance. As shown in Figure 2.5, the Brownian displacement of spherical particles exponentially increases when the particle's diameter is less than 1 micron or 1000 nm.

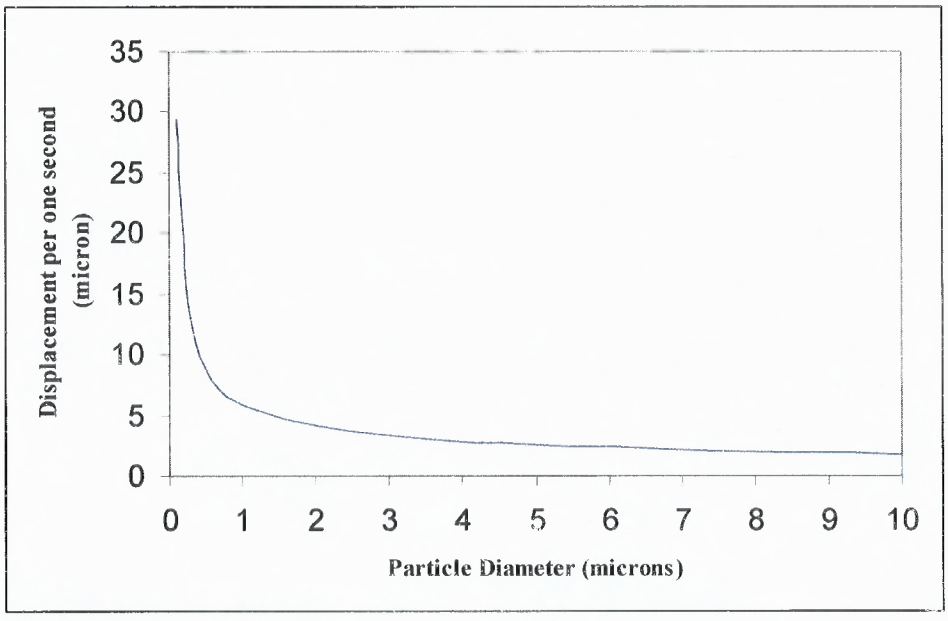

Figure 2.5 Displacement of spherical particles suspended in air at 70 °F.
Source: [Lapple, 1951]

The particle's velocity is also dependent on the temperature and the viscosity of the surrounding medium. Particles in air travel at a higher velocity compared to particles in liquid. At elevated temperature, air or liquid molecules travel at higher velocity causing collided particles to move at higher velocity.

Preliminary research has found that the filtration efficiency of nanoparticles can be affected by the random motion of nanoparticles [Shin et al., 2008]. A small change in filtration efficiency with temperature was observed. The description on the process impacts due to the random motion of nanoparticles are given in Chapter 4 of the dissertation.

2.6 Melting Behavior of Nanomaterials

Surface melting of nanoparticles has been studied extensively during the past decade. The melting point and the onset temperature of evaporation of nanoparticles have been demonstrated to be different from that of their bulk forms due to their large surface-to-volume ratio and surface melting mechanism. At the same time, melting and evaporation are the key operation for high temperature recycling process for rechargeable batteries and electronic products.

While nanomaterials are being used for cost and energy saving at the production and use stages, variation in the melting temperature of nanomaterials could lead to the composition change of metallurgy waste, purity deterioration of the reclaimed metals, and unintentional release of nanomaterials into the environment at the EOL stage. Hence, the information on the melting behavior of nanomaterials must be fully recognized as nanomaterials-contained batteries are entering into the waste stream. This part of the

dissertation addresses the anomalous melting and evaporation behaviors of nanoparticles/nanomaterials and their potentially undesirable consequences surrounding the recycling process.

2.6.1 Melting Point Depression

The melting point, the transition temperature between solid and liquid phase, of bulk materials is not size dependent. However, for free-standing nanoparticles, their melting point decreases with decreasing particle size [Qi, 2005; Goldstein et al., 1992]. This melting phenomenon is commonly called melting point depression or supercooling. The size and shape of nanoparticles are the main factors affecting the degree of melting point depression.

Melting process starts at the surface atoms due to their lower thermal stability relative to the interior atoms. The smaller a particle becomes, the more the percentage of surface atom increases. Therefore, when applying external heat energy, the melting process of nanoparticles starts at a temperature lower than that of their bulk form. Nanostructured titanium dioxide (also known as titania), electrode materials for nano-enabled Li-ion batteries commercialized by A123Systems [A123Systems] and Altairnano [Altairnano], also exhibit large melting point depression. At their bulk form, the melting point of titanium and zinc are 1690 °C and 419.5 °C, respectively. Large melting point depression is observed in the mixture of nano-scaled titanium dioxide and zinc oxide with the new melting point below 200°C [Wang, 2005]. Melting point depression is also observed in nanostructured tin, electrode materials for Sony's nano-enabled Li-ion batteries [Sony]. According to the experiment result by Bachel et al. [Bachels et al., 2000], the melting point of isolated tin nanoparticles, with the mean size of about 500

atoms and the radius ranging from 5-50 nm, was found to be lowered by 125 °C comparing to the bulk (around 230 °C).

Shape is another factor affecting the degree of melting point depression in free-standing nanoparticles due to the fact that different surface area is yielded by particles with different shape and the degree of melting point depression in nanoparticles is induced by the large surface-to-volume ratio. In most melting studies, nanoparticles are regarded as ideal spheres. In fact, nanoparticles made from the same materials are available in a variety of shapes depending on the synthesis techniques.

The surface area of non-spherical nanoparticles is always larger than that of spherical nanoparticles. Then, researchers use shape factor to account for the particle shape difference between the spherical and non-spherical nanoparticles [Qi and Wang, 2004; Gupta et al., 2008]. The shape factor is a ratio of the surface area of a non-spherical nanoparticle to that of a spherical nanoparticle in the identical volume. The shape factor of spherical nanoparticles is one and the shape factor of non-spherical nanoparticles is larger than one as shown in Table 2.4. The higher degree of melting point depression is exhibited in free-standing nanoparticles with higher value of the shape factor. Furthermore, the shape becomes larger with decreasing of the particle size due to the higher number of surface atoms.

Table 2.4 Shape Factor of Nanoparticles

Particle shape	Shape factor (α)
Spherical	1
Regular tetrahedral	1.49
Regular hexahedral	1.24
Regular octahedral	1.18
Disk-like	>1.15

Source: [Qi et al., 2005]

Nanomaterials made of materials with melting point higher than the reduction temperature may be melted at the reduction process as a result of melting point depression. This premelting may disrupt the oxidation-reduction reaction which starts only when the reduction temperature is reached. In addition, this may disrupt the handling and transportation of sponge iron.

2.6.2 Melting Point Elevation

On the other hand, melting point elevation or superheating can be observed when nanoparticles are coated or encapsulated within higher-melting-point host matrices [Rosner and Wilde, 2006]. The degree of superheating is strongly dependent on the types of the interface between them. Moreover, in the environment where superheating occurs, particle size and shape serve as additional factors affecting the degree of superheating.

In term of crystal structure, the interface can be classified as incoherent, semi-coherent, and coherent interfaces. High degree of superheating has been reported in materials with epitaxial (coherent or semicoherent) interface [Mei et al., 2004; Jin et al., 1999]. Epitaxial interface occurs when one material is oriented overgrown on a substrate or another material. Examples of nanomaterials with epitaxial interface are coated nanoparticles and confined thin film [Zhang et al., 2006; Zhang et al., 2000[a]]. Melting process starts with atomic vibration at the particle's surface. Epitaxial interface, the highly ordered interface between the nanoparticles and the host matrix, results in the depression of the atomic vibration amplitude and hence the melting point elevation of the confined nanoparticles.

In most cases, epitaxial interface plays a key role in elevating the melting point of encapsulated nanoparticles. However, pressure-induced melting point elevation can occur in system with incoherent interface when there is a huge difference in thermal expansion coefficients between the nanoparticles and the host matrix. Pressure-induced melting point elevation was experimentally observed in metallic nanoparticles embedded in a rigid ceramic or carbon matrix [Banhart et al., 2003].

The degree of superheating of encapsulated nanoparticles is found to be size dependent. Previous studies show that higher degree of superheating is observed in smaller nanoparticles [Zhong et al., 2001; Lu and Jin, 2001]. With decreasing particle size, the surface area is higher resulting in a larger number of surface atoms epitaxially bonded with the host matrix and therefore the higher degree of superheating. For the shape effect, the mechanism of the effect is analogous to that of melting point depression. Higher degree of superheating will occur in nanoparticles with shape that generate higher surface area [Qi and Wang, 2005].

The concern for unusual melting behavior of nanomaterials is critical to understanding impacts during recycling since melting is the primary behavior in the HTMR. High-temperature processing of superheated nanomaterials with unusually high melting point will require higher smelting temperatures which results in higher energy consumption and increased air emissions, including the possibility of nanomaterials escaping through the process filtration system.

2.7 Specific Heat Capacity of Nanomaterials

Specific heat capacity, C_p, is the amount of heat energy, Q, required to raise the temperature of one unit mass of substance by one degree. The relationship between specific heat capacity and temperature change, ΔT, can be expressed as shown in Equation 2.1 where m is the mass of substance.

$$Q = mC_p\Delta T \tag{2.1}$$

Most of the previous studies on thermal properties of nanomaterials have shown that the specific heat capacity of nanomaterials is higher than that of the corresponding bulk materials at low temperature range (lower than about 400 K) as shown in Table 2.4. This phenomenon is commonly called *heat capacity enhancement* or *excess heat capacity* of nanomaterials. In this dissertation, the term *specific heat capacity enhancement* will be used.

The specific heat capacity enhancement of nanoparticles is due to their unique physical characteristics, irrespective of chemical composition. The irregular geometric shape and low number of atoms in nanoparticles are responsible for their vibration spectrum which is different from that of the microscopic counterpart [Likhachev et al., 2006].

As shown in Table 2.4, experimental studies reveal that specific heat capacity of nanomaterials increases with decreasing size for metallic nanocrystals, nanostructured metal oxides, nanostructured silicon dioxide (SiO_2), and CNTs. For nanocomposites where CNTs are homogenously distributed within microstuctured material, previous study has shown that the specific heat capacity of the nanocomposite increases as the

percent content of the reinforced CNTs increases [Kumari et al., 2008]. Most of the nanomaterials shown in Table 2.5 are being developed by battery manufacturers and academic researchers as described in the previous section of Chapter 2.

Table 2.5 Specific Heat Capacity Enhancement of Nanomaterials

Materials		Size	% Heat Capacity Enhancement	Temperature	Studies
Metallic	Nanocrystalline Cu	8 nm	10%	150-300 K	Rupp and Birringer, 1987
	Nanocrystalline Pd	6 nm	40%	150-300 K	
	Nanocrystalline Ni	40 nm	2 - 4%	100-370 K	Wang et al., 2001[c]
	Nanocrystalline Fe	87 nm	8 - 14%	79-371 K	Wang et al., 2002
	Nanocrystalline Selenium	10 nm	2%	250-375 K	Sun and Lu, 1996
	Nanocrystalline Fe Co Cr	20 - 75 nm	20 - 50%	up to 470 K	Révész and Lendvai, 1998
	Nanocrystalline Fe	10 nm	120%	325-375 K	Lin et al., 1992
Metal Oxides	Nanocrystalline TiO_2	14 nm	26%	78-370 K	Wu et al., 2000
	Nanopowder Al_2O_3	20 nm	6 - 23%	78-370 K	Wang et al., 2001[b]
Metalloids	Amorphous SiO_2	20 nm	less than 10%	150-350 K	Wang et al., 2001[a]
	SiO_2 thin film	1-5 nm in thickness	evidently smaller than the bulk value	100-600 K	Tang et al., 2005
CNTs	DWCNTs	1.6 nm (outer tube) and 1 nm (inner tube) with >2μm in length	significantly higher than the C_p of graphite	320-560 K	Silva et al., 2009
	SWCNTs	2 nm	slightly higher than the C_p of graphite	320-470 K	
	CNTs nanocomposite	10 - 40 nm in diameter, 1 - 7 μm in length, and 7 - 19% of CNT content by weight	up to 318% increase in C_p at 370 K	330-670 K	Kumari et al., 2008

The specific heat capacity enhancement can also be explained by the change in Gibbs free energy of nanomaterials. As opposed to their corresponding bulk materials, nanomaterials possess higher specific heat capacity due to their higher free energy [Wu et al., 2001]. Based on the theory of surface energy, the higher surface area per volume of

nanomaterials enhances nanomaterials with higher levels of Gibbs free energy, *G*. Then, according to Equations 2.1 and 2.2 (Gibbs free energy equation) under adiabatic and constant pressure and volume conditions, the higher level of Gibbs free energy of nanomaterials corresponds to a higher level of enthalpy, heat content, and specific heat capacity as compared with their bulk counterpart.

$$G = H - T\,S \tag{2.2}$$

As a result, according to Equation 2.1, it is anticipated that the amount of energy consumed by the HTMR process in raising the temperature of nanomaterials-containing Li-ion batteries may be significantly higher, depending primarily on the amount of nanomaterials in the batteries and the degree of specific heat capacity enhancement. This behavior may also result in longer operating times and increased waste gas emissions by the HTMR process.

To analyze the impacts of superheating and specific heat capacity enhancement of nanomaterials on the HTMR process, the details of recycling technologies for rechargeable batteries focusing on the HTMR process are given in the following section. After that, the potential process and environmental impacts due to melting point elevation and specific heat capacity enhancement are analyzed in Chapter 5. By using thermodynamic and LCA techniques, the amount of energy loss, exergy loss, and green house gas emissions from the process is calculated and used as an environmental impact indicator.

2.8 Background Information on the End-of-Life (EOL) Management and Recycling Process of Rechargeable Batteries

According to the previous LCA study, recycling of batteries gives environmental benefit due to the recovery of metals and environmentally sound management of toxic chemicals [Parsons, 2007]. Batteries collected for recycle can be classified as primary and secondary (rechargeable) batteries. Following the case study, this part of the dissertation examines the recycling process for rechargeable batteries focusing on Li-ion batteries.

In the United States, most of spent Li-ion and other rechargeable batteries are recycled through the program administered by the Rechargeable Battery Recycling Corporation (RBRC). The program is design to recycle small, sealed, Nickel Cadmium (Ni-Cd), Nickel Metal Hydride (Ni-MH), Li-ion and lead (Pb) batteries. RBRC collects, sorts, and sends the batteries for recycling at different facilities. Inmetco and Toxco are RBRC recycling facilities that use pyrometallurgical and hydrometallurgical recovery process, respectively. These two recycling methods are also employed by other battery recycling companies that recycle Li-ion and other type of rechargeable batteries outside the United States as shown in Table 2.6.

Table 2.6 Rechargeable Battery Recycling Organizations and Technologies

Organization or Technology	Pyrometallurgy	Hydrometallurgy	Country	Rechargeable batteries accected for recycling
Accurec[1]	✓		Germany	NiCd, NiMH, Li, and Li-ion
AEA Technology[2]		✓	Scotland	Lead-acid, NiCd, NiMh, Li-ion
BATENUS[3]		✓	Germany	NiCd, Li, and Li-ion
Batrec AG[4]	✓		Switzerland	NiCd, NiMH, Lead, Li, and Li-ion
Citron[5]	✓		France	NiMH, Li-Ion, NiCd and lead batteries
Recupyl[6]		✓	France	Li and Li-ion
Snam-Savam[7]	✓		France	NiCd, NiMH, and Li-ion
Sumitomo[8]	✓		Japan	Li-ion

Source: [1] [Accurec]; [2] [Lain, 2001]; [3] [Frohlich and Sewing, 1995]; [4] [Batrec]; [5] [Citron]; [6] [Recupyl]; [7] [SNAM]; [8] [Frenay et al., 1994]

2.8.1 Pyrometallurgical Recovery Process

Pyrometallurgical recovery process is a process that uses physical and chemical reactions at elevated temperatures for extraction and separation of valuable metals. Both battery and non-battery wastes can be recycled through pyrometallurgical recovery process. Regularly processed types of battery include nickel cadmium, nickel iron, nickel metal hydride, Li-ion and mercury-free zinc carbon. For non-battery waste, recycled materials are iron and steelworks waste such as furnace dust, mill scale, and swarf [Bauer et al., 1990].

The process is often referred to as high-temperature metals recovery (HTMR) process As shown in Figure 2.6, the battery recycling process is a high-temperature operation composed of four primary steps: material size reduction, chemical and thermal reduction, smelting, and casting.

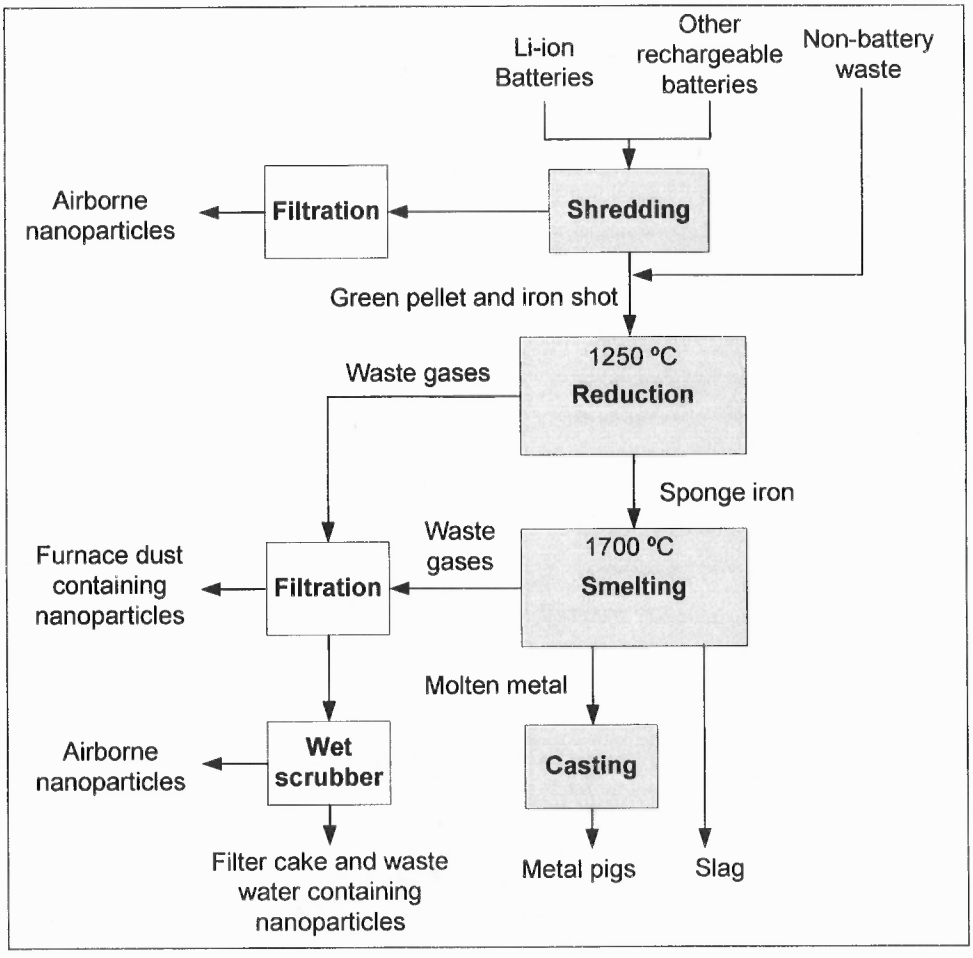

Figure 2.6 Process diagram for the HTMR process.

In the first process step, the batteries are mechanically shredded into small pieces using traditional shredders and hammer mills. Prior to the reduction process, the shredded material may be mixed with other non-battery scrap material and reducing agents, such as coke or coal. The desired composition of reclaimed metals is controlled by the composition of mixed feed materials.

The reduction process relies on both thermal and chemical reactions. In the process, the feed materials, containing significant carbon content, are heated to the reduction temperature (about 1250 °C) in a Rotary Hearth Furnace (RHF) [Bauer et al., 1990]. At this point, the high temperature causes an oxidation-reduction reaction to occur where the metal oxides release oxygen to the carbon. As a result, metal oxides are converted into metallic forms and carbon monoxide or carbon dioxide gases are released. Simultaneously, the vaporized volatile metals, such as zinc and cadmium, are drawn from the furnace. The furnace dust generated by the solidification of these metals, as the waste gas cools, is collected by the filtration system. The filtered waste gas is then diverted into the wet scrubber system where the scrubber water is treated and sent to the next process for metal recovery. The hot reduced feed from the RHF is transferred to the Submerged Electric Arc Furnace (SEAF) where they are smelted for the extraction of the metal components.

An electric arc furnace (EAF) is generally used in the smelting process to transform the reduced metals into a molten metal alloy of nickel, chromium, iron, and other metals. EAF applies heat to the waste or metal scrap by converting electric power into heat through graphite electrodes. The heating mechanism requires large amount of power (360 to 400 kWh of electricity to melt a ton of steel [Jeremy, 1997]). The reduced

waste may be combined with other steel wastes depending on the composition requirement. At the end of each batch cycle, a molten metal alloy and slag are formed at approximately 1700 °C and tapped out [Steeluniversity]. The discharged by-products include slag and heavy-metal dust (EAF dust). Molten metal alloy are sent to the next process for casting. Non-hazardous slag can be used in road construction. EAF dust is considered as hazardous waste which is sent for further waste treatment [Keegel, Jr., 1996]. It must be noted that the reduction and smelting temperatures may vary depending on the specific composition of the materials being recycled.

At the final process, the molten metal is cast into pigs which are an alloy of nickel, chromium, and iron. Pigs are sent to specialty steel mills to be used as stainless steel remelt alloy [Hanewald et al., 1996].

2.8.2 Hydrometallurgical Recovery Process

Hydrometallurgical recovery process consists of comminuting and chemical leaching processes where metals are extracted into an aqueous solution and subsequently recovered by methods such as electrolysis and precipitation. The process consumes significantly less amount of energy comparing to the pyrometallurgical recovery process which uses high-temperature treatments in extracting metals. Moreover, the process is performed without the emission of hazardous gas.

Toxco is an example of recycling companies in North America whose recycling process has been developed based on hydrometallurgical technique. Both primary and secondary batteries can be recycled at Toxco. Their process can recycle any size or type of lithium-based battery. Li-ion, lithium metal, and alkaline batteries are recycled together at its recovery plant located at Trial, British Columbia, Canada [Toxco]. The

primary metals recovered are zinc and manganese from alkaline as well as lithium and cobalt from lithium-based batteries. Other metals recovered are ferrous and nonferrous metals such as aluminum, tin, brass, copper, and steel.

Due to the waste composition of lithium metal, the recycling process begins with the cryogenic treatment (cooling process) in which the lithium containing waste is submerged into liquid nitrogen or liquid argon until its temperature reaches the cryogenic temperatures (about -180 °C) [McLaughlin, 1994]. Lithium, which is explosively reactive at room temperature, becomes many folds less reactive at this substantially low temperature. The waste can then be safely comminuted by using shredder or hammer mill.

At this point, the desired metals are selectively extracted from the comminuted waste as it undergoes a series of leaching operation. The comminuted waste is commonly mixed with water to form a solution. The solution is then treated by a multi-stage pH-adjustment treatment. At each stage, the solution is maintained at a different pH level to form different precipitates containing the desired metals. The chemical used to control the pH level is selected based on the desired form of final product. Commonly used chemicals are calcium carbonate, lime, and sodium hydroxide (NaOH) [Lloyd, 1998]. Lithium reclamation process by Toxco is an example of such the leaching process where lithium hydroxide (LiOH) is used to control the pH level when lithium carbonate ($LiCO_3$) is a designated product [McLaughlin, 1999].

After leaching, the solution which contains precipitates or salts of the desired metals is purified in order to remove the undesirable components. The preliminary purification can be performed by using precipitation techniques. The remaining impurities can be removed by using fine purification techniques such as solvent extraction and ion exchange [Waseda and Isshiki, 2001].

The final step, metal recovery, is commonly carried out by means of precipitation or electrolysis. By precipitation, the purified solution reacts with chemicals to precipitate. For electrolysis, the desired metal is extracted by passing electrical charge through the solution. As a result, the desired metal is deposited at the cathode.

2.9 Life Cycle Assessment Studies

The fast-growing use of nanomaterials in consumer products has raised concern regarding unknown risks to human health and environment. As shown in Table 2.7, prior LCA studies have focused on the economic viability of nanotechnology in light of the environmental burden. The economic and environmental comparison of SWNTs production techniques performed by research group at Northern Eastern University [Isaacs et al., 2006; Healy et al., 2008] concludes that electricity consumption is the major contributor to the environmental burden associated with SWNTs production. Ohio State University [Khanna et al., 2007, 2008] uses an LCA approach to analyze and compare life cycle energy intensity and environmental burden between the production of carbon nanofibers (CNFs) and other materials including aluminum, steel, and polypropylene. Without considering the toxicity of CNFs themselves, their result still indicates significantly higher energy requirement and higher environmental impact of

CNFs as compared to other materials. Other nanomaterials productions studied by LCA practitioners include titanium dioxide nanoparticles [Grubb and Bakshi, 2008] and carbon nanoparticles production [Kushnir and Sanden, 2008]. These studies are a "cradle-to-gate" analysis of nanomaterials synthesis.

For nanoproducts, researchers used LCA to estimate the impacts from substituting a nanocomposite for steel in automobile body panels [Lloyd and Lave, 2003; Khanna and Bakshi, 2009] and, also, the impact of using a nanofabrication technique for catalytic converters in automobiles [Lloyd et al., 2005]. Their results suggest that large energy consumption at the production stage is outweighed by the saving in raw materials at the production stage and a higher product performance at the use stage. Roe et al. evaluated the environmental impacts and cost throughout the life cycle of polypropylene nanocomposite products including packaging film, agricultural film, and automobile body panels. Their study shows that nanomaterials offer raw material saving opportunity which may result in the reduction of life cycle cost and environmental impacts [Roes et al., 2007]. However, the scope of their work is still limited to the material synthesis, production, and use stages without considering the EOL stage.

As nanomaterial toxicity data is becoming available, recent research has begun to emphasize the release of nanomaterials and the impacts based on their toxicity throughout the life cycle. A recent LCA study on Li-ion batteries and synthetic textile made of CNTs by Kohler et al. shows that CNTs could be released at different life cycle phase ranging from the processing of CNTS, production, usage and disposal phases of CNTs applications [Kohler et al., 2008].

Table 2.7 Summary of Life Cycle Assessments on Nanotechnology

Study	Process/Material/Product	Life Cycle Stages	Approach
Isaacs et al., 2006	SWNTs	Material synthesis	LCA and life cycle cost analysis
Healy et al., 2008	SWNTs	Material synthesis	LCA
Khanna et al., 2007, 2008	Carbon nanofiber production	Material synthesis, production, use phase	Process LCA
Grubb and Bakshi, 2008	Titanium dioxide nanoparticles	Material synthesis	Thermodynamic analysis, LCA
Kushnir and Sanden, 2008	Carbon nanoparticle production	Material synthesis	Life cycle energy analysis
Lloyd and Lave, 2003	Nanocomposite vehicle body panel	Material synthesis, production, use phase	EIO LCA
Khanna and Bakshi, 2009	Carbon nanofiber polymer composites as automotive body panels	Material synthesis, production, use phase	Life cycle energy analysis
Lloyd et al., 2005	Platinum-group metal automotive catalyst	Material synthesis, production, use phase	EIO LCA
Roes et al., 2007	Polypropylene nanocomposites as packaging film, agricultural film, vehicle body panels	Material synthesis, production, use phase	LCA and life cycle cost analysis

2.10 Discussion

This chapter of dissertation shows that the parameters which include the physical structure and chemical composition of nanomaterials have an impact on the exposure level and their ability to generate oxidative stress and toxic effects. The distribution, deposition, and translocation patterns in respiratory tract and other organisms as well as the clearance mechanism can be affected by the parameter as well. Furthermore, nanomaterials exhibit material properties and behaviors that are different than those of bulk materials. Nanomaterials properties, including melting behavior and Brownian

motion, are factors affecting the fate of nanomaterials in the high-temperature battery recycling process.

As a result, concern must be raised over the classification of nanomaterials according to the association between their properties and potential toxic effects. Characterization techniques such as scanning electron microscopy (SEM), energy-dispersive X-ray spectroscopy (EDS), and X-ray diffraction (XRD) have used by scientists to examine and classify nanomaterials according to their physical structure and chemical composition.

At the same time, characterization of nanomaterials has been performed to study the performance of nanoproducts. Sony's Nexelion and A123Systems Li-ion battery are an example of commercially available nano-enabled Li-ion batteries. According to Sony's statement, anode of nexelion cell is a material consisting of multiple elements such aş tin, cobalt, and carbon, which are mixed on a nanometer level [Sony]. Electrode material of a Nexelion cell, was examined by Army Research Laboratory by the combined use of SEM, EDS, and XRD [Wolfenstine, 2006]. According to the experimental study, anode of Nexelion is a composite consisting of graphite and amorphous tin-cobalt alloy with a mean particle size of less than one micrometer. The mean particle size of cathode material, consisting of cobalt (Co), manganese (Mn), nickel (Ni), and oxygen (O) as major elements, is also in micron range.

The next chapter of dissertation contains the details on experimental study performed at NJIT to verify the presence of nanomaterial in electrode material of A123Systems Li-ion battery. The physical structure and chemical composition of cathode material are crucial information required to improve the product design and process to prevent the unintentional release of nanomaterials.

CHAPTER 3

CHARACTERIZATION OF THE POSITIVE ELECTRODE OF AN A123SYSTEMS CELL

A new class of high-powered positive electrode materials made of nanostructured iron phosphate is being developed by A123Systems. The image of an A123Systems 26650A cell is shown in Figure 3.1. Using nanostructured iron phosphate as the cathode material prevents the battery from over-heating and possibly exploding because these materials can withstand high temperatures without releasing oxygen and thermal runaway. At the same time, A123Systems Li-ion batteries also equipped with fast charging capability while maintaining high energy density.

Figure 3.1 A123Systems 26650A cell.

In this dissertation, material characterization techniques are used to examine the positive electrode of an A123Systems 26650A cell shown in Figure 3.1. The surface topography of the positive electrode was examined at NJIT by the use of scanning electron microscopy (SEM). The chemical composition of the electrode material is determined by using energy-dispersive X-ray spectroscopy (EDS) and X-ray diffraction (XRD). Thermodynamic properties including the specific heat capacity and onset melting temperature of the electrode material is measured using differential scanning calorimetry (DSC). A 26650A cell was fully discharged and cut open as displayed in Figure 3.2. After that, the positive electrode made of aluminum foil coated with a thin film of lithium iron phosphate ($LiFePO_4$) and negative electrode made of graphite-coated copper foil were obtained for analysis.

Figure 3.2 Sample preparation for material characterization.

3.1 Structure

The SEM micrographs of the positive electrode are shown in Figure 3.3. As seen, agglomerates of nanoparticles with a size range from 10 nm to about 100 nm in diameter are found with fiber-shaped structures on the surface of the sample.

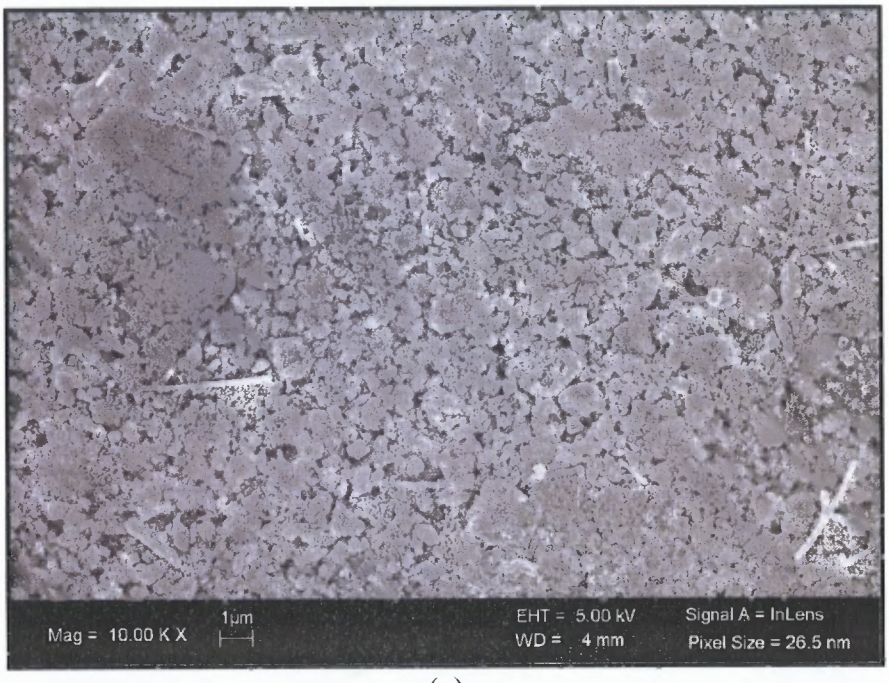

(a)

Figure 3.3 SEM images of Li-ion battery's positive electrode material.

(a) coating material consisting of iron phosphate based nanoparticles and carbon fibers, (b) carbon fibers extruded from the surface, (c - f) additional images listed in ascending order based on resolution. Product name : 26650A Manufacturer : A123Systems, Performed at NJIT York Center SEM Laboratory.

Source: [Olapiriyakul et al., 2009]

(b)

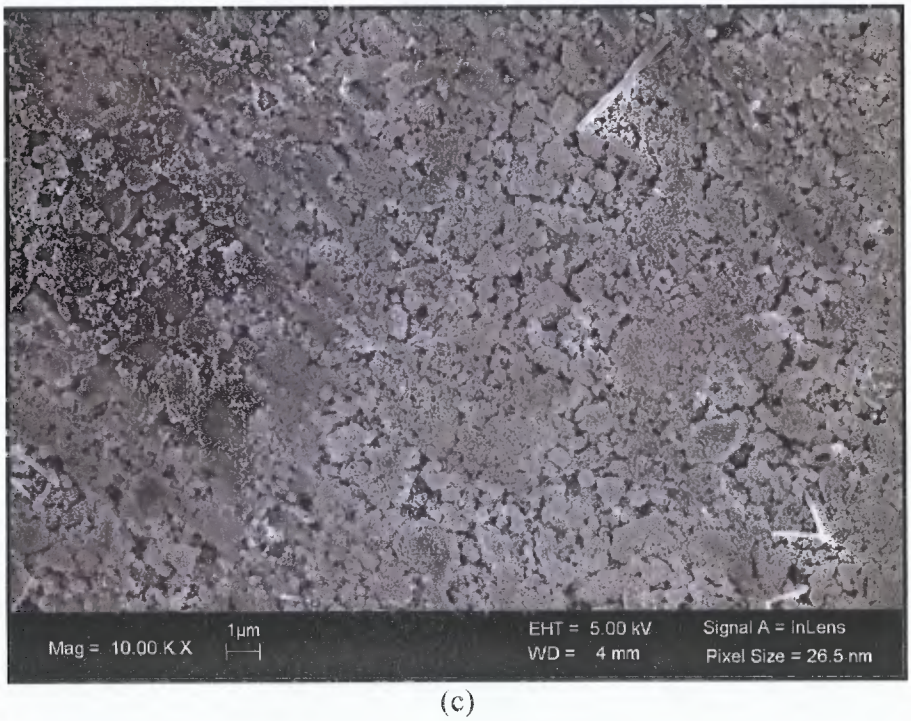

(c)

Figure 3.3 SEM images of Li-ion battery's positive electrode material. (Continued)

(a) coating material consisting of iron phosphate based nanoparticles and carbon fibers, (b) carbon fibers extruded from the surface, (c - f) additional images listed in ascending order based on resolution. Product name : 26650A Manufacturer : A123Systems, Performed at NJIT York Center SEM Laboratory.

Source: [Olapiriyakul et al., 2009]

(d)

(e)

Figure 3.3 SEM images of Li-ion battery's positive electrode material. (Continued)

(a) coating material consisting of iron phosphate based nanoparticles and carbon fibers, (b) carbon fibers extruded from the surface, (c - f) additional images listed in ascending order based on resolution. Product name : 26650A Manufacturer : A123Systems, Performed at NJIT York Center SEM Laboratory.

Source: [Olapiriyakul et al., 2009]

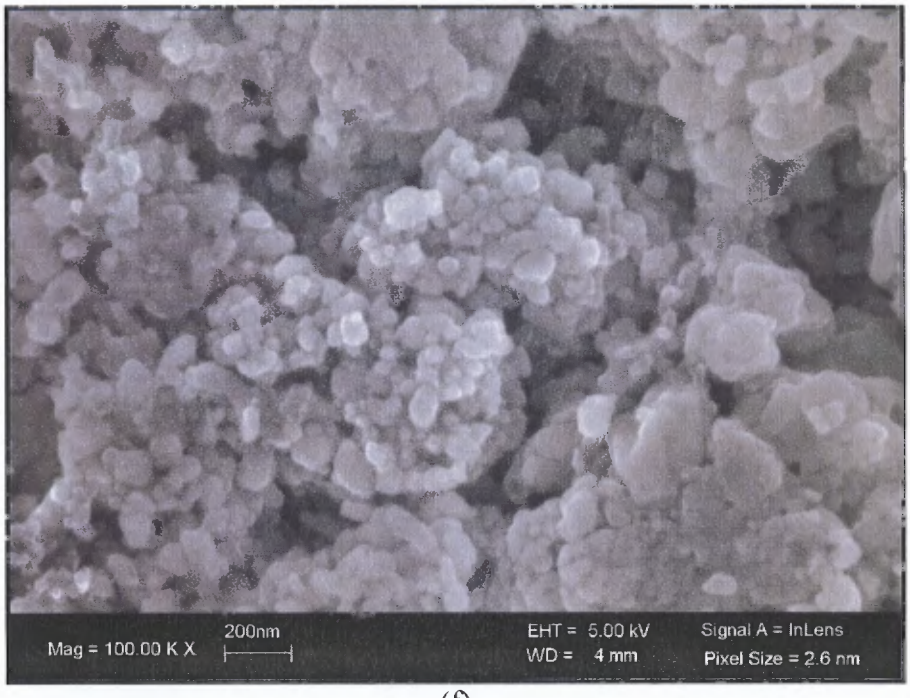

(f)

Figure 3.3 SEM images of Li-ion battery's positive electrode material. (Continued)

(a) coating material consisting of iron phosphate based nanoparticles and carbon fibers, (b) carbon fibers extruded from the surface, (c - f) additional images listed in ascending order based on resolution. Product name : 26650A Manufacturer : A123Systems, Performed at NJIT York Center SEM Laboratory.

Source: [Olapiriyakul et al., 2009]

3.2 Chemical Composition

The XRD pattern presented in Figure 3.4 shows that the positive electrode of A123Systems Li-ion is made of lithium iron phosphate ($LiFePO_4$). Table 3.1 provides additional chemical composition details from the EDS analysis showing iron, oxygen, phosphorus, and carbon to be the primary elements in terms of percentage by weight and number of atoms. The EDS results also indicate carbon as the primary composition of the fiber-shaped materials shown in Figure 3.3 (b) above. It should be noted that the EDS experimental analysis may not detect elements with low atomic number, such as lithium.

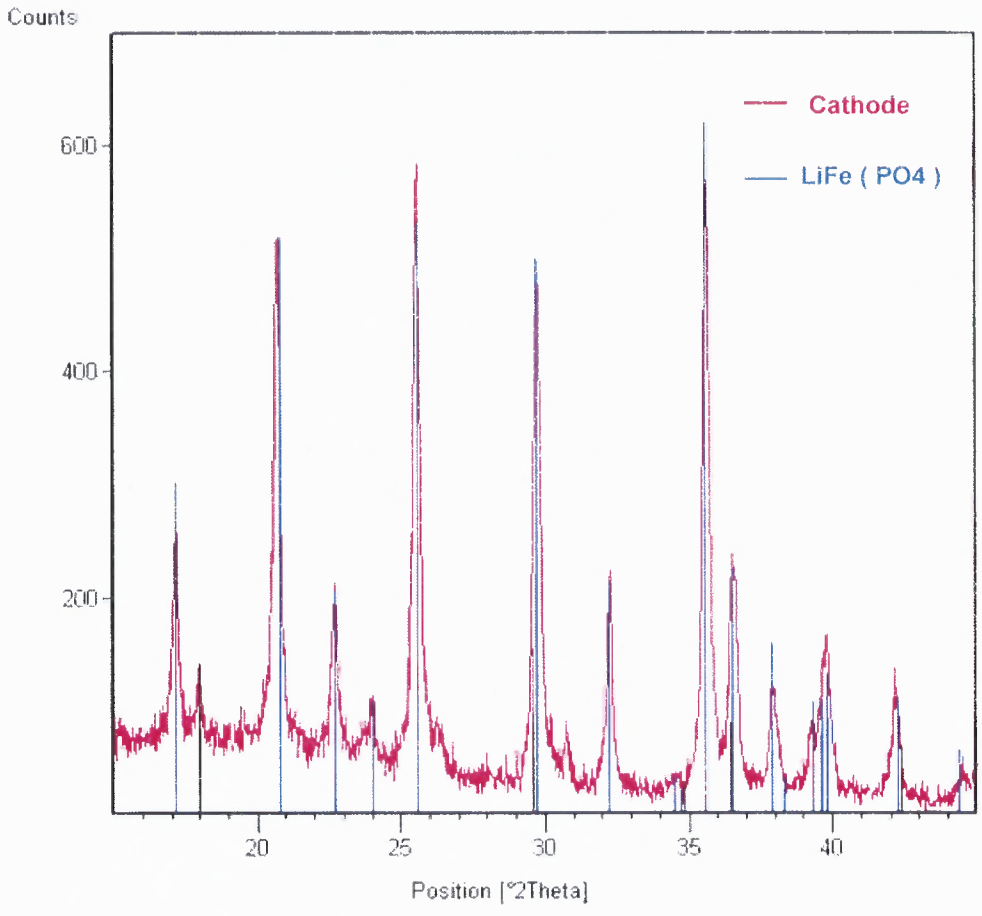

Figure 3.4 XRD patterns of A123Systems Li-ion's positive electrode.

Product name : 26650A Manufacturer : A123Systems, Performed at NJIT Colton Hall XRD Laboratory.

Source: [Olapiriyakul et al., 2009]

Table 3.1 Elemental Analysis Result by EDS

Elements	Weight %	±	Atomic %
C	15.11	0.16	26.35
O	39.49	0.16	51.72
Mg	0.10	0.05	0.09
Al	0.20	0.02	0.16
P	17.15	0.08	11.60
Fe	26.16	0.14	9.81
Co	0.16	0.08	0.06
Tb	1.64	0.21	0.22
Total	100.01		100.01

Product name : 26650A Manufacturer : A123Systems, Performed at NJIT York Center SEM Laboratory.

Source: [Olapiriyakul et al., 2009]

3.3 Specific Heat Capacity and Onset Melting Temperature

Two samples (with and without aluminum substrate) with approximately 10 mg in weight were prepared from A123Systems Li-ion's positive electrode made of thin aluminum foil coated with nanostructured $LiFePO_4$ material. Then, the specific heat capacity and onset melting temperature of the samples were measured using differential scanning calorimetry (DSC) over a temperature range between 25 °C (ambient temperature) and 550 °C (the maximum temperature of the instrument). Thermal gravimetric analysis (TGA) was performed to measure the weight loss of the samples. The experimental data on the specific heat capacity and onset melting temperature of both samples are shown in Table 3.2. The plot of the specific heat capacity (C_p) versus temperature (T) and the fitting curve for the sample with the aluminum substrate are shown in Figure 3.5.

Table 3.2 Specific Heat Capacity of A123Systems Li-ion's Positive Electrode

$LiFePO_4$ coating material with aluminum substrate				$LiFePO_4$ coating material without aluminum substrate			
Onset melting temperature of 193 °C				Onset melting temperature of 180 °C			
T (°C)	C_p (J/°C/g)	T (°C)	C_p (J/°C/g)	T (°C)	C_p (J/°C/g)	T (°C)	C_p (J/°C/g)
25	0.2248	300	2.0857	25	0.4956	300	0.0982
50	1.2782	325	2.1960	50	1.1189	325	0.9177
75	1.3954	350	2.2750	75	2.0403	350	1.8145
100	1.5237	375	2.2995	100	3.0239	375	2.8843
125	1.6114	400	2.3644	125	3.3459	400	2.1099
150	2.1429	425	2.4018	150	4.4053	425	1.6019
175	1.9216	450	2.4203	175	4.9449	450	1.3952
200	2.6652	475	2.5083	200	6.3694	475	2.5620
225	2.1413	500	2.5537	225	4.1274	500	3.0414
250	2.1465	525	2.4923	250	2.7976	525	2.1485
275	2.1111	547	2.4319	275	1.2961	547	0.0000

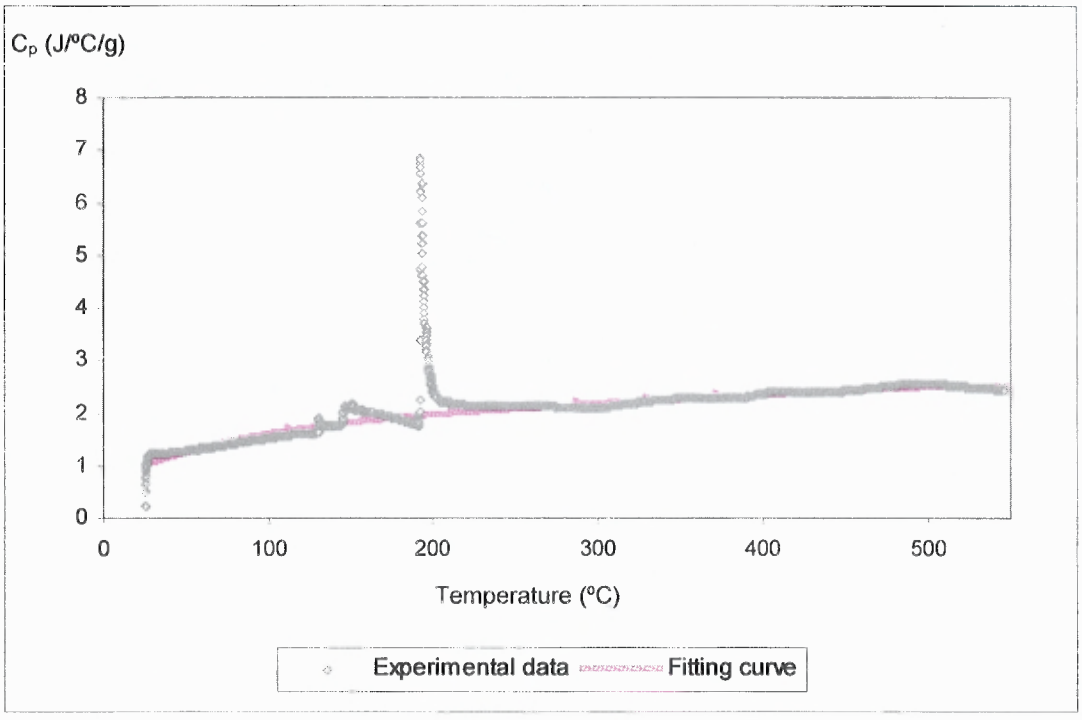

Figure 3.5 Specific heat capacity of A123Systems Li-ion's positive electrode.

Note: The A123Systems' positive electrode is made of Al Substrate coated with nanostructured $LiFePO_4$. The equation of the fitting curve obtained by least-square method with an R^2 value of 0.96 is

$$C_p = 0.8969 + 0.00842T - 0.00002T^2 + 1.53E^{-8}T^3$$

The small variation of the heat capacity may be explained by the weight loss of the $LiFePO_4$ observed by TGA through the entire temperature range used for the DSC. This may be due to the degradation or loss of volatiles such as water. It must be noted that the specific heat capacity at above the point of thermal transition can be affected by the weight loss.

Due to the unavailability of data on the specific heat capacity of aluminum coated with microscopic $LiFePO_4$, the specific heat capacity of the sample with the aluminum substrate (aluminum substrate coated with nanostructured $LiFePO_4$) is compared with the value of iron-phosphate-based material ($NaFePO_4$) and pure microstructured aluminum and iron as shown in Figure 3.6.

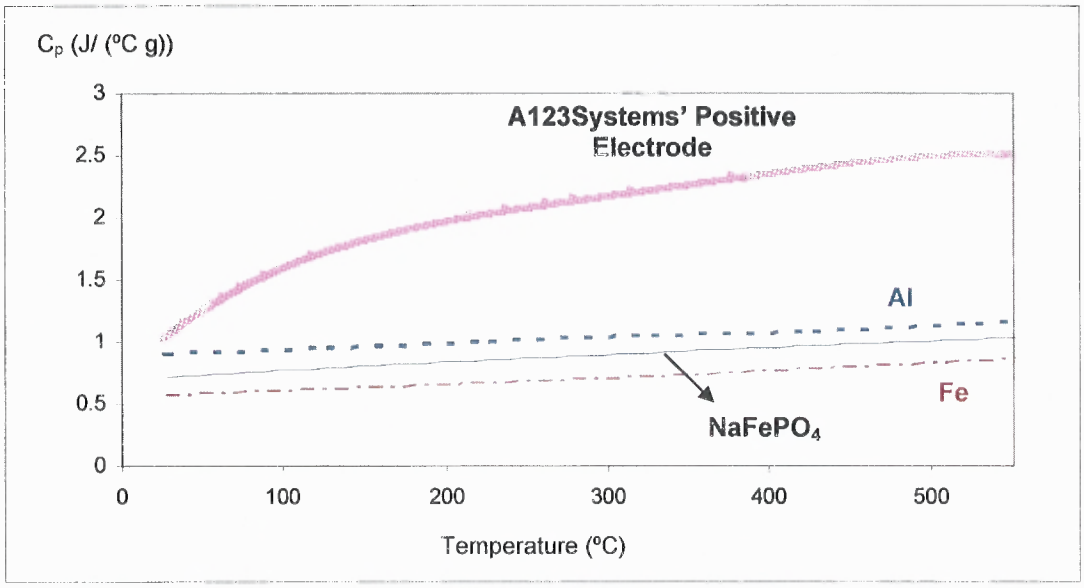

Figure 3.6 Specific heat capacity of A123Systems Li-ion's positive electrode, $NaFePO_4$, aluminum, and iron.

Note: The specific heat capacity of aluminum and iron can be expressed as

For $NaFePO_4$, $C_p = 0.6948 + 7.3258E^{-4}T - 2.0857E^{-7}T^2$

For aluminum, $C_p = 0.8964 + 0.0004T + 2.2179E^{-7}T^2$

For iron, $C_p = 0.5529 + 3.8015E^{-4}T + 2.9218E^{-7}T^2$

Source of specific heat capacity data: $NaFePO_4$ [Tremaine and Xiao, 1999], Al [Hatch, J.E., 1984], and Fe [NIST Chemistry Webbook]

3.4 Discussion

The experimental results reveal that the cathode of A123Systems 26650A cell is coated with a thin film of agglomerates of lithium iron phosphate nanoparticles. According to the SEM images, carbon fibers with a diameter of tens to hundreds nanometers are uniformly distributed throughout the surface topography of the cathode.

Upon exposure, carbon fibers could cause a similar toxic effect to that of asbestos and CNTs due to the similarity of their structures. Moreover, iron-based nanomaterials such as iron oxide (Fe_2O_3) nanoparticles have recently been found to cause toxic effect to nerve cells [Pisanic et al., 2007]. Lithium iron phosphate ($LiFePO_4$) nanoparticles could produce a similar toxic effect.

Thin film is one type of nanomaterial structure that exhibits superheating phenomenon. The melting point of iron-based materials is also high. Additional research is needed to determine the reduction and melting temperatures of nanostructured metal oxides and phosphates. If the reduction temperature of nanostructured metal oxides exceeds the operating temperature of the reduction process, then metal oxides will enter the smelting process without being converted into metallic form, which may affect the process. Eventually, nanostructured metal oxides whose melting point is higher than the smelting temperature may leave the process and serve as contaminants in the recovered metals and slag.

For those nanostructured metals with reduction temperatures higher than the operating temperature, it is unknown whether or not the nanostructured metal oxides will retain their structure throughout the HTMR. Additionally, metal oxides usually decompose upon heating and supply oxygen to the reduction process. However, A123Systems has claimed that their nanophosphate cathode exhibits no oxygen release upon heating [A123Systems]. Without adequate external oxygen supply, the reduction process may be disrupted as it must be operated in an oxygen-rich environment.

DSC results show that the specific heat capacity of the positive electrode is higher than the value of pure aluminum and iron-phosphate-based material ($NaFePO_4$). This excess heat capacity is attributed to the presence of nanostructured $LiFePO_4$ coating material on the electrode and the bonding/interface between the substrate and coating material . According to the laws of thermodynamics, it requires a higher amount of ***heat*** energy to ***raise*** the ***temperature of*** materials with higher specific heat capacity. As a result, it is anticipated that the excess heat capacity or specific heat capacity enhancement caused by nanomaterials will contribute to higher energy consumption by HTMR process.

CHAPTER 4

ENVIRONMENTAL AND PROCESS IMPACTS FROM PHYSICAL PROPERTIES OF NANOMATERIALS

Toxicity studies relevant to the exposure to airborne nanoparticles have indicated that inhaled nanoparticles can be toxic to human lung cell. Nanoparticles could penetrate into the deepest parts of human lungs and cause inflammatory effect. The result of these studies has raised concern about the potential release of airborne nanoparticles from nanoproduct production process as well as the recycling process where the product containing nanoparticles is decomposed into small pieces before entering the high-temperature processes.

Filtration is the most widely used control technique to limit occupational exposure to fine particles. During the past few years, the adequacy of the current filtration technology for capturing nanoparticles has been widely investigated. Existing studies examine the penetration of nanoparticles through various types of filter such as fibrous filter [Huang et al., 2007; Steffens and Coury, 2007[a]] and high efficiency particulate arrester (HEPA) filter [Steffens and Coury, 2007[b]]. According to these studies, due to the brownian motion of nanoparticles, there is a correlation between the filtration efficiency and particle size.

Research also shows that the shape of nanoparticles can significantly affect the filtration efficiency at low capture velocity where the motion of nanoparticles in contact with the filter and the area of contact between the filter media and nanoparticles are shape dependent [Boskovic et al., 2005, 2008]. From the study results, at capture velocity as

low as 5 cm/s (or 10 fpm), the filtration efficiency for spherical nanoparticles is significantly higher than that of non-spherical nanoparticles and the difference in the efficiency becomes larger with increasing particle size. It is worth mentioning that the typical capture velocity of industrial-used baghouse filter is 200 to 550 fpm [BPS]. Other secondary parameters which may affect the filtration efficiency include temperature, humidity, and particle charge.

4.1 Filtration of Nanoparticles

In the case of fine particles with diameters between 0.1 μm and 2.5 μm, the filtration efficiency decreases as the particle size decreases. However, for finer nanoparticles with diameters less than 0.1 μm (100 nm), the opposite occurs: filtration efficiency tends to increase as the size of nanoparticles decreases. The increase in efficiency is due to the random motion of nanoparticles in a gas medium, often referred to as Brownian motion. While traveling through air, nanoparticles repeatedly collide with air molecules resulting in the continuous change in their motion direction, eventually becoming random. The random motion increases the probability of contact between nanoparticles and the filter media, leading to higher filtration efficiency [Kim et al., 2007]. This phenomena only occurs when the particle mass is sufficiently low so that the particle can be deflected by the air molecules. However, the nanoparticle filtration study by Kim and et al., found an exception to this behavior for very fine nanoparticles [Kim et al., 2006[a]]. The filtration efficiency for nanoparticles with an average diameter of a few nanometers decreases with decreasing particle size. At the nanoscale, particles normally adhere to the filter elements by a weak-bond force, such as the Van Der Waal force. And, for very small particles, the

Brownian motion causes particles to move at very high velocity and fail to be captured by weak-bond forces, resulting in lower filtration efficiency.

The adequacy of fibrous filter commonly used in HTMR recycling process such as a baghouse filter for capturing nanoparticles is evaluated and discussed below. As shown in Figure 4.1, the filter efficiency curve of fibrous filter developed by Kim and et al [Kim et al., 2006 [a]] is used to simulate particle collection.

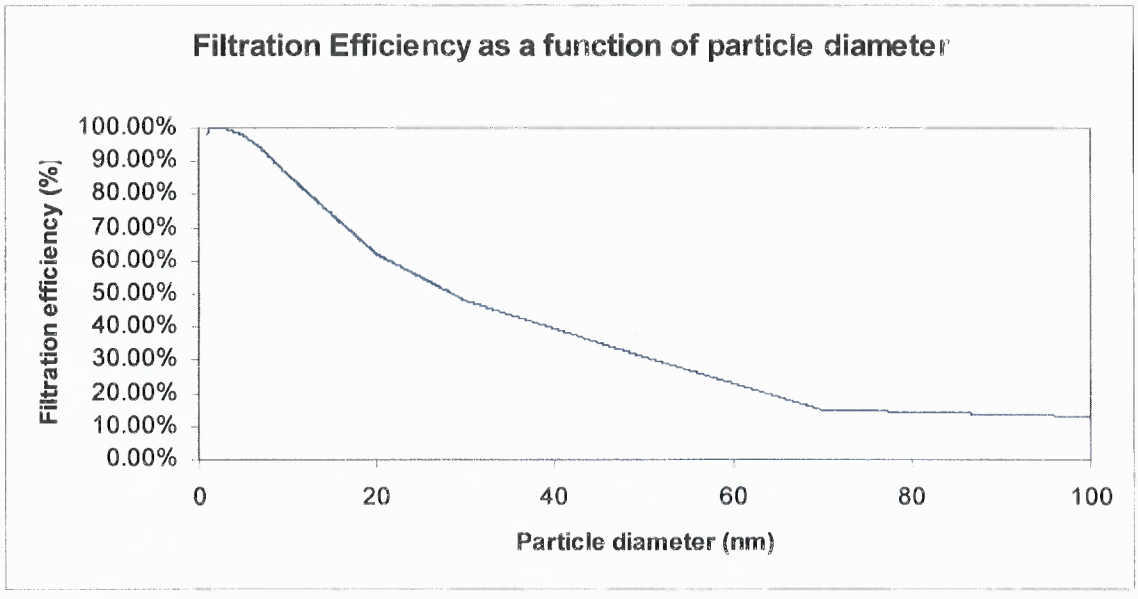

Figure 4.1 Filtration efficiency as a function of particle diameter.
Source: [Kim et al., 2006 [a]]

4.2 Environmental and Process Impacts from Nanomaterial Filtration

Most of nanomaterials being used as electrode materials by Li-ion batteries manufacturers and research groups are currently in the size of a few tens nanometers in diameter. Emerging trends in Li-ion technology have resulted in the increasing utilization of nanomaterials whose size is of the order of a few nanometers as electrode materials

[Wang et al., 2006]. The use of smaller anode materials helps reduce the volume expansion problem during charge and discharge process and hence improves the cycling stability of the battery. Meanwhile, the use of smaller cathode materials can reduce the lithium diffusion length resulting in shorter charging time [Panero et al., 2004].

At the EOL stage, the generation of smaller nanoparticles can be expected from the recycling process. The comminuting process by the use of shredder or hammer mill could result in shorter nanotubes and smaller nanoparticles. Recent studies reveal that CNTs can be mechanically cut by various physical techniques which include abrasion, grinding, ball milling, electrical cutting, gamma irradiation, chopping and sonication [Nanosprint, 2006]. Alternatively, CNTs can also be cut by the use of sonication technique in the presence of an oxidizing acid [Liu et al., 1998; Ziegler et al., 2005]. Sonication creates side-wall damage to CNTs and the subsequent attack at the point of damage by acid soon cuts the tubes completely. Shorter tubes can be obtained by increasing the reaction time.

A simulation model with three scenarios is developed to identify the size distribution of penetrated particles. The size of incoming particles is assumed to be normally distributed with a mean of 10, 40, and 70 nanometers and a standard deviation of 5, 8, and 10, respectively. In each scenario, the sample size of incoming particles is 500 particles. For each size interval, the number of penetrated particles is calculated by multiplying the number of incoming particles by the probability of penetration obtained directly from the filtration efficiency shown in Figure 4.1. According to the simulation results shown in Figure 4.2, for particle sizes of less than 100 nm, large-sized particles have a greater chance of penetrating the filter and becoming airborne particles as

compared to smaller-sized particles. In addition, approximately 80% of the 70-nm nanoparticles cannot be captured by the fibrous filter media.

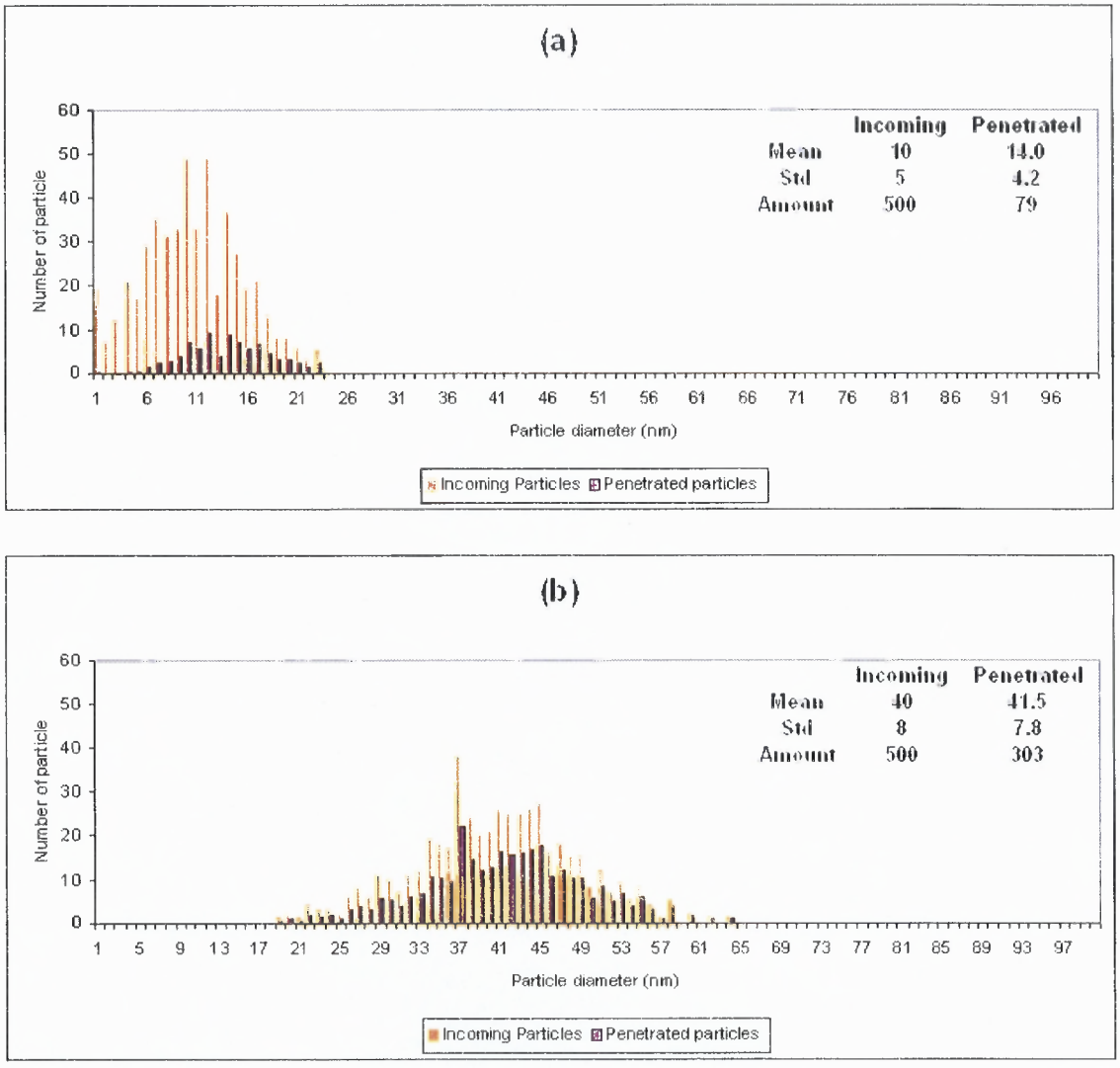

Figure 4.2 Size distribution of incoming and penetrated particles.

(a) Scenario 1 – Incoming particles normally distributed with a mean of 10 and a standard deviation of 5 nanometers, (b) Scenario 2 – Incoming particles normally distributed with a mean of 40 and a standard deviation of 8 nanometers, and (c) Scenario 3 – Incoming particles normally distributed with a mean of 70 and a standard deviation of 10

Source: [Olapiriyakul et al., 2009]

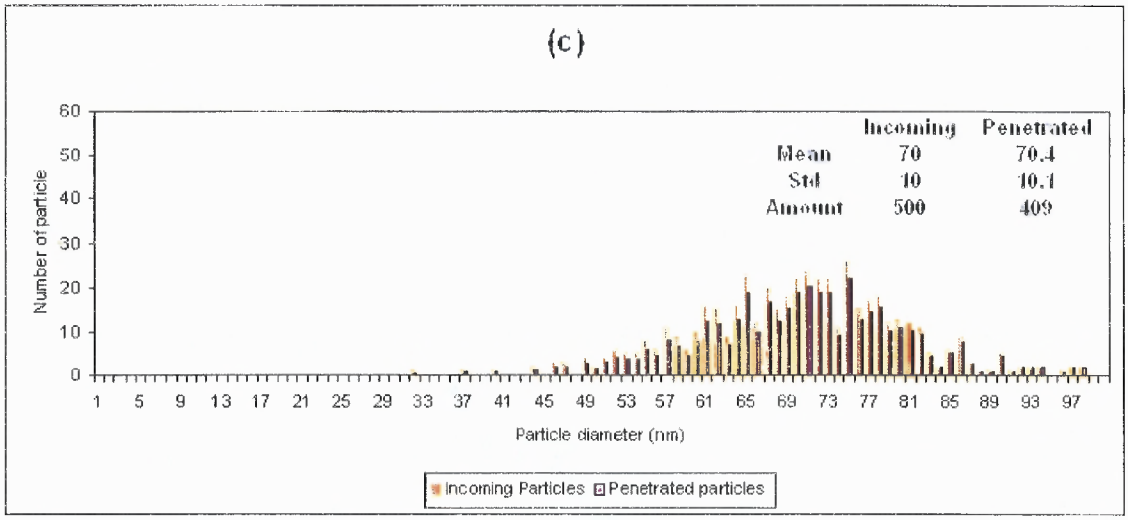

Figure 4.2 Size distribution of incoming and penetrated particles. (Continued)

(a) Scenario 1 – Incoming particles normally distributed with a mean of 10 and a standard deviation of 5 nanometers, (b) Scenario 2 – Incoming particles normally distributed with a mean of 40 and a standard deviation of 8 nanometers, and (c) Scenario 3 – Incoming particles normally distributed with a mean of 70 and a standard deviation of 10

Source: [Olapiriyakul et al., 2009]

CHAPTER 5

ENVIRONMENTAL AND PROCESS IMPACTS FROM THERMODYNAMIC PROPERTIES OF NANOMATERIALS

The study here focuses on the impacts of nanomaterials during the HTMR recycling process caused by their thermodynamic properties including melting point elevation (or superheating) and specific heat capacity enhancement (or excess heat capacity). High-temperature processing of superheated nanomaterials with unusually high melting point will result in a higher smelting temperature, higher energy consumption, and increased air emissions, including the possibility of nanomaterials escaping through the process filtration system. At the same time, the reduction process may require additional heat energy to raise the temperature of the furnace due to the specific heat enhancement of nanomaterials. Previous research at Ohio State University has shown that exergy analysis is a valuable tool in analyzing product and process environmental impacts when specific lifecycle data is unavailable [Bakshi and Ukidwe, 2006]. The ability of a process/product to create environmental impacts is quantified by means of evaluating the exergy loss or exergetic efficiency associated with the process/product. In this dissertation, thermodynamic analysis with a focus on energy and exergy is used to evaluate the potential environmental impacts in the absence of specific toxicity data.

5.1 Thermodynamic Analysis of HTMR Recycling Process

In this section of the dissertation, background information on thermodynamic analysis, consisting of both energy and exergy analyses, is presented. After that, a thermodynamic analysis is performed to examine the energy and exergy flows and losses of the HTMR process with the existing operating condition. The information such as material flow rate, operating temperature, and operating time of furnaces are obtained from publically available data on the Inmetco process. Inmetco operates an HTMR facility providing thermal recovery for numerous battery types including nickel cadmium, nickel-metal hydride, and Li-ion.

5.1.1 Background of Thermodynamic Analysis

The details of the thermodynamic analysis, including assumptions and formulas, are presented in this section. Energy analysis, based on the first law of thermodynamics, has long been used to identify potential energy improvements for a variety of processes. As shown below in Equation 5.1, the useful energy output, *Useful* E_{output}, is equal to the difference between the energy input, E_{input}, and energy loss, E_{loss}, which is the energy of unusable materials.

$$Useful\ E_{output} = E_{input} - E_{loss} \tag{5.1}$$

Assuming that all processes are adiabatic and constant in pressure and volume, the change in internal energy, ΔE, is equal to the change in enthalpy, ΔH, as represented in Equation 5.2. Under the same process assumptions, the change in enthalpy of material

flows is equal to the amount of heat absorbed during the process, which can be calculated by using Equation 5.3.

$$\Delta E = \Delta H \tag{5.2}$$

$$\Delta H = mC_p \Delta T \tag{5.3}$$

Measuring only the input and output energy, energy analysis frequently leads to an incomplete or misleading conclusion regarding process performance due the inability to account for the loss of useful energy, or the quality of energy, due to irreversibility of an actual process [Kissock et al., 2001]. Most importantly, energy analysis only examines the heat content of material flows without considering their chemical potential.

While the total energy remains constant, according to the second law of thermodynamics, any real process proceeds in such a direction that useful energy or exergy undergoes degradation through energy conversion mechanisms such as friction, electrical resistance, and chemical reactions. Based on the first and second law of thermodynamics, exergy is defined by Szargut, *et al* as the maximum amount of work obtainable when an energy carrier is brought from its initial state to a state of thermodynamic equilibrium [Szargut et al., 1988]. The term exergy is synonymous with available energy and availability, as based on the free energy concept developed by J. Willard Gibbs in 1873 [Gaggioli et al., 2002]. However, for a Gibbs free energy analysis, the pressure and temperature of a surrounding medium are held constant.

In the HTMR recycling process, the amount of exergy in the system decreases when transforming electrical energy into heat energy. Likewise, the chemical reactions during the reduction and smelting processes also result in significant loss of exergy due to the irreversibility of the reaction. These irreversible losses within the system boundary must be examined as they will eventually dissipate into the surroundings and potentially create negative environmental impacts.

Exergy analysis has been recognized by researchers and LCA practitioners as an approach that is more informative and meaningful than energy analysis alone due to its ability to measure losses associated with thermodynamic irreversibility of a process [Bakshi and Ukidwe, 2006; Ao et al., 2008]. According to these studies, process performance characteristics, such as exergy loss (consumption) and exergetic efficiency, have been used as indicators for environmental impact of emissions. Exergy output, Ex_{output}, is equal to the difference between the exergy input, Ex_{input}, and the total exergy loss, Ex_{loss}, which is the summation of the exergy of unusable materials, $Ex_{unusable}$, and the exergy loss due to process irreversibility, $Ex_{irr\ loss}$, as shown in Equations 5.4 and 5.5.

$$Ex_{output} = Ex_{input} - Ex_{loss} \tag{5.4}$$

$$Ex_{loss} = Ex_{unusable} + Ex_{irr\ loss} \tag{5.5}$$

The exergy analysis presented here focuses on thermal and chemical components, which are the primary conversion forces of the HTMR recycling process. Other forms of exergy such as potential, mechanical, kinetic, and nuclear are neglected in this study. Thermal exergy of material i, $Ex_{th,i}$, can be obtained by calculating the difference between

the change in enthalpy, ΔH, and entropy, ΔS, as shown in Equation 5.6, where the ambient temperature, T_0, is equal to about 300 K.

$$Ex_{th,i} = \Delta H - T_0(\Delta S) \tag{5.6}$$

For simplification, the specific heat capacity, C_p, of materials at the reference temperature is assumed to be the same as that of the material at the process temperature, $C_{p,i}$. As a result, thermal exergy of material i, $Ex_{th,i}$, can be expressed as shown in Equation 5.7.

$$Ex_{th,i} = C_p(T_i - T_0) - C_p T_0 \ln\frac{T_i}{T_0} \tag{5.7}$$

As depicted in Equation 5.8, the chemical exergy of material i, $Ex_{ch,i}$, is the product of the material's standard chemical exergy, e_i, and mass flow rate, $\dot{m}_i$.

$$Ex_{ch,i} = e_i \dot{m}_i \tag{5.8}$$

The calculation of chemical exergy is based on the reduction of iron oxide and manganese oxide, which are the primary materials contained in the battery wastes processed by the HTMR recycling process. By assuming the exergy conversion efficiency to be 33% and carbon dioxide as the only gaseous output produced by the chemical reaction, the chemical exergy balance equations can be written as shown in

Equations 5.9 and 5.10 [Baumgartner, 2006]. The reducing agent, carbon, is transformed into carbon dioxide during the reduction and smelting operations. It must be noted that the exergy conversion efficiency varies according to many factors such as the reaction temperature and composition of materials. However, for this study, an exergy conversion efficiency of 33% is assumed throughout the HTMR process and for all temperature ranges.

$$2\,Fe_2O_3 + 12.42\,C + 9.42\,O_2 \rightarrow 4\,Fe + 12.42\,CO_2 \tag{5.9}$$

$$2\,MnO + 4.2\,C + 6.4\,O_2 \rightarrow 2\,Mn + 4.2\,CO_2 \tag{5.10}$$

5.1.2 Energy Analysis Results

The energy losses shown in Table 5.1 for the reduction and smelting processes are calculated by using Equation 5.1 for a cycle time of 60 minutes. The energy or heat content of materials flows is calculated by using Equation 5.3. The details of energy flows of the studied system are shown in appendix A and B. For the reduction process, the only energy input is the electrical energy consumed by the RHF during the 60 minute cycle time. The heat content of input material flows, including green pellet and iron shot, is equal to zero as the material is stored at ambient temperature. The output energy flows are the heat content of sponge iron, waste gases, and carbon dioxide. At the smelting process, the total input energy is the summation of the heat content of the sponge iron and the electrical energy consumed by the EAF during the 60 minute cycle time. The total output energy is equal to the heat content of the molten metal, slag, scrubber filter cake, baghouse dust, and carbon dioxide.

Table 5.1 Energy Analysis Results of the HTMR Recycling Process For a Cycle Time of 60 Minutes

Reduction Process

Input		Output	
Electric Power	38.5 GJ	Sponge Iron	22.6 GJ
		Waste Gases	2.2 GJ
		Carbon Dioxide	12.7 GJ
E_{input}	38.5 GJ	Useful E_{output}*	22.6 GJ
		Useful E_{output}**	30.1 GJ
	E_{loss}*	15.9 GJ	
	E_{loss}**	8.4 GJ	

Smelting Process

Input		Output	
Electric Power	67.0 GJ	Molten Metal	27.5 GJ
Sponge Iron	22.6 GJ	Slag	12.4 GJ
		Waste Gases	2.5 GJ
		Carbon Dioxide	2.0 GJ
E_{input}	89.6 GJ	Useful E_{output}*	27.5 GJ
		Useful E_{output}**	29.7 GJ
	E_{loss}*	62.1 GJ	
	E_{loss}**	59.9 GJ	

* Assuming sponge iron and molten metal as the only useful output for the reduction and smelting process, respectively.

** Assuming that 50% of the heat content of carbon dioxide and waste gases can be recovered, which is within the typical range of heat recovery values reported [U.S. department of energy, 2005].

The results of the energy analysis show that the smelting process contributes to the major energy loss in the HTMR recycling process. At the same time, carbon dioxide emission is the primary source of energy loss at the reduction process.

5.1.3 Exergy Analysis Results

In Table 5.2, the exergy loss, Ex_{loss}, is calculated by using Equation 5.5. Exergy of the input-output material flows is the summation of thermal and chemical exergy. Thermal exergy can be calculated by using Equation 5.7. At the reduction process, assuming that the temperature of incoming material, which is green pellet and iron shot, is equal to the ambient temperature, the thermal exergy is equal to zero. The details of exergy flows of the studied system are shown in appendix A and B.

The chemical exergy of the material flows at the reduction and smelting processes is calculated directly from the standard chemical exergy value and the mass flow rate of each material as shown in Table 5.3. The amount of released carbon dioxide is estimated by using the exergy-balanced chemical reaction Equations 5.9 and 5.10.

Table 5.2 Exergy Analysis Results of the HTMR Recycling Process For a Cycle Time of 60 Minutes

Reduction Process

Input					Output				
Materials		Mass (kg)	Ex_{ch} (GJ)	Ex_{th} (GJ)	Materials		Mass (kg)	Ex_{ch} (GJ)	Ex_{th} (GJ)
Green Pellet and Iron Shot	Fe	9,100	61.2	-	Sponge Iron	Fe	20,700	139.1	13.7
	Fe_2O_3	22,000	2.3			Mn	150	1.1	
	MnO	500	0.8			Fe_2O_3	2,300	0.2	
	C	10,800	369.3			MnO	300	0.5	
	Others	750	-			C	2,100	71.8	
Oxygen		18,600	2.3			Others	80	-	
Electric Power		38.5 GJ			Waste Gases		3,000	6.7	1.3
					CO_2		33,500	15.2	32.9
Ex_{input} 474.4 GJ					Useful Ex_{output}* 226.4 GJ Ex_{loss}* 248.0 GJ Useful Ex_{output}** 243.5 GJ Ex_{loss}** 230.9 GJ				

Smelting Process

Input					Output				
Materials		Mass (kg)	Ex_{ch} (GJ)	Ex_{th} (GJ)	Materials		Mass (kg)	Ex_{ch} (GJ)	Ex_{th} (GJ)
Sponge Iron	Fe	20,700	139.1	13.7	Molten Metal	Fe	22,100	148.5	18.2
	Mn	150	1.1			Mn	320	2.4	
	Fe_2O_3	2,300	0.2			C	740	25.3	
	MnO	300	0.5			Others	-	-	
	C	2,100	71.8		Slag	Fe_2O_3	200	0.02	8.2
	Others	80	-		Waste Gases		2,300	1.5	1.7
Oxygen		2,000	0.3	-	CO_2		3,900	1.8	5.9
Electric Power		67.0 GJ							
Ex_{input} 293.7 GJ					Useful Ex_{output}* 194.4 GJ Ex_{loss}* 99.3 GJ Useful Ex_{output}** 198.2 GJ Ex_{loss}** 95.5 GJ				

* Assuming sponge iron and molten metal as the only useful output for the reduction and smelting process, respectively.

** Assuming that 50% of the heat content of carbon dioxide and waste gases can be recovered, which is within the typical range of heat recovery values reported [U.S. department of energy, 2005].

Table 5.3 Chemical Exergy of Material Flows in the HTMR Recycling Process

Material		Molecular Weight (g/mole)	Std Exergy (kJ/mole)	Reduction		Smelting	
				Mass (Kg)*	Exergy (MJ)	Mass (Kg)**	Exergy (MJ)
Input	Fe_2O_3	160	16.5	4664	480	2096	220
	MnO	87	135.5	57	90	300	470
	C	12	410.3	2189	74840	1063	36350
	O_2	32	4.0	4461	560	2327	290
Output	Fe	56	376.4	3265	21940	1467	9860
	Mn	55	410.2	36	270	189	1420
	CO_2	44	19.9	8026	3630	3898	1760

* reaction amount per one cycle time of 20 minutes

** reaction amount per one cycle time of 60 minutes

As shown in Table 5.2, the exergy loss associated with the reduction and smelting processes, operating without waste heat recovery, are 248 GJ and 99.3 GJ, respectively. As opposed to the energy analysis results presented above, the exergy analysis reveals that the reduction process is the primary source of process loss. For both the reduction and smelting processes, large amounts of exergy loss occurs due to the irreversibility of the chemical reactions, as shown in Figures 5.1 and 5.2.

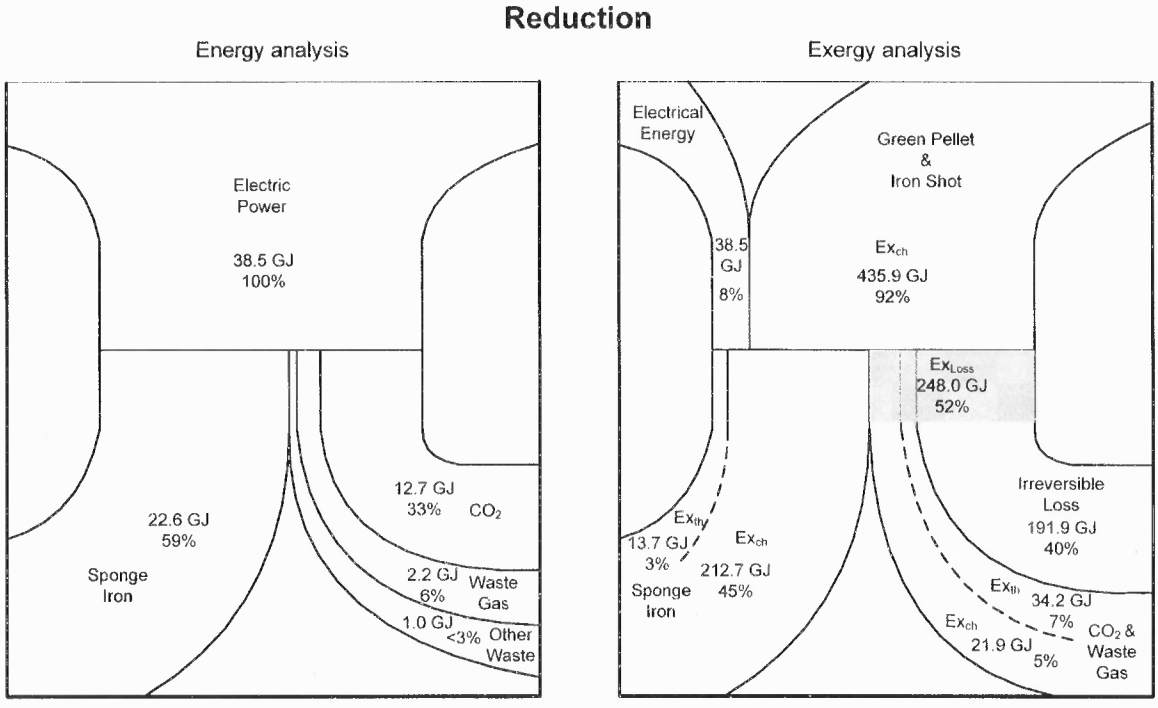

Figure 5.1 Energy and exergy flow pattern for the reduction process for a cycle time of 60 min.

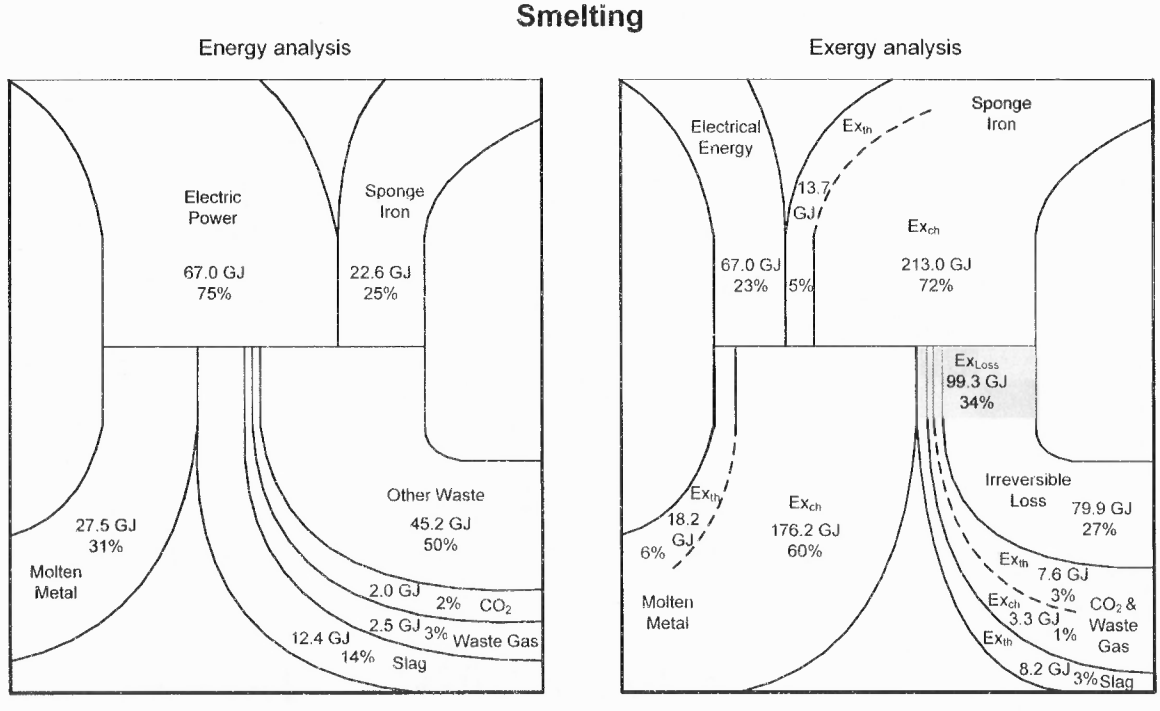

Figure 5.2 Energy and exergy flow pattern for the smelting process for a cycle time of 60 min.

5.2 Impacts of Higher Smelting Temperature on Exergy Loss

The energy consumption and environmental impact of nanomaterial-containing Li-ion batteries during the EOL lifecycle stage are explored using the HTMR process as the case study. During recycling, nanomaterials embedded in Li-ion batteries may exhibit superheating, retain their nanostructure throughout the recycling process, and contaminate the recovered metals and slag. To overcome the problem, the operating temperature for the smelting process will need to be increased resulting in increased energy consumption and higher levels of carbon dioxide emissions.

The impact of higher smelting temperatures, anticipated for superheated nanomaterials, is analyzed by examining the electrical power consumption, molten metal thermal exergy, and exergy loss corresponding to various smelting temperature levels as shown in Table 5.4. According to the energy consumption data of typical EAF operations by Camdali and Tunc [Camdali and Tunc, 2002], the relationship between electrical energy consumption and smelting temperature is essentially linear for the temperature range under study.

Table 5.4 Effects of Higher Smelting Temperature for a Cycle Time of 60 Minutes

Change (%)	Smelting Temperature (°C)	Electric Power (GJ)	Ex_{th} of Molten Metal (GJ)	Ex_{loss} (GJ)
0%	1700	67.0	18.2	99.3
+20%	2040	80.4	23.8	107.1
+50%	2550	100.5	32.4	118.6

Note: assume that the increases in the smelting temperature (+20% and +50%) are needed for the full meltdown of nanomaterials.

As shown in Figure 5.3, at a smelting temperature of 2550 °C, the exergy loss during the smelting process increases by about 20 GJ or about 6 % of the entire process loss over the 60 minute cycle time.

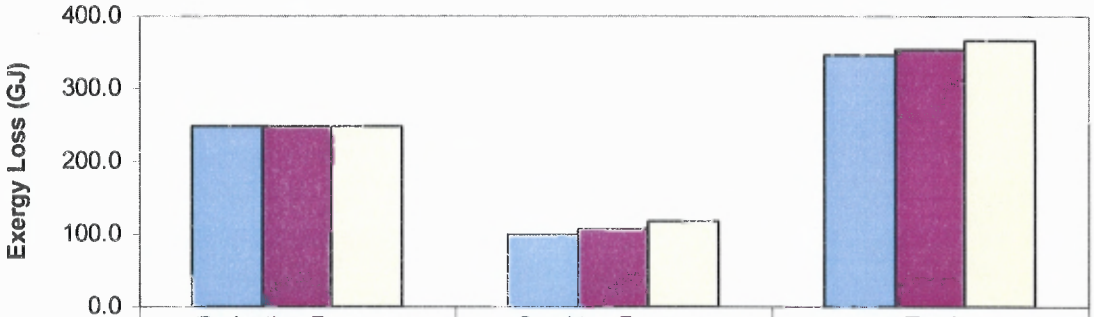

	Reduction Process	Smelting Process	Total
100%	248.0	99.3	347.3
120%	248.0	107.1	355.1
150%	248.0	118.6	366.6

Figure 5.3 Exergy loss as a function of smelting temperature.
Note: 120% and 150% are smelting temperatures for nanomaterials

The energy analysis, which considers only the heat content of material flows, identifies the smelting process as the primary source for process loss. However, in the case of HTMR recycling process, the result of the energy analysis is incomplete and potentially misleading as the process is partly driven by chemical reactions. It can be observed that the energy loss, which is the energy of unusable materials, of the reduction process is extremely low. This result reflects the limitation of the energy analysis by not considering the chemical exergy of the carbon reducing agent and other processed materials, which accounts for 92% of the total input exergy at the reduction process according to the exergy analysis.

The exergy analysis provides deeper insights into the environmental impact of the process due to the ability to identify the source and magnitude of the exergy loss. The exergy losses shown in Figures 5.2 and 5.3 can be categorized into irreversible losses, unrecoverable heat content, and chemical potential of the waste gas and slag. These losses produce an increase in entropy of the surrounding environment potentially creating disorder and causing ecological damage. In addition, the exergy-balanced reaction equations can be used to estimate the amount of carbon dioxide released from the chemical reactions. As opposed to the energy analysis result, the exergy analysis shows that the chemical reactions that occur during the reduction and smelting processes are the primary sources of exergy loss and carbon dioxide emissions, while the actual electricity consumption of the process has a lesser impact. At the same time, large amounts of exergy are dissipated through the conversion of electricity to heat at the smelting process. At the current operating condition, almost 30 % of the overall exergy loss originates from the smelting process. If the smelting temperature is increased by 50 % to fully process the nanomaterials, under assumptions of constant heat flux, the smelter may operate for a longer period of time resulting in an additional 20 GJ of exergy loss.

5.3 Impacts of Heat Capacity Enhancement of Nanomaterials

Specific heat capacity enhancement of nanomateirals is another thermodynamic property that may contribute to the increased energy consumption of HTMR process. As aforementioned in Chapter 2, specific heat capacity of nanomaterials is generally higher than the bulk value, called specific heat capacity enhancement. The degree of specific heat capacity enhancement depends on the physical characteristics of nanomaterials such as size, shape, and structure.

Specific heat capacity is the amount of heat energy required to raise the temperature of one unit mass of the substance by one unit of temperature. The increase in specific heat capacity of nanomaterials, which are being used as electrode materials of Li-ion batteries, will result in higher energy consumption during the HTMR process where the temperature of nanomaterials-containing recyclate is increased as needed to reach the reduction and smelting temperatures.

In this section of the dissertation, experimental data from several previous studies on the specific heat capacity of nanomaterials is combined with the specific heat capacity measurements performed in this dissertation on a sample of the positive electrode material from the A123systems battery. This datasets are analyzed to study the impacts of nanomaterials physical characteristics on the heat capacity enhancement of nanomaterials. By using regression analysis and the specific heat capacity equation, the impacts of three physical characteristics—size, structure, and host matrix—are analyzed in terms of the energy consumption required to raise the temperature of materials and average percentage enhancement of specific heat capacity.

5.3.1 Size of Nanoparticle

For nanocrystalline or nanoparticle materials, size defined as the diameter of particle is the key parameter affecting the specific heat capacity of nanomaterial, as demonstrated by the following examples.

Example 1: Nanocrystalline Titanium Dioxide (TiO_2)

According to the previous study by Wu [Wu, 2001], the increase in specific heat capacity at nanoscale has been observed in nanocrystalline TiO_2, a similar material to lithium titanate used by Li-ion battery manufacturers such as Enerdal [Enerdel] and Altair Nanotechnology [Altairnano] as the anode material. The specific heat capacity of coarse-grained (bulk) TiO_2 and nanocrystalline TiO_2 with various diameters; 14, 15, and 75 nm, was measured by an automated adiabatic calorimeter in the temperature range 78-370 K. Only the experimental data on the specific heat capacity of nanocrystalline TiO_2 in the temperature range of between 300 K (ambient temperature) to 370 K are shown in Table 5.5. According to the experimental data, specific heat capacity of nanocrystalline TiO_2 is size-dependent at nanoscale and increases with decreasing particle size.

Table 5.5 Specific Heat Capacity of 14, 15, and 75-nm Nanocrystalline TiO_2

14-nm TiO_2		15-nm TiO_2		75-nm TiO_2	
Temperature (K)	C_p (J/(mol K))	Temperature (K)	C_p (J/(mol K))	Temperature (K)	C_p (J/(mol K))
301	74.68	299	71.94	297	55.57
306	75.68	304	72.93	302	56.37
310	76.58	309	73.77	306	56.90
314	77.78	313	75.49	311	57.48
318	78.47	318	76.29	316	58.30
322	79.75	322	77.24	320	59.13
327	80.54	327	78.39	325	59.52
331	81.35	331	79.46	330	60.17
335	82.51	336	80.43	334	60.77
339	83.61	340	81.74	339	61.29
343	84.52	345	82.92	343	62.09
347	85.62	349	83.66	348	62.85
351	86.67	354	84.64	352	63.68
355	87.87	358	85.58	356	64.35
359	88.84	362	86.32	361	64.90
364	90.02	366	87.26	365	65.37
368	91.12	371	88.54	369	66.12

Source: [Wu, 2001]

The specific heat capacity (C_p) of nanocrystalline TiO_2 and coarse-grained (bulk) TiO_2 is expressed as a function of temperature (T) as shown in Equations 5.11-5.14 [Wu, 2001]. These equations are valid over the temperature range 78-370 K.

For 14-nm nanocrystalline TiO_2,

$$C_{p\ 14\text{-}nm\ TiO_2} = 57.314 + 32.904x - 4.5667x^2 + 5.9816x^3 - 0.37166x^4 \tag{5.11}$$

$$\text{where } x = \frac{(T - 223.46)}{144.45}$$

For 15-nm nanocrystalline TiO_2,

$$C_{p\ 15\text{-}nm\ TiO_2} = 57.412 + 29.603x - 3.2015x^2 + 6.4598x^3 - 1.6607x^4 \tag{5.12}$$

$$\text{where } x = \frac{(T - 225.41)}{145.23}$$

For 75-nm nanocrystalline TiO_2,

$$C_{p\ 75\text{-}nm\ TiO_2} = 45.949 + 22.229x - 8.5445x^2 + 4.9229x^3 + 1.8171x^4 \tag{5.13}$$

$$\text{where } x = \frac{(T - 223.89)}{144.91}$$

For bulk TiO_2,

$$C_{p\ bulk\ TiO_2} = 37.338 + 24.579x - 8.929x^2 + 0.34322x^3 + 2.0624X^4 \tag{5.14}$$

$$\text{where } x = \frac{(T - 175.33)}{122.83}$$

Equations 5.11-5.14 are integrated with respect to temperature to calculate the change in enthalpy. The energy consumption for raising the temperature of nanostructured and bulk TiO_2 from 300 K (ambient temperature) to 370 K is shown in Table 5.6.

Table 5.6 Energy Consumption for Raising the Temperature of 14-nm, 15-nm, and 75-nm Nanocrystalline TiO_2 and Bulk TiO_2

Material	Energy (KJ/Kg)
14-nm TiO_2	72.55
15-nm TiO_2	70.36
75-nm TiO_2	53.46
Bulk TiO_2	53.65

Note: The energy is consumed over the temperature range 300-370 K .

To further explore the size effect on the specific heat capacity of nanocrystalline TiO_2, multiple regression analysis is employed in this dissertation to model the specific heat capacity (C_p) of nanocrystalline TiO_2 as a function of temperature (T) and particle size (S) as shown in Equation 5.15.

$$C_p(S,T) = 16.6867 - 0.3397S + 0.2083T \tag{5.15}$$

The squared correlation coefficient, R^2, of the above fitting equations is equal to 0.986. The regression line and experimental data are plotted as shown in Figure 5.4. The energy requirement for raising the temperature of nanocrystalline TiO_2 from t_o (ambient temperature of 300 K) to t_2 (370 K), can be estimated by calculating the change in the enthalpy which is equal to the integral of the Equation 5.15 with respect to temperature.

$$\Delta H_{t_2-t_o} = \int_{t_o}^{t_2} \left(C_p(S,T)\right) dT$$

$$\Delta H_{370-298} = \left(16.6867\,T - 0.3397\,S\,T + 0.1042\,T^2\right)\Big|_{300}^{370}$$

$$\Delta H_{370-298} = 6213.05 - 24.4584\,S$$

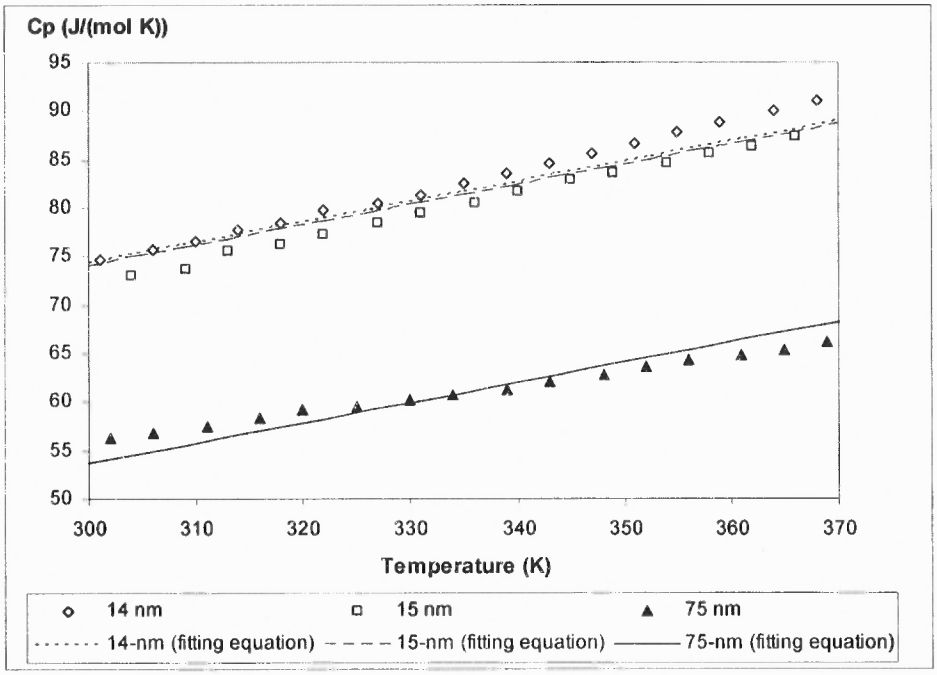

Figure 5.4 Experimental data on the specific heat capacity of nanocrystalline TiO_2 with fitting curves.

Note: The fitting curves are constructed based on Equation 5.15.

The energy requirement for raising the temperature of nanocrystalline TiO_2 with different size is shown in Table 5.7.

Table 5.7 Energy Consumption for Raising the Temperature of Nanocrystalline TiO_2

Size (nm)	Energy (KJ/Kg)
15	73.20
25	70.14
35	67.07
45	64.01
55	60.95
65	57.89
75	54.83

Note: The energy is consumed over the temperature range 300-370 K . The molecular weight of nanocrystalline TiO_2 equals to the bulk value which is 79.87 g/mol.

Example 2: Nanocrystalline Nickel

Electrode material made of nanostructured nickel [Boyanov et al., 2008] and other transition metals embedded in a phosphorous matrix have been recently developed to improve electrochemical mechanism and related performance characteristics of Li-ion batteries. Additionally, nanostructured nickel has long been used as a catalyst in the production of carbon nanotubes which are widely used in electronic applications and recently as an electrode material for Li-ion batteries.

Research [Wang, 2002] shows that the specific heat capacity of nanocrystalline nickel is slightly higher than that of the corresponding bulk material over the temperature range 78-370 K as shown in Figure 5.5. The equations of specific heat capacity as a function of temperature are shown in Equations 5.16 and 5.17. The specific heat capacity of bulk nickel is shown in Equation 5.18.

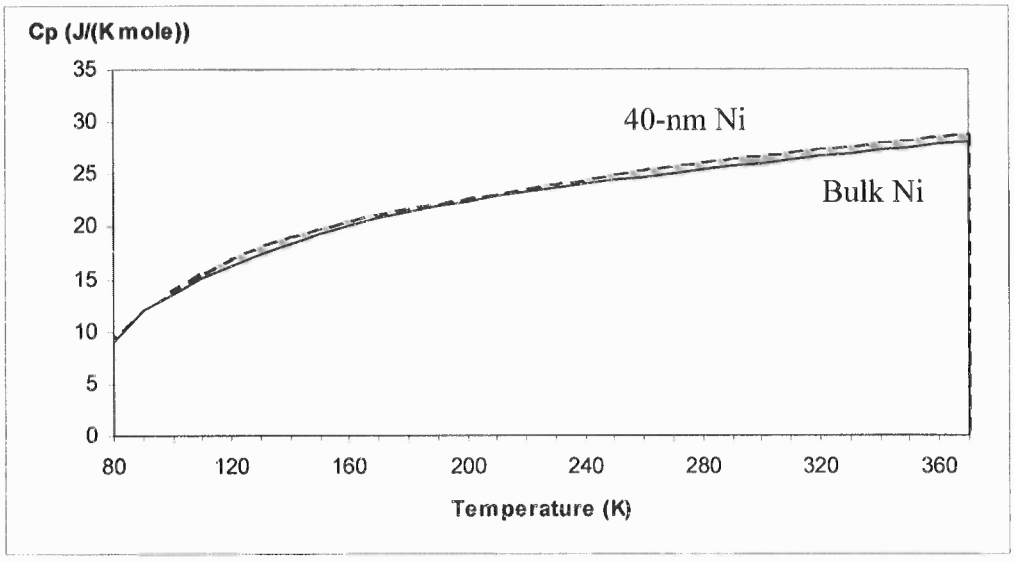

Figure 5.5 Specific heat capacity of 40-nm Ni and bulk Ni.

Source: The specific heat capacity values of nanocrystalline nickel are obtained from [Wang, 2002]. The specific heat capacity values of bulk nickel in the temperature range 80-300 K are obtained from [Busey and Giauque, 1952]. At above 300 K, the specific heat capacity values of bulk nickel is estimated by using polynomial least-squares fitting method.

For 40-nm nanocrystalline nickel,

$$C_{p\ 75\text{-}nm\ TiO_2} = 45.949 + 22.229x - 8.5445x^2 + 4.9229x^3 + 1.8171x^4 \tag{5.16}$$

where $x = \dfrac{(T - 223.89)}{144.91}$

For the ease of calculation, Equation 5.16 is simplified as

$$C_{p\ 40\text{-}nm\ Ni}(T) = -4.7891E^{-5}T^2 + 0.0617T + 12.6668 \tag{5.17}$$

For bulk nickel,

$$C_{p\ Bulk\ Ni}(T) = -3.9869E^{-5}T^2 + 0.0559T + 12.9204 \tag{5.18}$$

Source: Equation 5.16 [Wang, 2002] and Equation 5.18 [Busey and Giauque, 1952]

The heat energy consumption for raising the temperature of 40-nm Ni and bulk Ni from t_o (ambient temperature of 300 K) to t_2 (370 K), is estimated by calculating the change in the enthalpy which is equal to the integral of Equations 5.16-5.18, as shown below and in Table 5.8.

For 40-nm nanocrystalline nickel,

$$\Delta H_{t_2-t_o} = \int_{t_o}^{t_2} \left(C_{p\ \ 40-nm\ Ni}(T)\right) dT$$

$$\Delta H_{370-300} = \int_{300}^{370} \left(-4.7891E^{-5}T^2 + 0.0617T + 12.6668\right) dT$$

$$\Delta H_{370-300} = \left(-0.000016T^3 + 0.03085T^2 + 12.6668T\right)\Big|_{300}^{370}$$

$$\Delta H_{370-300} = 2.01\ KJ\ mole^{-1} \text{ or } 0.0342\ KJ/Kg$$

For bulk nickel,

$$\Delta H_{t_2-t_o} = \int_{t_o}^{t_2} \left(C_{p\ \ Bulk\ Ni}(T)\right) dT$$

$$\Delta H_{370-300} = \int_{300}^{370} \left(-3.9869E^{-5}T^2 + 0.0559T + 12.9204\right) dT$$

$$\Delta H_{370-300} = \left(-0.000013T^3 + 0.02795T^2 - 12.9204T\right)\Big|_{300}^{370}$$

$$\Delta H_{370-300} = 1.95\ KJ\ mole^{-1} \text{ or } 0.0333\ KJ/Kg$$

Table 5.8 Energy Consumption for Raising the temperature of Nanocrystalline Ni

Material	Energy (KJ/Kg)
40-nm Ni	0.0342
Bulk Ni	0.0333

Note: The energy is consumed over the temperature range 300-370 K

5.3.2 Structure of Nanomaterials

Research [Lu et al., 1991; Sun and Lu, 1996] shows that atomic structure is another factor affecting the specific heat capacity of nanomaterials. The description of nanostructure studied is shown in Table 5.9. In general, without structural change during the heating process, specific heat capacity of nanocrystalline materials is higher than that of the corresponding amorphous and coarse-grained polycrystalline (material composed of aggregates of nanocrystallines) counterpart [Lu et al 1991].

Table 5.9 Nanomaterials Structure

Structure	Description
Nanocrystalline	A polycrystal in which the size of the crystallites are in the range of 1 to 50 nm
Coarse-grained polycrystalline	Material composed of aggregates of nanocrystal
Amorphous	Material with low degree of crystal lattice structure

The experimental data of the specific heat capacity of nickel-phosphorous (Ni-P) alloy with three different structures: nanocrystalline, amorphous, and coarse-grained polycrystalline, over the temperature range 310-400 K, are shown in Figure 5.6. The average size of nanocrystalline and amorphous Ni-P alloy is substantial lower than 100 nm while the size of coarse-grained polycrystalline Ni-P alloy is about 100 nm.

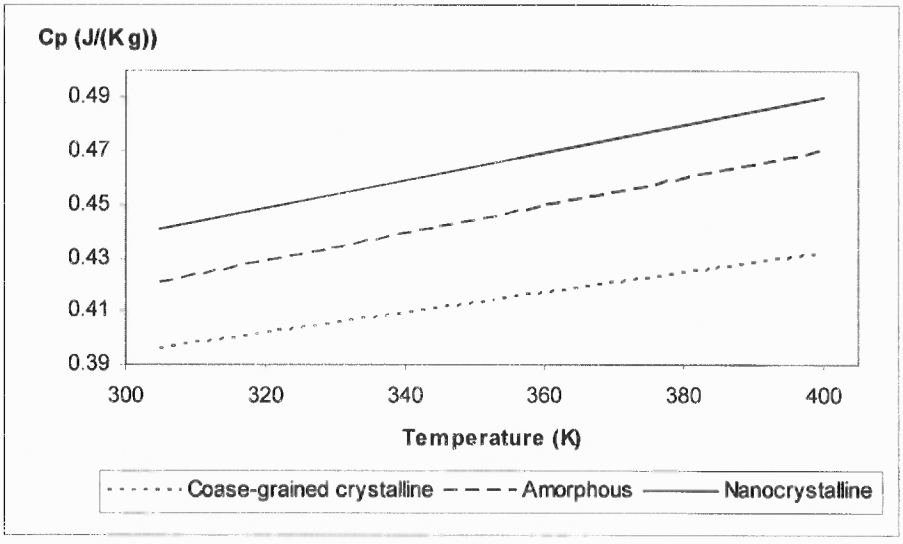

Figure 5.6 Specific heat capacity of Ni-P alloy with different structures.
Source: [Lu et al., 1991]

In order to evaluate the energy impact, the experimental data on specific heat capacity of Ni-P alloy obtained from the literature are expressed as a function of temperature (T) by using regression analysis. The fitting curves for nanocrystalline, amorphous, and coarse-grained crystalline Ni-P alloy are shown in Equations 5.20 – 5.22.

For nanocrystalline Ni-P alloy,

$$C_p(T) = 5.1579E^{-4}T + 0.2837 \tag{5.20}$$

For amorphous Ni-P alloy,

$$C_p(T) = 5.1579E^{-4}T + 0.2637 \tag{5.21}$$

For coarse-grained crystalline Ni-P alloy,

$$C_p(T) = 3.7895E^{-4}T + 0.2804 \tag{5.22}$$

The heat energy required to raise the temperature of Ni-P alloy with different structures from t_o (ambient temperature of 300 K) to t_2 (400 K), can be estimated by calculating the change in the enthalpy which is equal to the integral of the Equations 5.20-5.22 with respect to temperature as shown below. The estimated energy requirement is shown in Table 5.10.

For nanocrystalline Ni-P alloy,

$$\Delta H_{t_2-t_o} = \int_{t_o}^{t_2} \left(C_{p\ nanocrystalline}(T)\right) dT$$

$$\Delta H_{400-300} = \left(0.000258T^2 + 0.2837T\right)\Big|_{300}^{400}$$

$$\Delta H_{400-300} = 46.42 \quad KJ/Kg$$

For amorphous Ni-P alloy,

$$\Delta H_{t_2-t_o} = \int_{t_o}^{t_2} \left(C_{p\ amorphous}(T)\right) dT$$

$$\Delta H_{400-300} = \left(0.000258T^2 + 0.2637T\right)\Big|_{300}^{400}$$

$$\Delta H_{400-300} = 44.42 \quad KJ/Kg$$

For coarse-grained Ni-P alloy,

$$\Delta H_{t_2-t_o} = \int_{t_o}^{t_2} \left(C_{p\ \ amorphous}(T)\right) dT$$

$$\Delta H_{400-300} = \left(0.000189T^2 + 0.2804T\right)\Big|_{300}^{400}$$

$$\Delta H_{400-300} = 41.31 \quad KJ/Kg$$

Table 5.10 Energy Consumption for Raising the Temperature of Ni-P Alloy

Structure	Energy (KJ/Kg)
Nanocrystalline	46.42
Amorphous	44.42
Coarse-grained crystal	41.31

Note: The energy is consumed over the temperature range 300-400 K

5.3.3 Host Matrix

In this dissertation, the host matrix is classified into free-standing nanoparticles, supported nanoparticles (nanoparticles deposited on a substrate), and nanocomposites. The specific heat capacity enhancement of free-standing nanoparticles is investigated in the previous sections of the chapter. In this section, the factors affecting the degree of specific heat capacity enhancement in supported nanoparticles and nanocomposites are investigated. After that, the degree of specific heat capacity enhancement in free-standing nanoparticles, supported nanoparticles, and nanocomposite are compared.

Example 1: CNTs-Reinforced Aluminum Oxide (Al_2O_3) Nanocomposite

Research [Kumari et al., 2008] shows that the specific heat capacity of nanocomposites is higher than the bulk value, and, the degree of the enhancement is primarily dependent on the content of nanomaterials homogenously distributed within the matrix. The experimental data from the literature, as shown in Table 5.11 and Figure 5.7, indicate that the specific heat capacity of CNTs-reinforced aluminum oxide (CNT-Al_2O_3) nanocomposite increases with increasing CNTs content.

Table 5.11 Specific Heat Capacity of CNTs-Al_2O_3 Nanocomposites (J/(g K))

Temperature (°C)	CNTs Content (wt%)		
	0%	7.39%	19.10%
60	0.84	1.42	3.31
100	0.90	1.73	3.73
150	0.97	1.93	4.05
200	1.02	2.08	4.33
250	1.06	2.20	4.68
300	1.09	2.35	5.20
350	1.12	2.23	5.63
400	1.14	1.96	6.09

Note: The nanocomposite is sintered at 1450 °C during the synthesis process.

Source: [Kumari et al 2008]

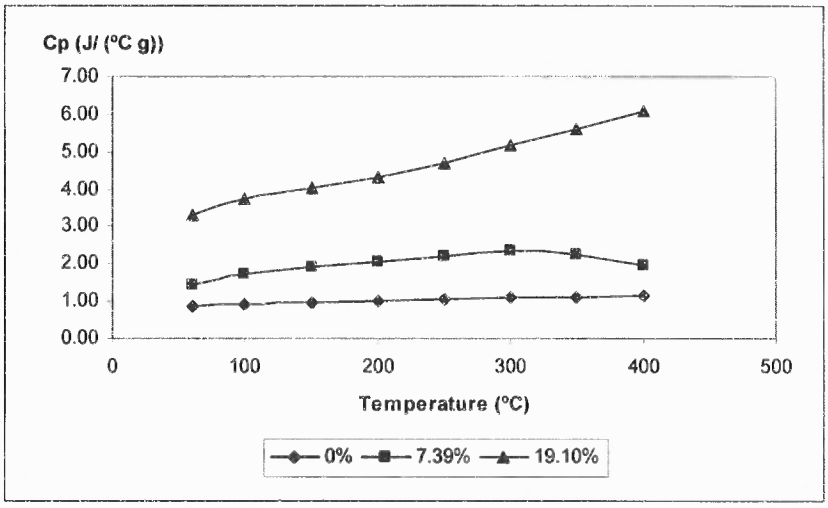

Figure 5.7 Specific heat capacity of CNTs-Al_2O_3 nanocomposites.
Source: [Kumari et al 2008]

In order to study the impacts of CNTs content on the specific heat capacity of the nanocomposites, multiple regression analysis is utilized to express the specific heat capacity as a function of CNTs content (C) and temperature (T) as shown in Equation 5.19.

$$C_p(C,T) = -2.591 + 1.498 \log T + 0.193\, C \tag{5.19}$$

Then, the heat energy required to raise the temperature of CNTs-Al_2O_3 nanocomposites with different CNTs content from t_o (ambient temperature of 300 K) to t_2 (673 K), can be estimated by calculating the change in the enthalpy which is equal to the integral of the Equation 5.19 with respect to temperature. The estimated values for the energy requirement are shown in Table 5.12.

$$\Delta H_{t_2-t_o} = \int_{t_o}^{t_2} \left(C_p(C,T)\right) dT$$

$$\Delta H_{673-300} = \left(0.651\,T\left(\ln(T)\right) + 0.297\left(C - 16.771\right)\right)\Big|_{300}^{673}$$

$$\Delta H_{673-300} = 72.375\,C + 530.985$$

Table 5.12 Energy Consumption for Raising the Temperature of CNTs-Al_2O_3 Nanocomposites

CNTs content (%wt)	Energy (KJ/Kg)
0%	531
2%	676
4%	821
6%	966
8%	1111
10%	1256
12%	1401
14%	1546
16%	1691
18%	1836
20%	1980

Note: The energy is consumed over the temperature range 25-400 °C

Example 2: A123Systems Li-ion battery positive electrode made of aluminum substrate coated with nanostructured $LiFePO_4$

The host matrix of the positive electrode material can be classified as supported nanoparticles. The DSC result presented in Chapter 3 indicates that the specific heat capacity of the position electrode made of aluminum substrate coated with nanostructured $LiFePO_4$ is higher that the value of bulk iron-phosphate-based material (sodium iron phosphate ($NaFePO_4$)) and macroscopic pure aluminum and iron as shown in Figure 5.8.

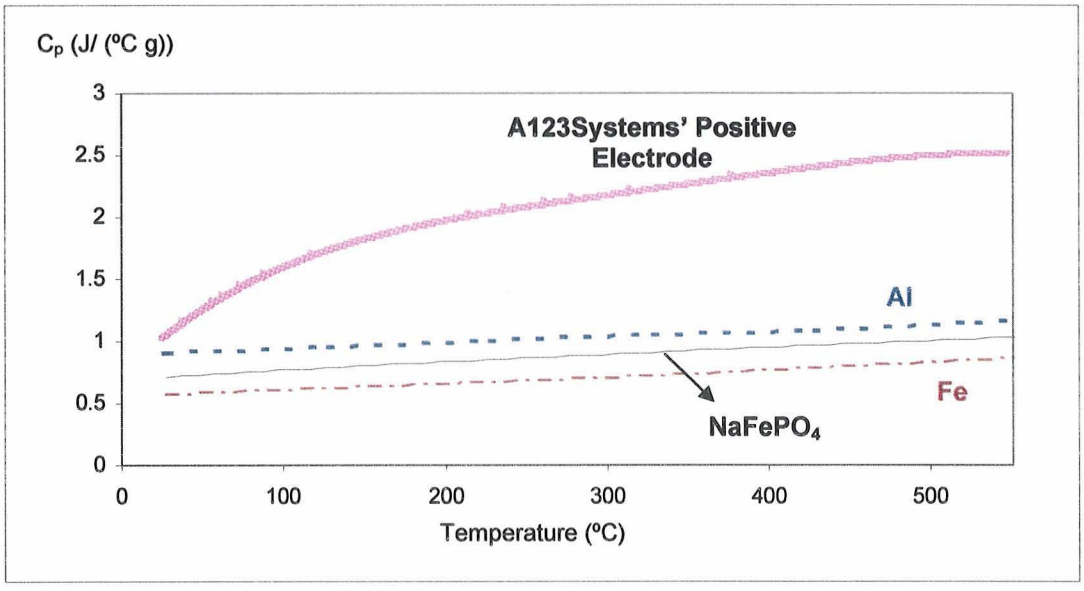

Figure 5.8 Specific heat capacity of A123Systems Li-ion's positive electrode, $NaFePO_4$, aluminum, and iron.

Note: The A123Systems' positive electrode is made of Al Substrate with coated with nanostructured $LiFePO_4$.

By using regression analysis, the specific heat capacity of the positive electrode material, $NaFePO_4$, macroscopic aluminum, and macroscopic iron can be expressed as a function of temperature (T) as shown in Equations 5.20 – 5.23, respectively.

For the positive electrode material,

$$C_p = 0.8969 + 0.00842T - 0.00002T^2 + 1.53E^{-8}T^3 \tag{5.20}$$

For sodium iron phosphate,

$$C_p = 0.6948 + 7.3258E^{-4}T - 2.0857E^{-7}T^2 \tag{5.21}$$

For aluminum,

$$C_p = 0.8964 + 0.0004T + 2.2179E^{-7}T^2 \tag{5.22}$$

For iron,

$$C_p = 0.5529 + 3.8015E^{-4}T + 2.9218E^{-7}T^2 \tag{5.23}$$

The heat energy required to raise the temperature of the positive electrode material, $NaFePO_4$, and the macroscopic materials from t_o (ambient temperature of 25 °C) to t_2 (550 °C), can be estimated by calculating the change in the enthalpy which is equal to the integral of the Equations 5.20-5.23 with respect to temperature. The estimated values for the energy requirement are shown in Table 5.13.

For the positive electrode material,

$$\Delta H_{t_2 - t_o} = \int_{t_o}^{t_2} \left(C_{p\ \text{Positive electrode}}(T) \right) dT$$

$$\Delta H_{550-25} = \left(3.825E^{-9}T^4 - 0.000007T^3 + 0.00421T^2 + 0.8969T \right)\Big|_{25}^{550}$$

$$\Delta H_{550-25} = 980\ KJ/Kg$$

For $NaFePO_4$,

$$\Delta H_{t_2-t_o} = \int_{t_o}^{t_2} \left(C_{p\ NaFePO_4}(T)\right) dT$$

$$\Delta H_{550-25} = \left(-6.9523E^{-8}T^3 + 0.0004T^2 + 0.6948T\right)\Big|_{25}^{550}$$

$$\Delta H_{550-25} = 460\ KJ/Kg$$

For aluminum,

$$\Delta H_{t_2-t_o} = \int_{t_o}^{t_2} \left(C_{p\ Al}(T)\right) dT$$

$$\Delta H_{550-25} = \left(7.393E^{-8}T^3 + 0.0002T^2 + 0.8964T\right)\Big|_{25}^{550}$$

$$\Delta H_{550-25} = 540\ KJ/Kg$$

For iron,

$$\Delta H_{t_2-t_o} = \int_{t_o}^{t_2} \left(C_{p\ Fe}(T)\right) dT$$

$$\Delta H_{550-25} = \left(9.7393E^{-8}T^3 + 0.0002T^2 + 0.5529T\right)\Big|_{25}^{550}$$

$$\Delta H_{550-25} = 360\ KJ/Kg$$

Table 5.13 Energy Consumption for Raising the Temperature of A123System's Positive Electrode, $NaFePO_4$, Aluminum, and Iron

Material	Energy (KJ/Kg)
A123System's positive electrode material	980
$NaFePO_4$	460
Aluminum	540
Iron	360

Note: The energy is consumed over the temperature range 25-550 °C

In summary, the specific heat capacity of nanomaterials is generally higher than the bulk value and the degree of specific heat capacity enhancement is dependent primarily on the physical characteristics of nanomaterials, irrespective of chemical composition. Higher degree of specific heat capacity enhancement is observed in nanocomposite and nanoparticles grown on top of a substrate (supported nanoparticles). As shown in Table 5.14, it requires a substantially higher amount of heat energy to raise the temperature of nanomaterials compared to their bulk counterparts. Compared to macroscopic $NaFePO_4$, aluminum and iron, at least 80% more heat energy is required to raise the temperature of A123System's positive electrode material from the ambient temperature to 550 °C.

Table 5.14 The Effect of the Physical Characteristics on the Degree of Heat Capacity Enhancement

Physical Characteristic	Comparison		Additional Energy Consumption	Temperature Range
	Bulk Material	Nanomaterial		
Size	bulk TiO_2	14-nm nanocrystalline TiO_2	35%	300-370K
	bulk Ni	40-nm nanocrystalline Ni	3%	300-370K
Structure	100-nm polycrystalline Ni-P alloy	nanocrystalline Ni-P alloy	12%	310-400K
	100-nm polycrystalline Ni-P alloy	amorphous Ni-P alloy	8%	310-400K
Host matrix	pure Al_2O_3	CNTs-reinforced Al_2O_3 nanocomposite (20% CNTs by weight)	270%	300-673K
	$NaFePO_4$, Al, and Fe	Al substrate coated with nanostructured $LiFePO_4$	> 80%	300-820K

Note: The amount of additional energy consumption is equivalent to the average specific heat capacity enhancement percentage over the studied temperature range.

5.4 LCA Analysis of HTMR Recycling Process

LCA is a process to evaluate the environmental burdens associated with a product by identifying and quantifying energy and material usage and environmental releases, to assess these impacts, and to evaluate and implement environmental improvements [SETAC]. LCA is a comprehensive approach which considers impacts across all stages of the product lifecycle from material extraction and synthesis to production, distribution, use and end of life management.

In this dissertation, LCA is performed to study the environmental impact of a higher operating temperature required by smelting process to ensure the full meltdown of Li-ion battery waste containing nanomaterials is analyzed in term of carbon dioxide emissions to air by using LCA software, Gabi 4.2. As shown in Figure 5.9, the boundary of the studied system consists of shredding, reduction, and smelting processes. The Gabi process plan contains data regarding the energy consumption and material flows during a 60-minute operating cycle.

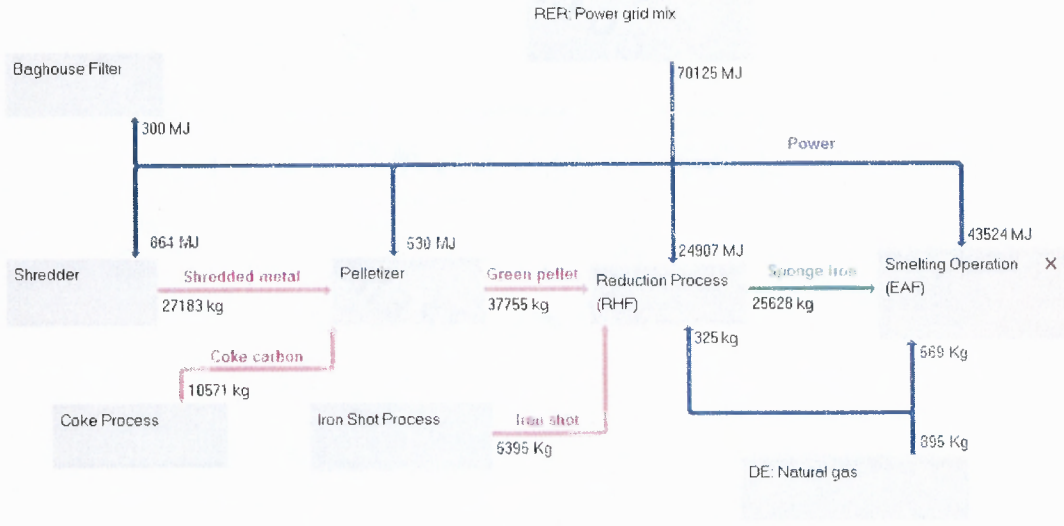

Figure 5.9 Gabi process plan for HTMR recycling process.

The environmental impact of the HTMR recycling system is calculated based on the amount of electricity and natural gas consumed by the system and the quantity of CO_2 generated directly from the chemical reactions at the reduction and smelting processes. The following describes the energy consumption values assumed for each process in the system:

- The hammer mill used for the shredding process is assumed to consume about 8.83 kwh per ton of shredded metal [Kawatra, S. K. and Ripke, S.J., 2002].
- Four disc pelletizers are used to prepare the battery waste in the form of green pellets. Each pelletizer consumes approximately 37 kwh, with a maximum capacity of 10 ton/hr [Henan Hongji Mine Machinery Co., Ltd.].
- Typically, HTMR processes use baghouse filters to remove particles and other contaminants from the air handling system. Each of these filters consumes between 690 and 854 kwh [Reddy, C.S., 2007].
- The rotary hearth furnace (RHF) at the reduction process consumes about 350 kwh per ton of sponge iron [Bauer et al. 1990].
- The smelting process is based on an electric arc furnace (EAF) which consumes between 360 to 400 kwh per ton of molten metals [Jeremy, J., 1997].
- The source of power consumption in the reduction and smelting process is assumed to be 65 percent electrical energy and 35 percent natural gas.

The amount of carbon dioxide emitted from the chemical reaction at the reduction and smelting processes into the atmosphere is calculated by using exergy-balanced chemical reaction, Equations 5.9 and 5.10, with 33% exergy conversion efficiency. Toxicity of nanomaterials and emissions associated with the supply chain of material flows are not included in the current analysis.

The amount of impact the process has on global warming is examined at three different smelting temperature levels; 100%, 120%, and 150% (1973K, 2368K, and 2960K). At the existing operating condition (100%), carbon dioxide emitted from the chemical reaction at the reduction and smelting processes represents the largest contribution to global warming potential in the process. As the required smelting temperature is higher, the smelter operates for a longer period of time resulting in a higher level of power consumption and carbon dioxide emissions due to the chemical reaction of the remaining carbon and metal oxides in the slag. As depicted in Gabi result shown in Figure 5.10, the total amount of carbon dioxide emissions increases by 2038 and 5094 kg as the smelting temperature increases by 20% and 50%, respectively, as needed to fully melt down nanomaterials. The carbon dioxide produced by chemical reaction is assumed to be released into the atmosphere.

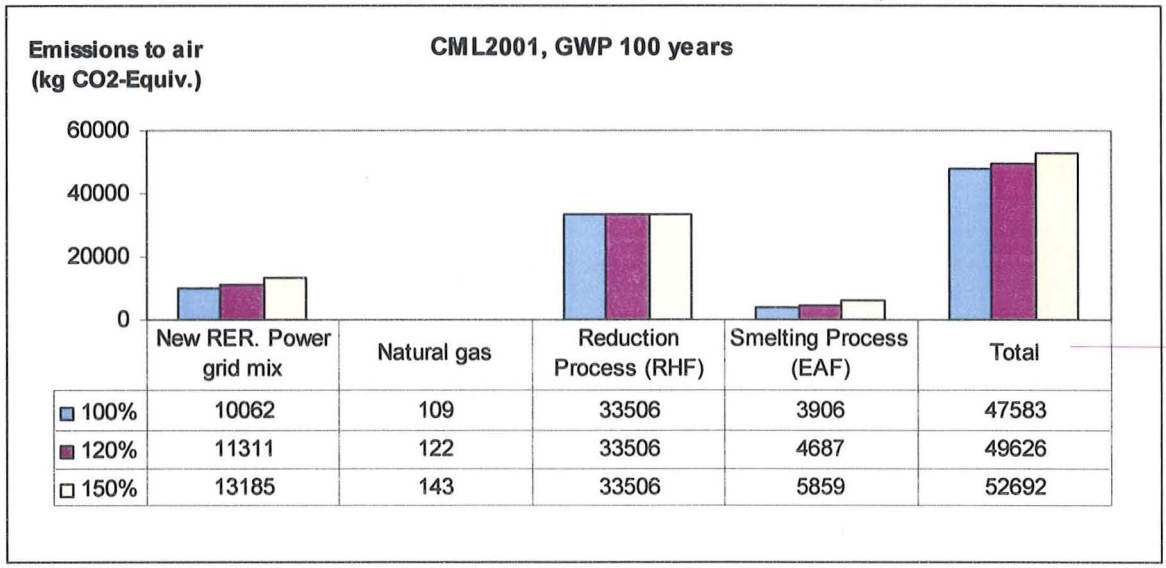

	New RER. Power grid mix	Natural gas	Reduction Process (RHF)	Smelting Process (EAF)	Total
100%	10062	109	33506	3906	47583
120%	11311	122	33506	4687	49626
150%	13185	143	33506	5859	52692

Figure 5.10 Emissions to air at various smelting temperature levels.

Note: 120% and 150% are the levels of higher smelting temperatures needed to fully process the nanomaterials.

5.5 Discussion

The environmental impacts of nanomaterials during the EOL stage due to their unusual thermodynamics properties are explored using high temperature battery recycling process as a case study. During recycling, nanomaterials embedded in Li-ion batteries may exhibit superheating, retain their nanostructure throughout the recycling process, and become contaminants in the recovered metals and slag. To overcome the problem, the operating temperature for the smelting process will need to be increased resulting in a longer operating time, increased energy consumption, and higher level of carbon dioxide emissions. At the same time, the specific heat capacity enhancement of nanomateirals within Li-ion batteries may result in a larger amount of energy consumption by HTMR recycling process for raising the temperature of the battery recyclate to the reduction temperature and their melting point.

Energy and exergy analysis are used in the present study to assess the environmental impact by examining the energy consumption and the thermal and chemical components of material flows. At the same time, LCA is used to estimate the global warming impact of the recycling process. The average increase in energy consumption over the studied temperature range caused by specific heat capacity enhancement is also evaluated by using regression analysis and specific heat equation.

The results of exergy analysis and LCA suggest that recycling of nanoproducts could result in a high level of thermal and chemical exergy consumption and emissions of global warming gases. In addition, previous exergy and LCA studies have shown that the production of nanomaterials and nanoproducts is an energy demanding process.

Energy analysis, focusing only on the heat content of material flows, identifies smelting process as the primary source for process loss. However, in the case of HTMR recycling process, the result of energy analysis is incomplete and potentially misleading as the process is partly driven by chemical reactions. It can be observed that the energy efficiency of the reduction process is excessively high due to neglecting the chemical exergy of carbon reducing agent which accounts for 88% of the total input exergy according to exergy analysis.

As opposed to energy analysis result, reduction process is identified as the primary source of process loss and carbon dioxide emissions by exergy analysis and LCA results, respectively. The results of exergy analysis also provide more insight into the environmental impact due to its ability in identifying the source and magnitude of the exergy loss. According to the exergy analysis results, while chemical reaction is the primary source of exergy loss at the reduction process, large amounts of exergy are

dissipated through the conversion of electricity to heat at the smelting process. In comparison, the exergy loss of reduction process is twice the amount of exergy loss of smelting process.

Additional exergy loss of about 19,300 MJ or 7% of the system's exergy loss can be expected during each 60-minute operating cycle when the smelting temperature is increased by 50 percent. Under existing operating conditions, about 8 percent of all greenhouse gas emissions originate from the smelting process. When the smelting temperature is increased 50 percent as needed to melt the nanomaterials, the smelter must operate for a longer period of time resulting in additional 5094 kg or 11% of carbon dioxide released directly from the chemical reactions and emissions associated with higher energy requirement.

In Chapter 6, to compare the exergy usage of nanoproducts with the amount of exergy available, a unique exergy footprint analysis is developed based on the exergy footprint concept to create a quantitative lifecycle environmental impact metric to complement the use of LCA and exergy analysis. Based on the exergy footprint concept, the product lifecycle exergy consumption can be analyzed and compared with the exergy associated with national resource consumption, creating a novel exergy footprint normalized at the national level. It is worth mentioning that the concept of exergy footprint is different from that of ecological footprint. While ecological footprint accounts for the amount of land required to regenerate the material or to support the demand of a population or productive activity, exergy footprint focuses on the exergy of materials and electricity consumed.

As shown in this dissertation, physical characteristics can significantly affect their properties/behaviors including the motion in the gas medium, melting behaviors (supercooling and superheating), and specific heat capacity enhancement. The properties/behaviors of nanomaterials can create negative environmental impacts associated with the HTMR process including airborne of nanoparticles, process disruption, nanomaterials contaminants in the recovered products, larger energy consumption, and increased emission of CO_2 and waste gases. In Chapter 7, preliminary design-for-environment (DFE) guidelines for nanomaterials-containing products are developed to provide the designers with environmental benign design alternatives.

CHAPTER 6

DESIGN FOR ENVIRONMENT GUIDELINES

As discussed in Chapter 2, chemical composition is the primary factor affecting the degree of toxicity of bulk materials. However, at nanoscale, the degree of toxicity can become significantly different due to the effects of various physical characteristics including size, nanostructure, and host matrix type. At the EOL stage, these properties/behaviors can create significant negative environmental impacts associated with human health, eco-toxicity, and energy consumption, as well as the quality of the recovered metals. As shown in Figure 6.1, the physical characteristics of nanomaterials can be considered as design-for-environment (DFE) attributes that represent the dimensions of a 3D DFE design space that can help guide material selection decisions during the nanoproduct design and realization process.

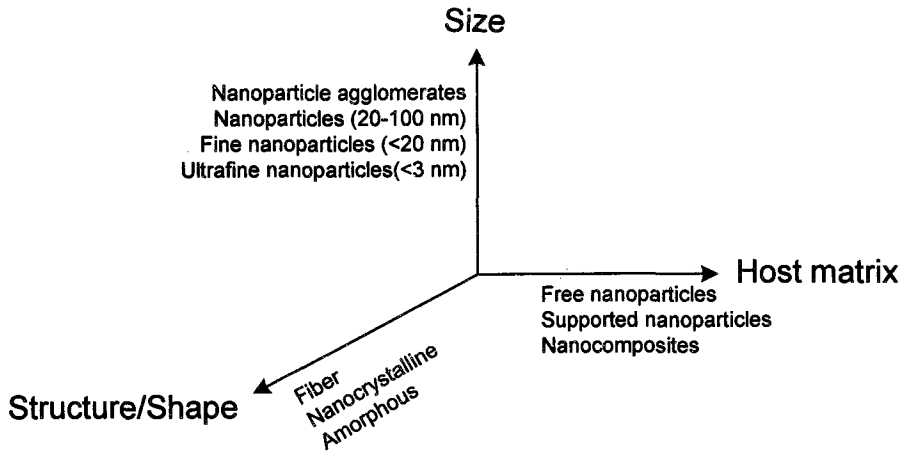

Figure 6.1 Generic DFE attributes and the 3D design space for nanomaterials.

6.1 Design-for-Environment Guidelines

In this section, design-for-environment (DFE) guidelines for nanomaterials-containing products are formulated to help product designers in selecting environmentally benign design alternatives. The guidelines are presented by nanomaterial design attribute: size, structure and host matrix.

Size

For nanoparticles, size is referred to as the diameter of particles. In case of high-aspect-ratio nanomaterials such as nanotubes, size is usually referred to as the outer diameter and/or the length of the tube. For thin film, size is referred to as the layer thickness. Size is segmented into four regions:

- Nanoparticle agglomerates
- Nanoparticles (20 - 100 nm)
- Fine nanoparticles (3 - 20 nm)
- Ultrafine nanoparticles (<3 nm)

Based on the results and research presented in previous chapters, the following DFE guidelines associated with the size of nanomaterials are suggested:

- The use of smaller nanoparticles is recommended for higher filtration efficiency. From the experimental results by Kim and et al. [Kim et al., 2006] described in Chapter 4, the size distribution of the incoming nanoparticles can be reorganized with respect to the filtration rating as shown in Table 6.1. For nanoparticles with diameters larger than a few nanometers, the filtration efficiency of standard industrial fibrous filters tends to increase as the size of nanoparticles decreases.

The table also implies that fibrous filters can achieve a 95% or better filtration efficiency only when the size of nanoparticles is below 6.5 nm.

- The use of very fine nanoparticles, with diameters on the order of a few nanometers, or nanocomposites containing these, should be avoided due to their ability to generate large melting point depression and elevation and to potentially create highly toxic effect due to the large surface area per volume ratio.

Table 6.1 Filtration Efficiency of a Glass Fibrous Filter for Nanoparticles

Filtration Efficiency	Particle diameter	Note
>99.97%	1.3-1.6 nm	100% filtration rating
>99%	below 4 nm	99% filtration rating
> 95%	below 6.5 nm	95% filtration rating
90-95%	6.5-8.5 nm	
85-90%	8.5-10.5 nm	
80-85%	10.5-12.5 nm	
70-80%	12.5-16.5 nm	
60-70%	16.5-21.5 nm	
50-60%	21.5-28.5 nm	
below 50%	28.5-100 nm	

Note: 100% level filter is required by ***Occupational Safety and Health Administration*** (OSHA) to filter highly toxic materials such as asbestos, cadmium, and lead.

Source: [Kim et al., 2006]

Structure/Shape

While thermal properties of nanomaterials can be affected by their atomic structure, the shape of the nanoparticles plays a key role affecting the filtration efficiency as well as the uptake and clearance mechanisms of nanoparticles in the human body. Structure and shape are characterized as fibers, nanocrystalline and amorphous structures.

As discussed in Chapter 2, the surface area of nanoparticles can be represented by a shape factor as shown in Table 6.2. The shape factor (α) is defined by the research of Qi, Wang and Liu [Qi et al., 2005] on size-dependent properties as the ratio of the surface area of nonspherical nanoparticles to that of spherical nanoparticles, where both of the nanoparticles have identical volume.

Table 6.2 Shape Factor of Nanoparticles

Particle shape	Shape factor (α)
Spherical	1
Regular tetrahedral	1.49
Regular hexahedral	1.24
Regular octahedral	1.18
Disk-like	>1.15

Source: [Qi et al., 2005]

From the literature review discussed in Chapter 2, previous research has shown that a high degree of supercooling and superheating tends to occur in nanoparticles with higher values of shape factor, due to the corresponding larger surface area to volume ratio. As a result, the following DFE guidelines are recommended to prevent the release of potentially toxic nanomaterials and the occurrence of unusually high or low melting temperatures of nanomaterials.

- The use of free-standing nanoparticles with high aspect ratios (or long fiber shape) structure should be avoided due it their asbestos-like toxicity.
- Use spherical nanoparticles whenever possible due to their higher filtration efficiency at low capture velocity compared to that of non-spherical nanoparticles.

- Small-sized nanoparticles with high shape factors must be used with caution due to their extremely large surface area per volume characteristics leading to the ability to generate chemical reactions with human cells, causing increased toxic effect, as well as the potential for large melting point depressions and elevations. While a high degree of superheating may be exhibited in encapsulated nanoparticles with high shape factors, a high degree of supercooling may exist in free nanoparticles with high shape factors.
- In general, the specific heat capacity of fiber-shaped nanomaterials and nanocrystal is higher than that of the corresponding amorphous and coarse-grained polycrystalline (material composed of aggregates of nanocrystallines). Amorphous nanomaterials can be used to prevent the occurrence of specific heat capacity enhancement.

Host Matrix

The host matrix can be classified as free-standing nanoparticles (free nanoparticles), supported nanoparticles, and nanocomposites. Supported nanoparticles are nanomaterials/nanoparticles that are supported by a substrate. This classification includes nanoparticles grown on top of a substrate or thin film coated on top of a substrate. Nanocomposite is a multiphase material where at least one of the phases is considered as a nanomaterial.

- When possible, use nanomaterials in the form of nanocomposites to avoid the release of free-standing nanoparticles during the shredding process.

- When using nanocomposites where nanoparticles are distributed within the host matrix, coating materials or the host matrix should exhibit melting temperatures that are lower than that of the embedded nanoparticles to prevent the occurrence of melting point elevation.
- Encapsulated carbonaceous nanomaterials such as doped CNTs may retain their structure throughout the recycling process if the amount of oxygen available during the reduction process is not sufficient to permit full reduction. CNTs should not be coated with metallic materials with melting points higher than the reduction temperature so that most of CNTs can be burnt off during reduction.
- Free standing nanoparticles and supported nanoparticles may be used to avoid the occurrence of a high degree of specific heat capacity enhancement which is observed in nanocomposites.

In addition to the DFE guidelines above, Table 6.3 is presented to illustrate the effects of the physical characteristics of nanomaterials on their properties/behaviors and the corresponding environmental impacts. In the Environmentally Responsible NanoProduct (ERNP) table an impact rating of high, moderate, or low is assigned for each corresponding property/behavior and environmental impact. The environmental impacts at the EOL stage contribute to five environmental impact analysis categories consisting of human health, eco-toxicity, resource depletion, global warming, and acidification. When applying the ERNP to a nanoproduct, particular concern must be given to the elements in the matrix containing high (or moderate) impact ratings, especially if multiple ranking fall above the moderate level.

Table 6.3 Environmentally Responsible Nanoproduct (ERNP) Assessment Matrix

			Environmental Impact Analysis Categories						
			Human health and Eco-toxicity			Resource depletion	Global warming and Acidification		
			Environmental and Process Impacts at the EOL Stage						
			Airborne nanoparticles	Acute toxic effects	Asbestos-like toxic effects	Nanomaterial contaminants	Higher process temperature	Process flow disruption	Higher energy consumption
			Properties/Behaviors of Nanomaterials						
			Brownian Motion	Large surface area per volume ratio	High aspect ratio structure	Superheating	Superheating	Supercooling	Specific heat capacity enhancement
Physical Characteristics	Size	Large	High	Low	-	Low	Low	Low	-
		Fine	Moderate	Moderate	-	Moderate	Moderate	Moderate	-
		Ultrafine	Low	High	-	High	High	High	-
	Structure	Amorphous	-	-	-	-	-	-	Low
		Nanocrystalline	-	-	-	-	-	-	Moderate
		Fiber	-	-	High	-	-	-	High
	Host Matrix	Free-standing	High	High	High	-	-	High	Low
		Substrate	Moderate	Moderate	Moderate	-	-	Moderate	Moderate
		Nanocomposite	Low	Low	Low	High	High	Low	High

Note: Designer concerns ranging from low level to high level, as represented by green and red colored cells, respectively.

To demonstrate the effects of the DFE attributes of size and host matrix for a single structure on the environmental impact at the EOL stage, the DFE design plane for nanocrystalline titanium oxide (TiO_2) is presented in Figure 6.2. With nanocrystalline structure, TiO_2 exhibits 30-35% specific heat capacity enhancement when the particle size is less than 20 nm, according to the previous heat capacity study [Wu, 2001]. At the same time, when the particle size is larger than about 6.5 nm, the filtration efficiency of a fibrous filter is less than 95%.

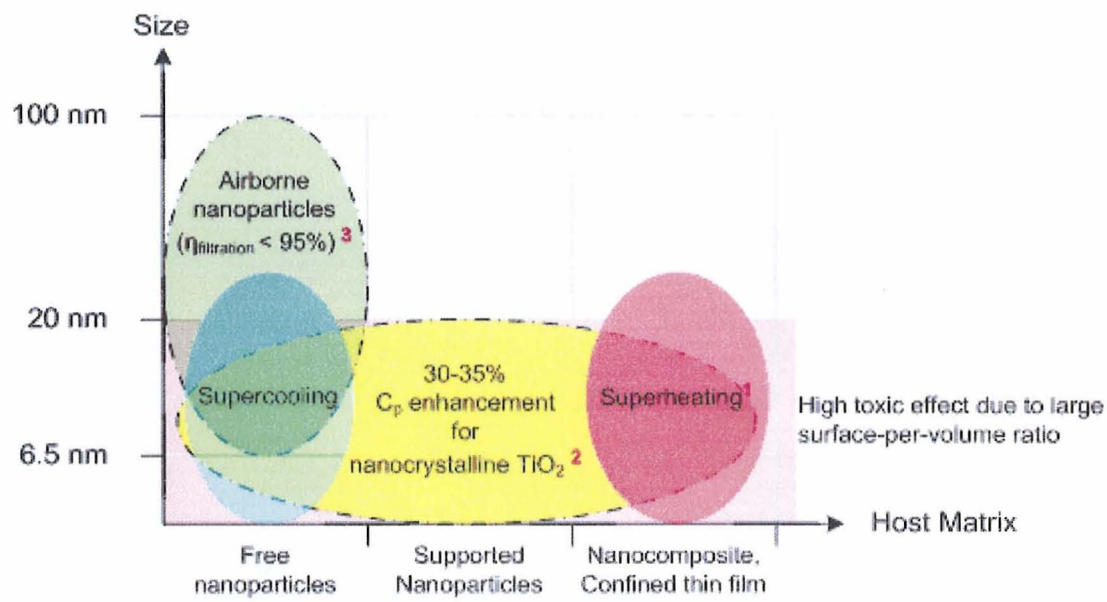

Figure 6.2 DFE design plane for nanocrystalline titanium oxide (TiO_2).

Note: [1] When the encapsulated nanoparticles are expitaxially bonded with the host matrix with higher melting point or when there is a huge difference in thermal expansion coefficients between the nanoparticles and the host matrix. [2] 30-35% C_p enhancement of TiO_2 at particle size of 20 nm is based on the heat capacity measurement by Wu, 2001. [3] The filtration efficiency of 95% for 6.5-nm nanoparticles is based on the study by Kim et al., 2006 where a traditional industrial-grade glass fibrous material is used as the filter media.

According to the DFE portfolio shown in Figure 6.2, the use of nanocrystalline TiO_2 in the form of fixed nanoparticles – supported nanoparticles and nanocomposite – is recommended to avoid the release of airborne nanoparticles. Moreover, the diameter of the nanocrystal should exceed 20 nm to prevent the occurrence of a high degree of supercooling, superheating, or specific heat capacity enhancement.

6.2 Recycling Process Recommendation

The following recycling process considerations are suggested:

- If possible, use electrostatic charged filtration systems for higher particle capture efficiency. Also, wet scrubbers may also generate sludge and waste water which may contain ultrafine nanoparticles
- For HTMR process consisting of the reduction and smelting processes, the premelting of nanomaterials with melting point depression may cause process flow disruption at the exit of the rotary hearth furnace (RHF) where the reduced iron is continuously discharged from the hearth of the furnace. The discharging system of the RHF should be capable of handling the materials in the form of liquid metals.

6.3 Discussion

The DFE guidelines for nanoproducts presented in this chapter of the dissertation are formulated based on the case study of high temperature battery recycling process. The environmentally benign design alternatives, as well as process recommendations, are given to avoid the release of potentially toxic nanomaterials, increase in energy consumption, and nanomaterial contamination in the reclaimed materials.

The guidelines are constructed with respect to the primary physical characteristics of nanomaterials—size, structure and host matrix—which are adopted as DFE attributes in this dissertation. The concept of an Environmentally Responsible Nanoproduct (ERNP) Assessment Matrix is constructed to illustrate the effect of the DFE attributed on the properties of nanomaterials and their corresponding potential environment impact. Finally, DFE design plane of nanocrystalline TiO_2 is constructed to demonstrate the effects of the DFE attributes on the environmental impact at the EOL stage.

CHAPTER 7

EXERGY FOOTPRINT ANALYSIS

7.1 Introduction

Lifecycle assessment (LCA) evaluates the environmental impact of material usage, energy consumption and environmental releases across the entire product lifecycle from raw material extraction and material synthesis to production, distribution, use and end-of-life management. The general structure for conducting an LCA is well-defined and documented in the ISO 14040 standard [ISO]. The basic methodology has been used for decades and is adapted from the original work by the Society of Environmental Toxicology and Chemistry (SETAC). The LCA methodology consists of four stages: Boundary and Scope; Lifecycle Inventory; Lifecycle Impact Analysis; and Interpretation. These stages are described as follows:

- Goal and Scope Definition: Define purpose and expected use of the study: set boundaries, assumptions, data collection technique, aggregation levels and results presentation.
- Lifecycle Inventory (LCI): An objective, data-driven process of quantifying energy usage, material flows, and environmental releases through out all lifecycle stages of the product, process or activity.
- Lifecycle Impact Assessment (LCIA): A technical, quantitative or semi-quantitative process to characterize and assess the effects of environmental

loading identified in the LCI. Typically, impact categories are defined that relate to the ecosystem, resource depletion and human health risks.

- Interpretation: A systematic evaluation of each step of the study to better understand assumptions and interpret results leading to improved environment performance.

While today there is almost universal acceptance of the overall methodology, there still exists significant disagreement on performing the actual impact analysis: the most important step in the overall procedure. The primary point of contention is the procedure for normalization and weighting, which takes various impact categories—such as global warming, ozone depletion, acidification, eutrophication, and resource depletion—and attempts to relate individual impact category quantities to a meaningful understanding of the actual impact on the environment.

Typically, normalization consists of defining a reference value for each impact category and calculating the ratio of the impact amount to the reference value. Normalization provides a scaling to interpret if the impact is large or small. For example, the quantity of global warming is characterized as the amount of lifecycle emissions of greenhouse gases (GHGs), measured in terms of CO_2 equivalence [Bates et al., 2008]. A typical reference value is the per capita quantity of total GHGs emitted annually by the entire region (e.g. Europe) or country (US) in which the LCA is based. Consequently, normalization yields a non-dimensional value for each impact category that reflects the relative size of the impact compared to the annual per capita emissions associated with entire region under study.

Weighting involves a decision as to the relative importance of each of the impact categories compared to each other. For example, the question being considered: is global warming a more important environmental issue than ozone depletion; and if so, is it 20% more important or 200% more important. Obviously, this is the least rigorous and least accepted step in the overall LCA process. Yet, normalization and weighting lead to a single quantitative value that *measures* overall environmental impact of the product, process or activity being studied; and, provides a single overall impact value which is easier for product designers, policy makers, and the general public to understand and take appropriate action.

7.2 Background

In this chapter, a novel approach to quantifying environmental impact is presented based on thermodynamic exergy analysis and is referred to as the Exergy Footprint. The exergy footprint has the potential to avoid the problems associated with the weighting procedure described above for traditional environmental impact analyses. In addition, the concept of exergy can be extended to include human activity and monetary flows, thereby making the exergy footprint a sustainability metric and not just an environmental impact metric.

The exergy footprint is structured similar to the widely used carbon footprint metric which focuses solely on greenhouse gas emissions. Instead of accounting for the consumption of only energy carriers and being concerned with the emission of CO_2, all resource consumption is considered in the exergy footprint: materials, water, energy even human and monetary capital. Consequently, the exergy footprint provides a comprehensive, sustainability view of the impact of a product, process or activity.

In order to make this approach useful, all consumption needs to be quantified in equivalent terms that allows the impacts to be compared directly and added to create a single-value metric. By using exergy as the same impact quantity for all resource consumptions and flows, the need to define, normalize and weight various impact categories is avoided. As discussed earlier in the dissertation, the application of exergy analysis to environmental issues is not new; however, the formalization into an exergy-based footprint with reference to per capita consumption has not been previously reported. The following describes the rationale for selecting thermodynamic LCA and using exergy as the common measure for the sustainability footprint:

- Exergy is based on sound scientific and engineering principles—the first and second laws of thermodynamics; consequently, the theoretical basis is well understood and universally accepted.
- All systems—physical, biological and ecological—are governed by the same fundamental principles; consequently, a single, unified theory underlies the analytical framework.
- The important, but often overlooked, differences in lifecycle temporal and spatial-specific characteristics can be incorporated in the footprint by defining a local reference environment for calculations.
- Exergy provides a common set of units to evaluate material flows, energy flows, process behavior and human body interaction with the surrounding environment.

- Exergy consumption has been widely accepted as an environmental metric relating increased entropy to environmental chaos, as described earlier in the dissertation.
- Exergy analysis has been used extensively to identify potential efficiency improvements in complex processes. Often times, energy analysis is misleading and fails to identify the inefficient process operation. Consequently, the Carbon Footprint method may also lead analysts to misjudge areas for improvement or contribute to other misleading results.

Although the exergy consumption alone has been shown to be useful, there needs to be a standard means for determining what these consumption numbers mean. In order to achieve this normalization, the total exergy consumption of the US per capita will be used. By using this reference value it will be possible to directly see how the consumption of exergy compares to the United States as a whole.

In order to determine this exergy consumption reference value the methods employed by Reistad [Reistad, 1975] and Ertesvag [Ertesvag, 2005] is used. Exergy analysis has been used to evaluate the exergy flow and the exergetic efficiency of several societies or countries around the world. In the mid-seventies, Reistad developed an approach to calculate the available energy (exergy) consumption in the US; however, his work was limited to energy carriers only. After that, Reistad approach has been applied to Finland [Wall, 1991], Canada [Rosen, 1992], Brazil [Schaeffer and Wirtshafter, 1992], and Turkey [Ileri and Gurer, 1998]. Similarly, Ertesvag and Mielnik performed an exergy analysis of the Norwegian society [Ertesvag and Mielnik, 2000]; Wall studied

exergy conversion in the Japanese society [Wall, 1990]; and, Chen and Chen analyzed the Chinese society [Chen and Chen, 2007, 2009]. These studies extended Reistad's work to include exergy of materials as well as just energy carriers. In addition, Ukidwe and Bakshi examined resource intensities of chemical sectors in the US using input-output models [Ukidwe and Bakshi, 2007].

7.3 Approach

As mentioned earlier, several previous studies have used exergy concepts to evaluate the exergetic efficiency of a society or a country and to identify resource utilization improvement opportunities. However, this dissertation focuses only on the input exergy flow of a society. Therefore, the exergy content of resources are quantified based the functional aspect intended by the society. In other words, the exergy content of resources is quantified based on their purpose of use. The exergy of fuel materials, whose energy is extracted by combustion, is calculated based on their heating value and the quality factor. Quality factor, referred to as exergy factor in some studies, is the exergy to energy ratio [Wall, 1977]. For non-fuel materials, chemical exergy is generally used as a measure of their maximum useful work potential relative to the surroundings or the specified reference state. In the case of construction materials, structural exergy may be more appropriate as a measure of their potential since their chemical potential will not be utilized by the society.

In this dissertation, the consumption and flow of exergy in the US economy will be defined in terms of five functional categories: materials, transportation, food, water, and direct energy carriers. Materials will account for the exergy associated with minerals

and material consumption. Transportation will account for all exergy from energy sources used for transporting goods and people. Food will include exergy content of food items in terms of calorific values. The exergy of water will be the chemical exergy of consumed water. Direct energy carriers accounts for the exergy due to energy consumed directly by the end user. These categories will give the ability to not only quantify that excess exergy is being consumed but will also identify how the exergy is being consumed and indicate where would be the best place to reduce consumption. The following provides additional details in developing the reference level for the total exergy consumption per capita in the US:

Fossil fuel and renewable energy

$$Exergy = Gross\ Heating\ Value \times Quality\ Factor$$

Gross heating value or the higher heating value (HHV) is used in this dissertation as it is used by Energy Information Administration (EIA) to represent the heat content of combustible materials. However, net heating value or lower heating value (LHV) is used to represent the exergy of fuelwood and fossil fuel in previous studies using Wall's approach (i.e. the analysis of Sweden, Italy and Japan). Heating value is the amount of heat released during combustion of the material. The latent heat of vaporization of water released from the material during the combustion is included in HHV, but not in LHV. Consequently, the HHV and LHV of a material are approximately the same when its moisture content is low.

Fresh and saline water

Chemical exergy of both fresh and saline water is assumed to be 50 MJ/m^3 [Bosch et al., 2007]. Saline water is defined as water containing dissolved solids of 1,000 milligrams per liter or more.

Food and beverage

Calorific value (or nutritional value) obtained from USDA National Nutrient Database [USDA] is used in this dissertation as the exergy content of food and beverage. In the analyses of Japan [Wall, 1990], Italy [Wall et al., 1994], and Brazil [Schaeffer and Wirtshafter, 1992], the exergy of food is equivalent to the recommended daily intake of about 2600 kcal/capita or 4 GJ/capita annually. The value is varied depending on the age distribution of the population of each country.

Construction materials and metals

Chemical exergy is used for construction materials and metals. As presented in Chapter 5, the chemical exergy is the product of the standard chemical exergy for the material and the number of moles of the material used.

Paper and wood

The exergy content of 10.44 GJ/m^3 is used for fuel wood with density of about $750kg/m^3$ and moisture content of 20% [FAO]. The exergy content of 17 GJ/ton is used for paper and 8 GJ/m^3 is used for construction wood with density of $450kg/m^3$ and moisture content of 25%. The chemical content of paper is approximately the same as that of

cellulose which the main composition of wood pulp used as the raw material for paper. The values of construction wood and paper are commonly used in the previous exergy analysis studies such as the exergy analyses of Norway [Ertesvag and Mielnik, 2000], Sweden [Wall, 1994], and Japan [Wall, 1990].

7.4 Exergy Analysis of the United States

The resource consumption amount shown in this section is the apparent consumption which is calculated based on the production, import, and export amounts. The change in the stock amount may be considered.

$$\textit{Apparent Consumption} = \textit{Production} + \textit{Imports} - \textit{Exports} \pm \textit{(Stock Change)}$$

The annual US exergy consumption of various energy carriers is calculated based on the 2008 US energy consumption data obtained from EIA [EIA] and the quality factor, as shown in Table 7.1. The exergy consumption by the transportation sector, shown in Table 7.2, is excluded from the quantities presented in Table 7.1 so as to avoid double counting energy flows. The energy carriers are primarily divided into fossil fuel (non-renewable energy) and renewable energy. The entry Electricity retail sales is defined by EIA as "the electricity retail sales to ultimate customers reported by electric utilities and other energy service providers" [EIA]. It is the amount consumed by customers that is not reported in other energy carrier categories. The losses are also included in the consumption quantity as they are considered as part of the input of the society. From Tables 7.1 and 7.2, the total US exergy consumption in 2008 is 485 GJ/capita, which is about 50% higher than the value of US in 1970 reported by Reistad (321 GJ/capita)

[Reistad, 1975]. Since the US energy consumption per capita has increased approximately 50% since 1970, the value calculated here for 2008 US exergy consumption is reasonable.

Table 7.1 Annual US Exergy Consumption of Energy Carriers

Energy Carrier		Quality Factor	Energy (Billion Btu)	Exergy	
				(PJ)	(GJ/capita)
Fossil Fuel	Coal	1.03	22,461,190	24,409	80.3
	Natural gas	0.92	23,170,423	22,490	74.0
	Petroleum	1.06	10,804,685	12,084	39.8
Renewable Energy	Nuclear	0.95	8,455,236	8,475	27.9
	Hydroelectric Power	1.00	2,452,073	2,587	8.5
	Geothermal	0.29	358,497	110	0.4
	Solar/PV	0.93	91,003	89	0.3
	Wind	1.00	514,224	543	1.8
	Biomass	1.05	3,051,302	3,380	11.1
Electricity Retail Sales		1.00	12,697,972	13,397	44.1
Electrical System Energy Losses		1.00	27,392,376	28,900	95.1
Total				116,464	383.3

Note: 2008 US population is 303,824,640 [CIA].

Source for 2008 annual energy consumption: [EIA]
Source for the quality factor: [Ertesvag and Mielnik, 2000] for fossil fuel, [Wall, 1989] for Nuclear, and [Ileri and Gurer, 1995] for the remaining renewable energy carriers (Quality factor of wind power is assumed to be 1)

Table 7.2 Annual US Exergy Consumption of Energy Carriers for Transportation

Energy Carrier	Quality Factor	Energy (Billion Btu)	Exergy	
			(PJ)	(GJ/capita)
Natural gas	0.92	677,193	657	2.2
Petroleum	1.06	26,331,990	29,449	96.9
Biomass	1.05	832,950	923	3.0
Total		27,842,133	31,029	102.1

Note: These quantities are not included in Table 7.1.

Source for 2008 annual US energy consumption: [EIA]

The annual US exergy consumption of water, foods and beverages, and materials is shown in Tables 7.3 to 7.5, respectively.

Table 7.3 Annual US Exergy Consumption of Water

Water	Exergy (MJ/m^3)	Consumption (Million gal)	Exergy	
			(PJ)	(GJ/capita)
Fresh	50	127,385,000	24,108	79.3
Saline		22,265,000	4,214	13.9
Total		149,650,000	28,321	93.2

Source of water consumption: [Kenny et al., 2009]

Table 7.4 Annual US Exergy Consumption of Foods and Beverages

Food and Beverage	Consumption (lb/capita)	Exergy (GJ/capita)
Red Meat and Poultry	276	1.30
Fish and Shell Fish	16	0.04
Daily Products and Egg	310	0.63
Fruits and Nuts	273	0.37
Vegetables	417	0.51
Fats and Oils	82	1.34
Beverage and Sweetener	754	1.95
Total	2,128	6.14

Source of foods and beverages consumption: [USDA, 2009]

Table 7.5 Annual US Exergy Consumption of Materials

Materials	Consumption (Metric ton)	Exergy	
		(PJ)	(GJ/capita)
Construction Materials	3,244,980,064	595	2.0
Metals	315,462,924	1,117	3.7
Agricultural Products	4,955,279	0	0.0
Paper	92,500,000	1,573	5.2
Fuelwood	36,754,600	556	1.8
Construction Wood	55,145,400	980	3.2
Total	3,749,798,267	4,821	15.9

Note: The exergy of wood and paper is based on the lower heating value as described in the previous section of the chapter. Structural exergy of wood and paper may be used to improve the estimation of the exergy content of non-fuel wood and paper.

Source: [USGS] for construction materials (denoted as minerals by the source), metals, and agricultural products; [Matos, 2009] for paper and construction wood; [FAO] for fuelwood

The total exergy consumption in 2008 is about 182,500 PJ or 601 GJ/capita. The overview of the annual US exergy consumption in 2008 is presented in Figure 7.1. The US exergy consumption and average carbon footprint per person in the US is compared to various countries as shown in Figure 7.2.

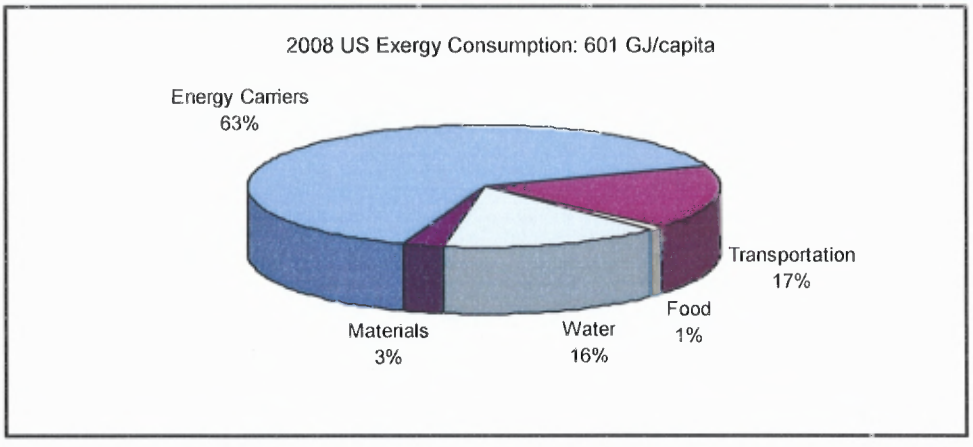

Figure 7.1 2008 US exergy consumption.

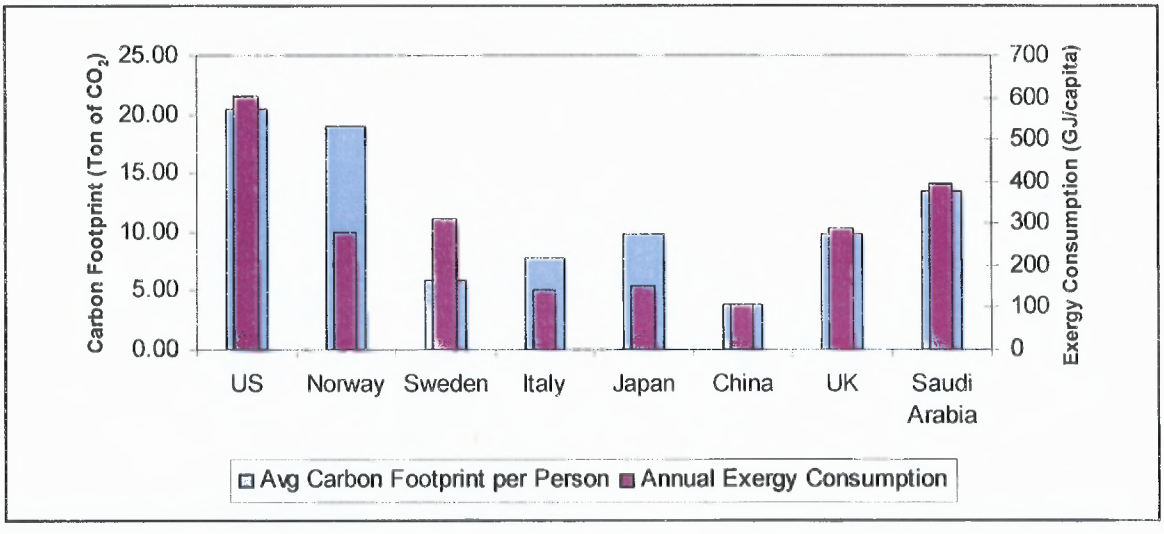

Figure 7.2 Exergy Footprint: A Comparison with National Carbon Footprints.

Source: [Ertesvag and Mielnik, 2000] for Norway; [Wall, 1997] for Sweden; [Wall, 1994] for Italy; [Wall, 1990] for Japan; [Chen and Chen, 2009] for China; [Gasparatos et al., 2009] for UK; [Dincer et al., 2004] for Saudi Arabia

7.5 Exergy Footprint of the HTMR Process

In this dissertation, the environmental impact of the HTMR process due to the processing of nanomaterial-containing Li-ion batteries is normalized to the annual US exergy consumption and expressed in terms of the exergy footprint of the process. The exergy loss associated with the HTMR process with the existing operating condition and with the higher smelting temperature needed to melting down superheated nanomaterials are expressed in the terms of the exergy footprint as shown in Table 7.6.

Table 7.6 Exergy Footprint of the HTMR Process

HTMR Process	Annual Exergy Loss		Exergy Footprint
	(PJ)	(GJ/capita)	(millipoints)
Existing Operating Condition	182	0.601	1.000
150% Smelting Temperature	193	0.634	1.056

Note: 2008 Annual US exergy consumption for the energy carrier section is 600.7 GJ/capita. And, from Chapter 5 analysis, the HTMR process exergy loss for the existing operation and the higher smelting temperature operation is 347.2 GJ/hr and 366.6 GJ/hr, respectively.

Millipoint is equal to 10^{-3}.

7.6 Discussion

Exergy concept has long been used to identify the potential improvement of a process, a society, or a country. In this dissertation, exergy-based environmental performance metric is created based on the exergy concept and expressed as the annual US exergy consumption. Input flows of resources are expressed in the common unit of exergy, eliminating the need for normalization and weighting among various categories of resources. Consequently, the exergy footprint avoids this major problem inherent in traditional lifecycle impact assessment methods.

After that, the environmental impact associated with the HTMR process represented by the amount of exergy loss is compared with the US exergy consumption. The resulting exergy footprint can be used to benchmark the environmental performance of each process, as compared to the exergy consumption at the national level. Process with larger exergy footprint will dissipate more exergy into the environment and creating a higher degree of environmental impact. DFE guidelines presented in Chapter 6 could be implemented to reduce the thermodynamic losses, leading to more sustainable product design. The concept of exergy can be extended to include human activity and monetary flows, thereby making the exergy footprint a true sustainability metric and not just an environmental impact metric.

APPENDIX A

ENERGY AND EXERGY FLOWS AT THE REDUCTION PROCESS

Process: Reduction Operating Temperature: 1523 K
Cycle time: 60 min. Ambient Temperature: 298 K
Electrical energy consumed: 38.5 GJ

Assumption: Only the chemical exergy, Ex_{ch}, of reducing agent, metal oxides, and reduced metals is used in calculating the system performances and, hence, shown in Appendix A and B.

Table A.1 Inputs of Reduction Process

Material	Composition	Molecular Weight (g/mol)	Mass (Kg)	Ex_{ch} (KJ/mol)	Ex_{ch} (GJ)
Green Pellet and Iron Shot	Fe	55.80	9100	376.4	61.2
	Fe2O3	159.70	22000	16.5	2.3
	MnO	157.90	500	135.5	0.8
	C	12.00	10800	410.3	369.3
	Others	-	750	-	-
Oxygen		32.00	18600	4.0	2.3

Note: The value of energy and thermal exergy of input materials at the reduction process are equal to zero as their temperature is the same as ambient temperature.

Table A.2 Outputs of Reduction Process

Composition		Molecular Weight (g/mol)	Mass (Kg)	C_p (KJ/Kg.K)	Ex_{Ch} (KJ/mol)	E (GJ)	Ex_{Th} (GJ)	Ex_{Ch} (GJ)
Sponge Iron	Fe	55.80	20,651	0.71	376.4	17.893	10.792	139.30
	Fe_2O_3	159.70	2295	0.90	16.5	2.534	1.529	0.24
	Mn	55.00	150	0.48	410.2	0.088	0.053	1.12
	MnO	157.90	300	0.46	135.5	0.169	0.102	0.26
	C	12.00	2142	0.69	410.3	1.798	1.084	73.24
Waste Gases	Fe	55.85	44	0.71	376.4	0.039	0.023	0.30
	ZnO	65.39	1111	0.32	-	0.432	0.261	-
	Zn (salt)	65.39	132	0.32	-	0.051	0.031	-
	Pb	207.21	239	0.14	-	0.041	0.025	-
	Cd	112.41	4	0.23	-	0.001	0.001	-
	Sn	118.71	4	0.23	-	0.001	0.001	-
	Cr	52.00	2	0.80	-	0.001	0.001	-
	Ca	40.08	4	0.87	-	0.004	0.003	-
	Al	26.98	6	1.18	-	0.009	0.005	-
	Na	22.99	137	0.90	-	0.151	0.091	-
	K	39.10	58	0.53	-	0.038	0.023	-
	C	12.01	186	0.69	410.3	0.156	0.094	6.34
	S	32.07	243	0.66	-	0.197	0.119	-
	Cl	35.45	393	0.61	-	0.294	0.177	-
	F	19.00	43	1.11	-	0.058	0.035	-
	O	16.00	426	1.30	-	0.679	0.410	-
CO_2		44.00	8043*	1.33	19.9	13.10	-	-
			33500**			-	32.92	15.15

* The amount is calculated based on mass-balance chemical reaction equations
** The amount is calculated based on exergy-balance chemical reaction equations

APPENDIX B

ENERGY AND EXERGY FLOWS AT THE SMELTING PROCESS

Process: Smelting Operating Temperature: 1973 K
Cycle time: 60 min.
Electrical energy consumed: 67 GJ

Assumption: The input of the smelting process is equivalent to the output of the reduction process. Only the output of the smelting process is presented.

Table B.1 Outputs of Smelting Process

Composition		Molecular Weight (g/mol)	Mass (Kg)	C_p (KJ/Kg.K)	Ex_{Ch} (KJ/mol)	E (GJ)	Ex_{Th} (GJ)	Ex_{Ch} (GJ)
Molten Metal	Ni	58.71	1698	0.66	-	1.885	1.251	-
	Cr	51.996	2817	0.99	-	4.678	3.105	-
	Fe	55.8452	22100	0.82	376.4	30.507	20.248	148.96
	Mn	54.938	320	0.84	410.2	0.449	0.298	2.39
	Mo	95.94	200	0.38	-	0.127	0.085	-
	Cu	63.546	140	0.52	-	0.121	0.080	-
	Co	58.933	80	0.69	-	0.092	0.061	-
	S	32.06	60	0.66	-	0.067	0.044	-
	C	12.011	739	0.69	410.3	0.848	0.563	25.25
	Si	28.085	20	0.97	-	0.032	0.022	-
	P	30.974	10	0.68	-	0.011	0.008	-
Slag	SiO_2	60.1	1589	1.43	-	3.800	2.522	-
	MgO	40.3	1126	1.38	-	2.601	1.726	-
	Cr_2O_3	152.0	331	0.91	-	0.502	0.333	-
	CaO	56.1	2119	1.04	-	3.694	2.452	-
	Al_2O_3	102.0	662	1.34	-	1.483	0.984	-
	Fe_2O_3	159.7	199	0.92	16.5	0.306	0.203	0.02
Scrubber Filter Cake and Baghouse Dust	SiO_2	60.1	99.89	1.427527	-	0.239	0.159	-
	Al_2O_3	102.0	99.89	1.337352	-	0.224	0.149	-
	CaO	56.1	179.8	1.040879	-	0.313	0.208	-
	MgO	40.3	179.8	1.379574	-	0.415	0.276	-
	F	19.0	79.91	1.101565	-	0.147	0.098	-
	Cl	35.5	189.8	0.603232	-	0.192	0.127	-
	Pb	207.2	199.8	0.141771	-	0.047	0.031	-
	Zn	65.4	998.9	0.317842	-	0.532	0.353	-
	Fe	55.8	219.7	0.824135	376.4	0.303	0.201	1.48
	Cr	52.0	69.92	0.756403	-	0.089	0.059	-
CO_2		44.00	865	1.33	19.9	1.926	-	-
		44.00	3906	1.33	19.9	-	5.774	1.77

* The amount is calculated based mass-balance chemical reaction equations
** The amount is calculated based exergy-balance chemical reaction equations

REFERENCES

Accurec http://www.accurec.de (date accessed 5/5/2008).

Altairnano, Altair's battery electrode materials. *American Ceramic Society Bulletin* **2005,** *84*, (1).

Altamirano-Lozano, M., Beyersmann, D., Carter, D.E., Fowler, B.A., Fubini, B., Kielhorn, J., Kirsch-Volders, M., Kucera, J., Kusaka, Y., Lasfargues, G., Lison, D., Mangelsdor, I., McElvenny, D., Nemery, B., Roycroft, J., Svartengren, M., Junghans, T., Olin, S., Renne, R., Longfellow, D.G., Ziegler-Skylakakis, K., Baan, R., Cogliano, V., El Ghissassi, F., Fletcher, T., Friesen, M., Grosse, Y., Napalkov, N., Secretan, B., Straif, K., Wang, Z.-Q., Williams, R., Cobalt in hard metals and cobalt sulfate, gallium arsenide, indium phosphide and vanadium pentoxide. *IARC Monographs on the Evaluation of Carcinogenic Risks to Humans* **2006,** *86*, 1-292.

Amine, K., Liu, J., Belharouak, I., Kang, S.-H., Bloom, I., Vissers, D., Henriksen, G., Advanced cathode materials for high-power applications. *Journal of Power Sources* **2005,** *146*, (1-2), 111-115.

Ao, Y., Gunnewiek, L., Rosen, M.A., Critical review of exergy-based indicators for the environmental impact of emissions. *International Journal of Green Energy* **2008,** *5*, (1-2), 87-104.

Bachels, T., Guntherodt, H.-J., Schafer, R., Melting of isolated tin nanoparticles. *Physical Review Letters* **2000,** *85*, (6), 1250-1253.

Bakshi, B. R., Ukidwe, N.U. In *The role of thermodynamics in life cycle assessment of existing and emerging technologies*, IEEE International Symposium on Electronics and the Environment 2006, 2006; pp 15-20.

Banhart, F., Hernandez, E., Terrones, M., Extreme superheating and supercooling of encapsulated metals in fullerenelike shells. *Physical Review Letters* **2003,** *90*, (18), 185502/1-185502/4.

Barsukov, I. V., Gallego, M.A., Doninger, J.E., Novel materials for electrochemical power sources - Introduction of PUREBLACK® Carbons. *Journal of Power Sources* **2006,** *153*, (2), 288-299.

Bates, B. C., Kundzewicz, Z.W., Wu, S., Palutikof, J.P., Climate Change and Water. 2008.

Batrec http://www.batrec.ch/en-us (date accessed 5/5/2008).

Bauer, K. H., Huette, D., Lehmkuehler, H.J., Schmauch, H., Recycling of iron and steelworks wastes using the inmetco direct reduction process. *MPT. Metallurgical plant and technology* **1990,** *13*, (4).

Baumgartner, S., Faber, M., Schiller, J., *Joint Production and Responsibility in Ecological Economics: On the Foundations of Environmental Policy*. Edward Elgar Publishing Inc.: 2006.

Becker, M. L., Fagan, J.A., Gallant, N.D., Bauer, B.J., Bajpai, V., Hobbie, E.K., Lacerda, S.H., Migler, K.B., Jakupciak, J.P., Length-dependent uptake of DNA-wrapped single-walled carbon nanotubes. *Advanced Materials* **2007,** *19*, (7), 939-945.

Bosch, M. E., Hellweg, S., Huijbregts, M.A.J., Frischknecht, R., Applying Cumulative Exergy Demand (CExD) indicators to the ecoinvent database. *International Journal of Life Cycle Assessment* **2007,** *12*, (3), 181-190.

Boskovic, L., Agranovski, I.E., Altman, I.S., Braddock, R.D., Filter efficiency as a function of nanoparticle velocity and shape. *Journal of Aerosol Science* **2008,** *39*, (7), 635-644.

Boskovic, L., Altman, I.S., Agranovski, I.E., Braddock, R.D., Myojo, T., Choi, M., Influence of particle shape on filtration processes. *Aerosol Science and Technology* **2005,** *39*, (12), 1184-1190.

Boyanov, S., Annou, K., Villevieille, C., Pelosi, M., Zitoun, D., Monconduit, L., Nanostructured transition metal phosphide as negative electrode for lithium-ion batteries. *Ionics* **2008,** *14*, (3), 183-190.

BPS www.baghousepart.com. (date accessed 12/4/2009).

Brown, D. M., Wilson, M.R., MacNee, W., Stone, V., Donaldson, K., Size-dependent proinflammatory effects of ultrafine polystyrene particles: A role for surface area and oxidative stress in the enhanced activity of ultrafines. *Toxicology and Applied Pharmacology* **2001,** *175*, (3), 191-199.

Busey, R. H., Giauque, W.F., The heat capacity of nickel from 15 to 300°K. Entropy and free energy functions. *Journal of the American Chemical Society* **1952,** *74*, (12), 3157-3158.

Camdali, U., and Tunc, M., Modeling of electric energy consumption in the AC electric arc furnace. *International Journal of Energy Research* **2002,** *26*, 935-947.

Chan, C. K., Peng, H., Liu, G., Mcilwrath, K., Zhang, X.F., Huggins, R.A., Cui, Y., High-performance lithium battery anodes using silicon nanowires. *Nature Nanotechnology* **2008,** *3*, (1), 31-35.

Chandra Bose, A., Kalpana, D., Thangadurai, P., Ramasamy, S., Synthesis and characterization of nanocrystalline SnO_2 and fabrication of lithium cell using nano-SnO_2. *Journal of Power Sources* **2002,** *138-141*, (107), 1.

ChematGroup http://www.chemat.com/html/solgel.html (date accessed 5/5/2008).

Chen, G. Q., Chen, B., Extended-exergy analysis of the Chinese society. *Energy* **2009,** *34*, (9), 1127-1144.

Chen, G. Q., Chen, B., Resource analysis of the Chinese society 1980-2002 based on exergy-Part 1: Fossil fuels and energy minerals. *Energy Policy* **2007,** *35*, (4), 2038-2050.

Chen, G., *Nanoscale Energy Transport and Conversion.* Oxford University Press: 2005.

Chen, Z., Meng, H., Xing, G., Chen, C., Zhao, Y., Jia, G., Wang, T., Yuan, H., Ye, C., Zhao, F., Chai, Z., Zhu, C., Fang, X., Ma, B., Wan, L., Acute toxicological effects of copper nanoparticles in vivo. *Toxicology Letters* **2006,** *163*, (2), 109-120.

Chiang, I. W., Brinson, B.E., Huang, A.Y., Willis, P.A., Bronikowski, M.J., Margrave, J.L., Smalley, R.E., Hauge, R.H., Purification and characterization of single-wall carbon nanotubes (SWNTs) obtained from the gas-phase decomposition of CO (HiPCO process). *Journal of Physical Chemistry B* **2001,** *105*, (35), 8297-8301.

Chiang, Y. M., Gozdz, A.S., Payne, M.W. Nanoscale ion storage materials. US Patent 0190418, 2007.

CIA, The World Fact Book. (date accessed 11/25/2009).

Citron http://www.citron.ch/ (date accessed 5/5/2008).

De Haar, C., Hassing, I., Bol, M., Bleumink, R., Pieters, R., Ultrafine but not fine particulate matter causes airway inflammation and allergic airway sensitization to co-administered antigen in mice. *Clinical and Experimental Allergy* **2006,** *36*, (11), 1469-1479.

Dincer, I., Hussain, M.M., Al-Zaharnah, I., Analysis of sectoral energy and exergy use of Saudi Arabia. *International Journal of Energy Research* **2004,** *28*, (3), 205-243.

Donaldson, K., Aitken, R., Tran, L., Stone, V., Duffin, R., Forrest, G., Alexander, A., Carbon nanotubes: A review of their properties in relation to pulmonary toxicology and workplace safety. *Toxicological Sciences* **2006,** *92*, (1), 5-22.

Donaldson, K., Stone, V., Borm, P.J.A., Jimenez, L.A., Gilmour, P.S., Schins, R.P.F., Knaapen, A.M., Rahman, I., Faux, S.P., Brown, D.M., MacNee, W., Oxidative stress and calcium signaling in the adverse effects of environmental particles (PM10). *Free Radical Biology and Medicine* **2003,** *34*, (11), 1369-1382.

Donaldson, K., Tran, C.L., An introduction to the short-term toxicology of respirable industrial fibres. *Mutation Research - Fundamental and Molecular Mechanisms of Mutagenesis* **2004,** *553*, (1-2), 5-9.

Dumortier, H., Lacotte, S., Pastorin, G., Marega, R., Wu, W., Bonifazi, D., Briand, J.-P., Prato, M., Muller, S., Bianco, A., Functionalized carbon nanotubes are non-cytotoxic and preserve the functionality of primary immune cells. *Nano Letters* **2006,** *6*, (7), 1522-1528.

Edelstein, E. S., Cammaratra, R.C., *Nanomaterials: Synthesis, Properties and Applications.* Taylor & Francis: 1998.

EIA, Annual Energy Review 2008.

Eltron Research Inc., Combustion synthesis of nanoparticle metal phosphate cathode materials for improved lithium ion batteries.

Endo, M., Grow carbon fibers in the vapor phase. *Chemtech* **1988,** *18*, (9), 568-576.

Endo, M., Hayashi, T., Kim, Y.A., Muramatsu, H., Development and application of carbon nanotubes. *Japanese Journal of Applied Physics, Part 1: Regular Papers and Short Notes and Review Papers* **2006,** *45*, (6A), 4883-4892.

Enerdel http://enerdel.com (date accessed 5/5/2008).

Ertesvag, I. S., Energy, exergy, and extended-exergy analysis of the Norwegian society 2000. *Energy* **2005,** *30*, (5), 649-675.

Ertesvag, I. S., Mielnik, M., Exergy analysis of the Norwegian society. *Energy* **2000,** *25*, (10), 957-973.

FAO ForesSTAT. http://faostat.fao.org (date accessed 11/25/2009).

Frenay, J., Ancia, P.H., Preschia, M., Minerallurgical and metallurgical processes for the recycling of used domestic batteries. *Proceedings of the Second International Conference on Recycling of Metals* **1994**, 13-20.

Frohlich, S., Sewing, D., The BATENUS process for recycling mixed battery waste. *Journal of Power Sources* **1995,** *57*, (1-2), 27-30.

Gaggioli, R. A., Richardson, D.H., Bowman, A.J., Available energy - Part I: Gibbs revisited. *Journal of Energy Resources Technology* **2002,** *124*, 105-109.

Gao, B., Kleinhammes, A., Tang, X.P., Bower, C., Fleming, L., Wu, Y., Zhou, O., Electrochemical intercalation of single-walled carbon nanotubes with lithium. *Chemical Physics Letters* **1999,** *307*, (3-4), 153-157.

Gasparatos, A., El-Haram, M., Horner, M., Assessing the sustainability of the UK society using thermodynamic concepts: Part 2. *Renewable and Sustainable Energy Reviews* **2009,** *13*, (5), 956-970.

Goldstein, A. N., Echer, C.M., Alivisatos, A.P., Melting in semiconductor nanocrystals. *Science* **1992,** *256*, (5062), 1425-1427.

Government, B. C., Water quality guidelines for cobalt.

Gozdz, A. S., Chu, A.C., Chiang, Y.M., Riley, Jr., G.N. Lithium secondary cell with high charge and discharge rate capability. US Patent 7261979, 2007.

Graetz, J., Ahn, C.C., Yazami, R., Fultz, B., Highly reversible lithium storage in nanostructured silicon. *Electrochemical and Solid-State Letters* **2003,** *6*, A194-A197.

Grubb, G. F., Bakshi, B.R. In *Energetic and environmental evaluation of titanium dioxide nanoparticles*, IEEE International Symposium on Electronics and the Environment, 2008.

Gupta, S. K., Talati, M., Jha, P.K., Shape and size dependent melting point temperature of nanoparticles. *Materials Science Forum* **2008,** *570*, 132-137.

Hanewald, R. H., Schweers, M.E., Liotta, J.J. In *Recycling nickel-cadmium batteries through the high temperature metal recovery process and New cadmium recovery facility*, Proceedings of the Annual Battery Conference on Applications and Advances, 1996; pp 207-212.

Hatch, J. E., *Aluminum: properties and physical metallurgy*. ASM International: 1984.

Hazards Magazine, Killing the future: asbestos use in Asia, international ban asbestos secretariat. 2007.

Healy, M. L., Dahlben, L.J., Isaacs, J.A., Environmental assessment of single-walled carbon nanotube processes. *Journal of Industrial Ecology* **2008,** *12*, (3), 376-393.

Henan Hongji Mine Machinary Co., L. http://hongjijituan.en.made-in-china.com/product/FeOnwsmxbfUp/China-Disc-Pelletizers.html (date accessed 12/4/2009).

Heyder, J., Deposition of inhaled particles in the human respiratory tract and consequences for regional targeting in respiratory drug delivery. *Proc Am Thorac Soc* **2004,** *1*, (4), 315-320.

Hsu, K. F., Tsay, S.Y., Hwang, B.J., Synthesis and characterization of nano-sized $LiFePO_4$ cathode materials prepared by a citric acid-based sol-gel route. *Journal of Materials Chemistry* **2004,** *14*, (17), 2690-2695.

Huang, S. H., Chen, C.W., Chang, C.P., Lai, C.Y., Chen, C.C., Penetration of 4.5 nm to 10 μm aerosol particles through fibrous filters. *Journal of Aerosol Science* **2007,** *38*, (7), 719-727.

Ijima, S., Helical microtubules of graphitic carbon. *Nature* **1991,** *354*, (6348), 56-58.

Ileri, A., Gurer, T., Energy and exergy utilization in Turkey during 1995. *Energy* **1998,** *23*, (12), 1099-1106.

Isaacs, J. A., Tanwani, A., Healy, M.L. In *Environmental assessment of SWNT production*, IEEE International Symposium on Electronics and the Environment, 2006; pp 38-41.

ISO http://www.iso.org (date accessed 12/18/2008).

Jeremy, J. *Understanding Electric Arc Furnace Operations*; Carnegie Mellon University: 1997.

Jin, Z. H., Sheng, H.W., Lu, K., Melting of Pb clusters without free surfaces. *Physical Review B - Condensed Matter and Materials Physics* **1999,** *60*, (1), 141-149.

Jugovic, D., Uskokovic, D., A review of recent developments in the synthesis procedures of lithium iron phosphate powders. *Journal of Power Sources* **2009,** *190*, (2), 538-544.

Kaewamatawong, T., Kawamura, N., Okajima, M., Sawada, M., Morita, T., Shimada, A., Acute pulmonary toxicity caused by exposure to colloidal silica: Particle size dependent pathological changes in mice. *Toxicologic Pathology* **2005,** *33*, (7), 745-751.

Kasavajjula, U., Wang, C., Appleby, A.J., Nano- and bulk-silicon-based insertion anodes for lithium-ion secondary cells. *Journal of Power Sources* **2007,** *163*, (2), 1003-1039.

Kawatra, S. K., Ripke, S.J., Pelletizing steel mill desulfurization slag. *International Journal of Mineral Processing* **2002,** *65*, (3-4), 165-175

Keegel, J., J. F. Methods for recycling electric arc furnace dust. US Patent 5538532, 1996.

Khanna, V., Bakshi, B.R., Carbon nanofiber polymer composites: Evaluation of life cycle energy use. *Environmental Science and Technology* **2009,** *43*, (6), 2078-2084.

Khanna, V., Bakshi, B.R., Lee, L.J. In *Life Cycle Energy Analysis and Environmental Life Cycle Assessment of Carbon Nanofibers Production*, Proceedings of the 2007 IEEE International Symposium on Electronics and the Environment, 2007; pp 128-133.

Khanna, V., Bakshi, B.R., Lee, L.J., Carbon nanofiber production: Life cycle energy consumption and environmental impact. *Journal of Industrial Ecology* **2008,** *12*, (3), 394-410.

Kim, C. S., Bao, L., Okuyama, K., Shimada, M., Niinuma, H., Filtration efficiency of a fibrous filter for nanoparticles. *Journal of Nanoparticle Research* **2006**[a], *8*, (2), 215-221.

Kim, J. H., Gibb, H.J., Howe, P.D. *Cobalt and inorganic cobalt compounds*; WHO: 2006[b].

Kim, S. C., Harrington, M.S., Pui, D.Y.H., Experimental study of nanoparticles penetration through commercial filter media. *Journal of Nanoparticle Research* **2007,** *9*, (1), 117-125.

Kissock, K., Hallinan, K., Bader, W., Energy and waste reduction opportunities in industrial processes. *Strategic Planning for Energy and the Environment* **2001,** *21*, (1), 40-53.

Kohler, A. R., Som, C., Helland, A., Gottschalk, F., Studying the potential release of carbon nanotubes throughout the application life cycle. *Journal of Cleaner Production* **2008,** *16*, (8-9), 927-937.

Kumari, L., Zhang, T., Du, G.H., Li, W.Z., Wang, Q.W., Datye, A., Wu, K.H., Thermal properties of CNT-Alumina nanocomposites. *Composites Science and Technology* **2008,** *68*, (9), 2178-2183.

Kushnir, D., Sanden, B.A., Energy requirements of carbon nanoparticle production. *Journal of Industrial Ecology* **2008,** *12*, (3), 360-375.

Lain, M. J., Recycling of lithium ion cells and batteries. *Journal of Power Sources* **2001,** *97-98*, 736-738.

Lam, C. W., James, J.T., McCluskey, R., Arepalli, S., Hunter, R.L., A review of carbon nanotube toxicity and assessment of potential occupational and environmental health risks. *Critical Reviews in Toxicology* **2006,** *36*, (3), 189-217.

Lapple, C., *Fluid and Particle Mechanics*. 1st ed.; Read Books: 1951.

Lee C.K., R. K. I., Preparation of $LiCoO_2$ from spent lithium-ion batteries. *Journal of Power Sources* **2002,** *109*, 17–21.

Li, N., Martin, C.R., Scrosati, B., High-rate, high-capacity, nanostructured tin oxide electrode. *Electrochemical and Solid-State Letters* **2000,** *3*, (7), 316-318.

Li, X. Y., Brown, D., Smith, S., MacNee, W., Donaldson, K., Short-term inflammatory responses following intratracheal instillation of fine and ultrafine carbon black in rats. *Inhalation Toxicology* **1999,** *11*, (8), 709-731.

Li, X. Y., Gilmour, P.S., Donaldson, K., MacNee, W., Free radical activity and pro-inflammatory effect of particulate air pollution (PM10) in vivo and in vitro. *Thorax* **1996,** *51*, (12), 1216-1222.

Lifton, V. A., Simon, S. In *A novel battery architecture based on superhydrophobic nanostructured materials*, 2005 NSTI Nanotechnology Conference and Trade Show - NSTI Nanotech 2005 Technical Proceedings, 2005; pp 726-729.

Likhachev, V. N., Vinogradov, G.A., Alymov, M.I., Anomalous heat capacity of nanoparticles. *Physics Letters, Section A: General, Atomic and Solid State Physics* **2006,** *357*, (3), 236-239.

Lin, C.-Y., Lee, K.-C., Yao, Y.D., The magnetic property and the structure change of iron nanocrystalline materials. *Solid State Communications* **1992,** *83*, (5), 371-374.

Liu, J., Rinzler, A.G., Dai, H., Hafner, J.H., Kelley Bradley, R., Boul, P.J., Lu, A., Iverson, T., Shelimov, K., Huffman, C.B., Rodriguez-Macias, F., Shon, Y.S., Lee, T.R., Colbert, D.T., Smalley, R.E., Fullerene pipes. *Science* **1998,** *280*, (5367), 1253-1256.

Liu, Z., Hong, L., Guo, B., Physicochemical and electrochemical characterization of anatase titanium dioxide nanoparticles. *Journal of Power Sources* **2005,** *143*, 231-235.

Lloyd, R. A. Hydrometallurgical Zinc Recovery Process and Apparatus. WO/1998/004752, 1998.

Lloyd, S. M., Lave, L.B., Life cycle economic and environmental implications of using nanocomposites in automobiles. *Environmental Science and Technology* **2003,** *37*, (15), 3458-3466.

Lloyd, S. M., Lave, L.B., Matthews, H.S., Life cycle benefits of using nanotechnology to stabilize platinum-group metal particles in automotive catalysts. *Environmental Science and Technology* **2005,** *39*, (5), 1384-1392.

Lu, K., Jin, Z.H., Melting and superheating of low-dimensional materials. *Current Opinion in Solid State and Materials Science* **2001,** *5*, (1), 39-44.

Lu, K., Wang, J.T., Wei, W.D., Comparison of properties of nanocrystalline and amorphous Ni-P alloys. *Journal of Physics D: Applied Physics* **1992,** *25*, (5), 808-812.

Magrez, A., Kasas, S., Salicio, V., Pasquier, N., Seo, J.W., Celio, M., Catsicas, S., Schwaller, B. , Forro, L., Cellular toxicity of carbon-based nanomaterials. *Nano Letters* **2006,** *6*, (6), 1121-1125.

Matos, G. R. *Use of Minerals and Materials in the United States From 1900 Through 2006*; USGS: 2009.

McLaughlin, W. J. Method for the neutralization of hazardous materials. US Patent 5345033, 1994.

McLaughlin, W., Adams, T.S. Li reclamation process. US Patent 5888463, 1999.

Mei, Q. S., Wang, S.C., Cong, H.T., Jin, Z.H., Lu, K., Determination of pressure effect on the melting point elevation of Al nanoparticles encapsulated in Al_2O_3 without epitaxial interface. *Physical Review B - Condensed Matter and Materials Physics* **2004,** *70*, (12), 125421-1-125421-5.

Muller, J., Huaux, F., Moreau, N., Misson, P., Heilier, J.-F., Delos, M., Arras, M., Fonseca, A., Nagy, J.B., Lison, D., Respiratory toxicity of multi-wall carbon nanotubes. *Toxicology and Applied Pharmacology* **2005,** *207*, (3), 221-231.

Nanosprint, Anatomy of a patenting area: Nanotube cutting. 2006.

Nanotech News, Modifications Render Carbon Nanotubes Nontoxic. 2005.

Nel, A., Xia, T., Madler, L., Li, N., Toxic potential of materials at the nanolevel. *Science* **2006,** *311*, (5761), 622-627.

Ngo, Q., Cruden, B.A., Cassell, A.M., Walker, M.D., Ye, Q., Koehne, J.E., Meyyappan, M., Li, J., Yang, C.Y. In *Thermal conductivity of carbon nanotube composite films*, Materials Research Society Symposium Proceedings, 2004; pp 179-184.

Nikkiso *Carbon Nanotube (CNT)*; Nikkiso.

Nikolaev, P., Bronikowski, M.J., Bradley, R.K., Rohmund, F., Colbert, D.T., Smith, K.A., Smalley, R.E., Gas-phase catalytic growth of single-walled carbon nanotubes from carbon monoxide. *Chemical Physics Letters* **1999,** *313*, (1-2), 91-97.

NIST Chemistry Webbook. http://webbook.nist.gov/chemistry (date accessed 12/18/2008).

NNCO *Nanotechnology and the environment*; 2003.

Oberdorster, G., Ferin, J., Lehnert, B.E., Correlation between particle size, in vivo particle persistence, and lung injury. *Environmental Health Perspectives* **1994,** *102*, 173-179.

Oberdorster, G., Maynard, A., Donaldson, K., Castranova, V., Fitzpatrick, J., Ausman, K., Carter, J., Karn, B., Kreyling, W., Lai, D., Olin, S., Monteiro-Riviere, N., Warheit, D., Yang, H., Principles for characterizing the potential human health effects from exposure to nanomaterials: Elements of a screening strategy. *Particle and Fibre Toxicology* **2005**[a], *2*, (8).

Oberdorster, G., Oberdorster, E., Oberdorster, J., Nanotoxicology: An emerging discipline evolving from studies of ultrafine particles. *Environmental Health Perspectives* **2005**[b], *113*, (7), 823-839.

Olapiriyakul, S., Caudill R.J., Thermodynamic Analysis to Assess the Environmental Impact of End-of-life Recovery Processing for Nanotechnology Products. *Environmental Science and Technology* **2009,** *43*, (21), 8140-8146.

Olapiriyakul, S., Caudill, R.J. In *A Framework for Risk Management and End-Of-Life (EOL) Analysis for Nanotechnology Products: A Case Study in Lithium-Ion Batteries*, Proceedings of the 2008 IEEE International Symposium on Electronics & the Environment, 2008.

Olapiriyakul, S., Elele, E., Caudill, R.J., End-Of-Life Analysis of Nanotechnology Products: A Case Study Focusing on the High Temperature Battery Recycling Process. In *13th Battery Materials Recycling Seminar and Exibit*, Florida, 2009.

Osaka, T., Asahi, T., Kawaji, J., Yokoshima, T., Development of high-performance magnetic thin film for high-density magnetic recording. *Electrochimica Acta* **2005,** *50*, (23), 4576-4585.

OSHA, Asbestos. In *Safety and health topics.*

Palit, S., Sharma, A., Talukder, G., The effects of cobalt on plants. *BOT.REV.* **1994,** *60*, (2), 149-181.

Panero, S., Scrosati, B., Wachtler, M., Croce, F., Nanotechnology for the progress of lithium batteries R&D. *Journal of Power Sources* **2004,** *129*, 90-95.

Parsons, D., The environmental impact of disposable versus re-chargeable batteries for consumer use. *International Journal of Life Cycle Assessment* **2007,** *12*, (3), 197-203.

Pechenik, A. Method for making a nano-stamp and for forming, with the stamp, nano-size elements on a substrate. US Patent 6365059, 2002.

Peter, J., Recharging EVs. *Automotive Industries AI* **2005,** *185*, (2).

Pisanic II, T. R., Blackwell, J.D., Shubayev, V.I., Finones, R.R., Jin, S., Nanotoxicity of iron oxide nanoparticle internalization in growing neurons. *Biomaterials* **2007,** *28*, (16), 2572-2581.

Portet, C., Yushin, G., Gogotsi, Y., Electrochemical performance of carbon onions, nanodiamonds, carbon black and multiwalled nanotubes in electrical double layer capacitors. *Carbon* **2007,** *45*, (13), 2511-2518.

Qi, W. H., Size effect on melting temperature of nanosolids. *Physica B: Condensed Matter* **2005,** *368*, (1-4), 46-50.

Qi, W. H., Wang, M.P., Liu, Q.H., Shape factor of nonspherical nanoparticles. *Journal of Materials Science* **2005,** *40*, (9-10), 2737-2739.

Qi, W. H., Wang, M.P., Size and shape dependent melting temperature of metallic nanoparticles. *Materials Chemistry and Physics* **2004,** *88*, (2-3), 280-284.

Qi, W. H., Wang, M.P., Size- and shape-dependent superheating of nanoparticles embedded in a matrix. *Materials Letters* **2005,** *59*, (18), 2262-2266.

Recupyl Lithium-ion battery recycling. http://www.recupyl.com/105-lithium-ion-battery-recycling.html (date accessed 5/5/2008).

Reddy, C. S. *Installtion of VFD for Reverse Air Fan and Operating at Optimum Bag House Pressure*; 2007.

Reistad, G. M., Available energy conversion and utilization in the United States. *Journal of Engineering for Power ASME* **1975,** *97 Ser A*, (3), 429-434.

Revesz, A., Lendvai, J., , Thermal properties of ball-milled nanocrystalline Fe, Co and Cr powders. *Nanostructured Materials* **1998,** *10*, (1), 13-24.

Roes, A. L., Marsili, E., Nieuwlaar, E., Patel, M.K., Environmental and cost assessment of a polypropylene nanocomposite. *Journal of Polymers and the Environment* **2007,** *15*, (3), 212-226.

Rosen, M. A., Evaluation of energy utilization efficiency in Canada using energy and exergy analyses. *Energy* **1992,** *17*, (4), 339-350.

Rosner, H., Wilde, G., The impact of altered interface structures on the melting behaviour of embedded nanoparticles. *Scripta Materialia* **2006,** *55*, (2), 119-122.

Rupp, J., Birringer, R., Enhanced specific-heat-capacity (C_p) measurements (150-300 K) of nanometer-sized crystalline materials. *Physical Review B (Condensed Matter)* **1987,** *27*, (1), 7888-7890.

Saidi, M., Yazid, Huang, H. Synthesis of metal phosphates. US Patent 7060238, 2006.

Schaeffer, R., Wirtshafter, R.M., An exergy analysis of the Brazilian economy: From energy production to final energy use. *Energy* **1992,** *17*, (9), 841-855.

SETAC http://www.setac.org (date accessed 12/18/2008).

Shin, W. G., Mulholland, G.W., Kim, S.C., Pui, D.Y.H., Experimental study of filtration efficiency of nanoparticles below 20 nm at elevated temperatures. *Journal of Aerosol Science* **2008,** *39*, (6), 488-499.

Silva, G. G., Musumeci, A.W., Gomes, A.P., Liu, J.-W., Waclawik, E.R., George, G.A., Frost, R.L., Pimenta, M.A., Characterization of commercial double-walled carbon nanotube material: Composition, structure, and heat capacity. *Journal of Materials Science* **2009,** *44*, (13), 3498-3503.

SNAM http://www.snam.com (date accessed 5/5/2008).

Sony, Sony's new nexelion hybrid lithium ion batteries to have thirty-percent more capacity than conventional offering.

Steeluniversity http://www.steeluniversity.org (date accessed 12/18/2008).

Steffens, J., Coury, J.R., Collection efficiency of fiber filters operating on the removal of nano-sized aerosol particles: I-Homogeneous fibers. *Separation and Purification Technology* **2007[a],** *58*, (1), 99-105.

Steffens, J., Coury, J.R., Collection efficiency of fiber filters operating on the removal of nano-sized aerosol particles. II. Heterogeneous fibers. *Separation and Purification Technology* **2007[b],** *58*, (1), 106-112.

Sun, N. X., Lu, K., Heat-capacity comparison among the nanocrystalline, amorphous, and coarse-grained polycrystalline states in element selenium. *Physical Review B - Condensed Matter and Materials Physics* **1996,** *54*, (9), 6058-6061.

Szargut, J., Morris, D.R., Steward, F.R., *Exergy analysis of thermal, chemical, and metallurgical processes*. Hemisphere Publishing Corporation: New York, 1988.

Tang, Z. A., Ding, H.T., Huang, Z.X., Xu, Z.Q., Li, X., Molecular dynamics simulation of specific heat capacities of SiO_2 thin films. *Dalian Ligong Daxue Xuebao/Journal of Dalian University of Technology* **2005,** *45*, (3), 313-315.

Templeton, R. C., Ferguson, P.L., Washburn, K.M., Scrivens, W.A., Chandler, G.T., Life-cycle effects of single-walled carbon nanotubes (SWNTs) on an estuarine meiobenthic copepod. *Environmental Science and Technology* **2006,** *40*, (23), 7387-7393.

Tian, F., Cui, D., Schwarz, H., Estrada, G.G., Kobayashi, H., Cytotoxicity of single-wall carbon nanotubes on human fibroblasts. *Toxicology in Vitro* **2006,** *20*, (7), 1202-1212.

Toxco http://www.toxco.com (date accessed 5/5/2008).

Tremaine, P. R., Xiao, C., Enthalpies of formation and heat capacity functions for maricite, $NaFePO_4$(cr), and sodium iron(III) hydroxy phosphate, $Na_3Fe(PO_4)_2$-($Na_{4/3}$ $H_{2/3}O$)(cr). *Journal of Chemical Thermodynamics* **1999,** *31*, 1307-1320.

U.S.DepartmentofEnergy *Install Waste Heat Recovery Systems for Fuel-Fired Furnaces*; 2005.

Ukidwe, N. U., Bakshi, B.R., Industrial and ecological cumulative exergy consumption of the United States via the 1997 input-output benchmark model. *Energy* **2007,** *32*, (9), 1560-1592.

USDA, USDA National Nutrient Database for Standard Reference, Release 22. Agricultural Research Service, Nutrient Data Laboratory: 2009.

USEPA http://epa.gov/ncer/rfa/2009/2009_uk_nano.html

Uskokovic, V., Nanotechnologies: What we do not know. *Technology in Society* **2007,** *29*, 43-61.

Wall, G. *Exergy Conversion in the Finnish, Japanese and Swedish Societies*; Turku School of Economics: 1991.

Wall, G. In *Exergy use in the Swedish society 1994*, Proceedings of the International Conference on Thermodynamic Analysis and Improvement of Energy Systems, 1997; pp 403-413.

Wall, G., Exergy conversion in the Japanese society. *Energy* **1990,** *15*, (5), 435-444.

Wall, G., Sciubba, E., Naso, V., Exergy use in the Italian society. *Energy* **1994,** *19*, (12), 1267-1274.

Wang, J., Wang, G., Yang, L., Ng, S.H., Liu, H., An investigation on electrochemical behavior of nanosize zinc sulfide electrode in lithium-ion cells. *Journal of Solid State Electrochemistry* **2006,** *10*, (4), 250-254.

Wang, L., Tan, Z., Meng, S., Druzhinina, A., Varushchenko, R.A., Li, G., Heat capacity enhancement and thermodynamic properties of nanostructured amorphous SiO_2. *Journal of Non-Crystalline Solids* **2001**[a], *296*, (1-2), 139-142.

Wang, L., Tan, Z., Meng, S., Liang, D., Gao, D., Sun, Z., Liu, Z., Low temperature heat capacity and thermal stability of nanocrystalline iron. *Cailiao Yanjiu Xuebao/Chinese Journal of Materials Research* **2002,** *16*, (1), 13-16.

Wang, L., Tan, Z., Meng, S., Liang, D., Li, G., Enhancement of molar heat capacity of nanostructured Al2O3. *Journal of Nanoparticle Research* **2001**[b], *3*, (5-6), 483-487.

Wang, L., Tan, Z., Meng, S., Liang, D., Liu, B., Low temperature heat capacity and thermal stability of nanocrystalline nickel. *Thermochimica Acta* **2001**[c], *386*, (1), 23-26.

Wang, M. T. Nano photocatalyst coating procedure. US Patent 0129853, 2005.

Wang, S., Lu, W., Tovmachenko, O., Rai, U.S., Yu, H., Ray, P.C., Challenge in understanding size and shape dependent toxicity of gold nanomaterials in human skin keratinocytes. *Chemical Physics Letters* **2008,** *463*, (1-3), 145-149.

Wang, W., Kumta, P.N., Reversible high capacity nanocomposite anodes of Si/C/SWNTs for rechargeable Li-ion batteries. *Journal of Power Sources* **2007,** *172*, (2), 650-658.

Waseda, Y., Isshiki, M., *Purification Process and Characterization of Ultra High Purity Metals Application of Basic Science to Metallurgical Processing*. Springer: 2001.

Wilson, B., Nanotechnology and the future of displays. *Nanotechnology Law and Business* **2006,** *3*, (2), 127-133.

Wolfenstine, J., Allen, J.L., Read, J., Foster, D. *Chemistry and structure of Sony's Nexelion Li-ion electrode materials*; Army Research Laboratory: 2006.

Worle-Knirsch, J. M., Kern, K., Schleh, C., Adelhelm, C., Feldmann, C., Krug, H.F., Nanoparticulate vanadium oxide potentiated vanadium toxicity in human lung cells. *Environmental Science and Technology* **2007,** *41*, (1), 331-336.

Wu, G. T., Wang, C.S., Zhang, X.B., Yang, H.S., Qi, Z.F., He, P.M., Li, W.Z., Structure and lithium insertion properties of carbon nanotubes. *Journal of the Electrochemical Society* **1999,** *146*, (5), 1696-1701.

Wu, X. M. W., L.; Tan, Z.C.; Li, G.H.; Qu, S.S., Preparation, Characterization, and Low-Temperature Heat Capacities of Nanocrystalline TiO_2 Ultrafine Powder. *Journal of Solid State Chemistry* **2001,** *156*, 220-224.

Wu, Y. P., Rahm, E., Holze, R., Carbon anode materials for lithium ion batteries. *Journal of Power Sources* **2003,** *114*, 228-236.

Yamada, A., Hosoya, M., Chung, S.C., Kudo, Y., Hinokuma, K., Liu, K.Y., Nishi, Y., Olivine-type cathodes Achievements and problems. *Journal of Power Sources* **2003,** *119-121*, 232-238.

Zhang, L., Jin, Z.H., Zhang, L.H., Sui, M.L., Lu, K., Superheating of confined Pb thin films. *Physical Review Letters* **2000[a]**, *85*, (7), 1484-1487.

Zhang, L., Zhang, L.H., Sui, M.L., Tan, J., Lu, K., Superheating and melting kinetics of confined thin films. *Acta Materialia* **2006,** *54*, (13), 3553-3560.

Zhang, Q., Kusaka, Y., Donaldson, K., Comparative pulmonary responses caused by exposure to standard cobalt and ultrafine cobalt. *Journal of Occupational Health* **2000[b]**, *42*, (4), 179-184.

Zhang, Q., Kusaka, Y., Sato, K., Nakakuki, K., Kohyama, N., Donaldson, K., Differences in the extent of inflammation caused by intratracheal exposure to three ultrafine metals: Role of free radicals. *Journal of Toxicology and Environmental Health - Part A* **1998,** *53*, (6), 423-438.

Zhang, Q., Kusaka, Y., Zhu, X., Sato, K., Mo, Y., Kluz, T., Donaldson, K., Comparative toxicity of standard nickel and ultrafine nickel in lung after intratracheal instillation. *Journal of Occupational Health* **2003,** *45*, (1), 23-30.

Zhong, J., Zhang, L.H., Jin, Z.H., Sui, M.L., Lu, K., Superheating of Ag nanoparticles embedded in Ni matrix. *Acta Materialia* **2001,** *49*, (15), 2897-2904.

Ziegler, K. J., Gu, Z., Peng, H., Flor, E.L., Hauge, R.H., Smalley, R.E., Controlled oxidative cutting of single-walled carbon nanotubes. *Journal of the American Chemical Society* **2005,** *127*, (5), 1541-1547.